The Development of an On-line Fan Blade Damage Detection Methodology

by

Abraham Johannes Oberholster

Submitted in fulfilment of part of the requirements for the degree of Master of
Engineering in the Faculty of Engineering, the Built Environment and Information
Technology
University of Pretoria
Supervisor: Professor P. S. Heyns

2004

The Development of an On-line Fan Blade Damage Detection Methodology

by

Abraham Johannes Oberholster
Supervisor: Professor P.S. Heyns

Department of Mechanical and Aeronautical Engineering
Degree: M Eng

Summary

This dissertation entails the development of an on-line fan blade damage detection methodology. The aim is to use a minimal number of sensors to measure in-operation blade vibrations in order to qualify and quantify fan blade damage in terms of blade root crack length for multiple blades. An experimental setup namely the Fan Blade Condition Monitoring Test Structure (FaBCoM TeSt) was used to develop such a methodology.

A Finite Element Model (FEM) of the FaBCoM TeSt was developed to study the feasibility of using Global Mode Shape Frequency (GMSF) shifts for damage quantification and qualification, to identify GMSFs useful for damage detection in the FaBCoM TeSt and to select features from Frequency Response Functions (FRFs) of the FEM for training neural networks to be used on the FaBCoM TeSt.

The feasibility study was done by performing modal analyses on the FEM for different levels of damage for two blade damage scenarios. Also, the influences of typical fan operating condition variables such as temperature and rotational velocity were investigated. The results of these modal analyses were used to identify GMSFs that are sensitive damage indicators in terms of frequency shifts.

In order to verify the validity of the FEM, an Experimental Modal Analysis (EMA) was performed on the FaBCoM TeSt. A Modal Assurance Criterion (MAC) matrix of the FEM was calculated, the results of which led to a decision to update the model by means of frequency tuning and adjusting material properties.

Piezoelectric accelerometers and strain sensors were used as transducers during experimental testing due to their compactness and low masses. As no suitable wireless vibration data transmission system for testing could be found, it was decided to make use of a slip ring assembly for signal transmission. Operational vibration measurements were taken on the FaBCoM TeSt by means of strain sensors on three of

the four blades as well as a radially orientated piezoelectric accelerometer. Measurements were taken for different blade damage scenarios, levels of damage and sensor location scenarios.

The suitability of using neural networks for damage identification using less than one sensor per blade was studied for two different approaches. The first approach was to train neural networks with features obtained form the experimental measurements. Very satisfying results were obtained, proving the ability of neural networks to do damage detection on a fan for all the above-mentioned scenarios when experimental supervision is employed.

For expensive and critical industrial equipment however, neural networks cannot necessarily be trained using this type of supervision due to cost implications. Therefore, the second approach was to train neural networks with features obtained from FRFs calculated using the FEM. Normalization of the FEM features was needed and for this, a single set of feature normalizing constants were calculated from a single set of experimental measurements obtained from an undamaged structure. Very good results were obtained proving the feasibility of using this approach on an operating structure.

Keywords: *On-line blade vibration; damage detection; experimental modal analysis; frequency sensitivity analysis; neural networks; finite element modelling; model updating; feature normalization; numerical testing; experimental testing*

Die Ontwikkeling van 'n Operasionele Waaierlemskade Opsporingsmetodologie

deur

Abraham Johannes Oberholster
Studieleier: Professor P.S. Heyns

Departement Meganiese en Lugvaartkundige Ingenieurswese
Graad: M Ing

Opsomming

Hierdie verhandeling handel oor die ontwikkeling van 'n operasionele waaierlemskade opsporingsmetodologie. Die doel was om gebruik te maak van 'n minimum aantal sensors om die operasionele vibrasies van lemme te meet om sodoende skade kwalifisering en kwantifisering te kan doen in terme van lemwortel kraaklengte vir 'n meervoudige aantal lemme. Ten einde so 'n metodologie te ontwikkel is gebruik is gemaak van 'n eksperimentele opstelling genaamd die Waaierlem Toestandsmonitering Toets Struktuur (WTTS).

'n Eindige Element Model (EEM) van die WTTS is ontwikkel om die moontlikheid van die gebruik van Globale Modusvorm Frekwensie (GMF) skuiwe vir skade kwanitifisering en kwalifisering te bepaal, om GMFs te identifiseer vir gebruik van skade opsporing in die WTTS en om kenmerke te selekteer vanaf Frekwensie Responsie Funksies (FRFs) verkry van die EEM om neurale netwerke op te lei vir gebruik op die WTTS.

Die moontlikheid om gebruik te maak van GMF skuiwe vir skade opsporing, is ondersoek deur modale analises te doen op die EEM vir verskeie skadevlakke vir twee lemskade gevalle. Die invloed van tipiese waaier werkstoestandveranderlikes, naamlik temperatuur en rotasiesnelheid is ook ondersoek. Die resultate van hierdie modale analises is ook dan gebruik vir 'n GMF sensitiwiteitsanalise om sodoende GMFs te identifiseer wat sensitiewe skade-aanduiders is.

Die geldigheid van die EEM is geverifiëer deur 'n eksperimentele modale analise op die WTTS gedoen. 'n Modale versekeringskriterium matriks van die EEM is bereken en die resultate hiervan het gelei tot die besluit om die EEM op te dateer deur middel van frekwensie instemming en materiaaleienskap verfyning.

Daar is besluit om gebruik te maak van piezo-elektriese versnellingsmeters en vervormingsmeters as sensors na aanleiding van hulle kompaktheid en lae massas.

iii

Aangesien geen geskikte draadlose vibrasie data sender stelsel geïdentifiseer kon word vir toets doeleindes nie, is die besluit geneem om van sleepringe gebruik te maak vir seingeleiding. Vibrasiemetings is geneem op die WTTS deur middel van vervormingsmeters wat op drie van die vier lemme geïnstalleer is asook `n piezo-elektriese versnellingsmeter wat radiaal georiënteer is. Metings is geneem vir verskeie lemskade gevalle, skadevlakke en meetposisie gevalle.

Die geskiktheid daarvan om neurale netwerke te gebruik vir skade opsporing deur gebruik te maak van minder as een sensor per lem is bestudeer deur middel van twee verskillende benaderings. Die eerste hiervan was om neurale netwerke op te lei met eienskappe wat verkry is vanaf die eksperimentele metings. Baie goeie resultate is verkry wat bewys dat neurale netwerke die vermoë het om skade opsporing uit te voer op `n waaier vir al die genoemde gevalle wanneer eksperimentele opleiding gebruik word.

Vir duur en kritieke industriële masjinerie, kan neurale netwerke nie noodwendig opgelei word deur gebruik te maak van hierdie tipe opleiding nie as gevolg van koste implikasies. Die tweede benadering was dus om neurale netwerke op te lei met eienskappe wat verkry is vanaf FRFs wat bereken is met die EEM. Normalisering van die EEM eienskappe was nodig en daarvoor is normaliseringskonstantes bereken vanaf `n enkele stel eksperimentele metings wat verkry is vanaf `n onbeskadigde struktuur. Baie goeie resultate is verkry wat bewys dat hierdie benadering wel gebruik kan word op 'n operasionele struktuur.

Sleutelterme: _Operasionele lemvibrasie; skade opsporing; eksperimentele modale analise; frekwensie sensitiwiteitsanalsise; neurale netwerke; eindige element modellering; model opdatering; eienskap normalisering; numeriese toets; eksperimentele toets_

Acknowledgements

I would like to thank the following people for their support and contribution:

- Professor P.S. Heyns
- Cornie Scheffer
- Leon Staphorst
- Frans Windell
- Willy Garnett-Bennett
- Mark Newby
- Francois du Plooy
- De Wet Strydom

I would also like to thank the following people for their personal support:

- Jesus Christ
- Jan and Magdaleen Oberholster
- Joekie de Kock
- Anne-Marie van Heerden

and all my friends.

Table of Contents

Nomenclature

Symbols

A	Area [m^2]
c	Constant
$CW(f)$	Coherence-window function
$C_{pxx}(\tau)$	Power cepstrum
df	Frequency derivative
dt	Time derivative
E$_y$	Young's modulus [GPa]
$E[x^2]$	Mean-Square value
f	Frequency [Hz]
H	Transfer function
I	Second moment of inertia [m^4]
i	Integer [#]
j	Integer [#]
$[K]$	Stiffness matrix
$[K_g]$	Geometric stiffness matrix
k	Discrete frequency number [#]
l	Length [m]
$[M]$	Mass matrix
$M_{a,b}(f)$	Modal Ratio Function
N	Number of data points
n	Number of discrete frequencies [#]
$PW(f)$	Phase-window function
p	Number of group elements [#]
R^2	Squared Pearson Product Moment Correlation Coefficient
T	Time period [s]
t	Time variable [s]
$TF_{a,b}(f)$	Transmissibility function
$\overline{U}$	Random variable vector
$[V]$	Linear combination matrix
$[W]$	Covariance matrix
$x(t)$	Time signal
$\ddot{x}(t)$	Second derivative of $x(t)$
$X(f)$	Fourier transform of the time signal $x(t)$
$X^*(f)$	Complex conjugate of $X(f)$

X_{max}	Peak value of the time signal $x(t)$
X_{RMS}	Root-Mean-Square value of the time signal $x(t)$
βl	Transverse beam vibration boundary condition value
Δt	Time sampling interval [s]
$\gamma^2(f)$	Coherence function
γ_c^2	Coherence cut-off
λ	Eigenvalue matrix
$\theta(f)$	Phase angle function
θ_c	Phase angle cut-off
ρ	Density [kg.m^{-3}]
σ^2	Variance
ω	Frequency [rad.s^{-1}]
$\{\psi\}$	Eigenvector matrix

Abbreviations

AD	Analogue to Digital
ANPSD	Averaged Normalized Power Spectral Density
ARMAX	Autoregressive Moving Average with Exogenous input
Cov	Covariance
DOF	Degree of Freedom
EFBDS	Experimental Fan Blade Damage Simulator
EMA	Experimental Modal Analysis
EMS	Experimental Mode Shape
FaBCoM TeSt	Fan Blade Condition Monitoring Test Structure
FD	Forced Draught
FEM	Finite Element Model
FRF	Frequency Response Function
GMSF	Global Mode Shape Frequency
ID	Induced Draught
LDV	Laser Doppler Vibrometer
LTF	Linear Transfer Function
LWIM	Low Power Wireless Integrated Microsensors
MAC	Modal Assurance Criterion
MEMS	Micro-electromechanical Systems
MPC	Multi-Point Constraint
MRF	Modal Ratio Function
NExT	Natural Excitation Technique
NMS	Numerical Mode Shape

NPSD	Normalized Power Spectral Density
PCA	Principal Component Analysis
PSD	Power Spectral Density
PSDRMS	Power Spectral Density Root-Mean-Square
RMS	Root-Mean-Square
SDT	Structural Dynamics Toolbox
SL	Sensor Location
TSTF	Tan-Sigmoid Transfer Function
Var	Variance
WLAN	Wireless Local Area Network

Chapter 1   Introduction and Literature Study

1.1. Introduction

The on-line condition monitoring of industrial equipment is of great importance. As industry focuses more and more on productivity, conventional condition monitoring methods are not always viable options when the shutdown of equipment and possibly the subsequent shutdown of the whole production cycle is required. A practical example is the Forced Draught (FD) and Induced Draught (ID) fans found at coal powered power station boilers such as Majuba Power Station in South Africa. These fans facilitate airflow through the boilers in order to sustain combustion. This means that a whole power production unit needs to be shut down when stationary condition monitoring of these fans is required.

A big problem currently experienced with the fans is the failing of blade attachment shafts resulting in the separation of the involved blades which in turn cause secondary damage as well as production loss, both of which involve large financial implications. The blade attachment shafts experience a lot of fatigue loading during start-up and shutdown and as a result, fatigue cracks initiate and grow. For an application such as this, the need arises for blade damage qualification and quantification. This basically means that a system or methodology is needed to determine which blade shaft attachments are damaged and to which extent they are damaged.

For this type of application, a number of issues need to be addressed. In the first place, rotating equipment present a unique problem namely that of transducer signal or data transmission from the rotating parts. Also, the number of transducers used needs to be addressed. For example, if only one transducer is to be installed on each blade of a FD or ID fan, this will result in a huge amount of data to be processed as these fans typically have twenty blades each. Another issue is that of the effect of electrical noise on measurements.

For this dissertation, use is made of a test structure to develop such a methodology.

1.2. Majuba Fan Operating Conditions

To obtain better understanding and insight into the operational conditions of the FD and ID fans at Majuba Power Station, the station's Draught Plant Systems Engineer was consulted [19].

The fans at Majuba Power Station have been in operation for 12000 hours, which very roughly translates to 1.5 years of operation for 18.5 hours of operation per day. The problems experienced are not with the blades themselves, but the cracking of the blade attachment shafts. These shafts crack and these cracks then propagate until

catastrophic failures occur. A typical blade attachment shaft failure is shown in Figure 1-1.
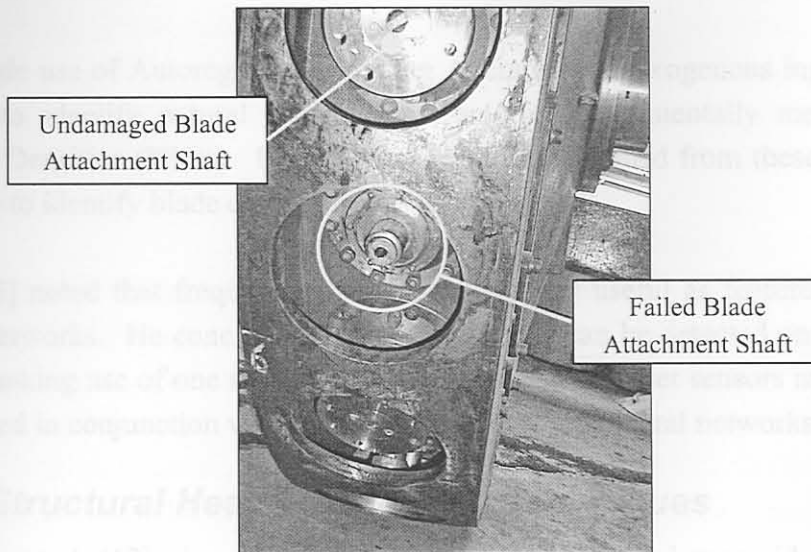
Figure 1-1: Blade Attachment Shaft Failure

The ID fans operate in the gas outlet environment. No debris deposit onto the blades is evident except for ash clinging to the oily surface caused by mild oil or grease leakage or "sweat". The maximum debris mass is estimated to be about 20 g, covering the lower third blade surface area. The fans rotate at a constant speed of 740 rpm and operate at a temperature of about 110 °C. Change in the blade characteristics is more wear-related specifically around the blade tip leading edges.

The FD fans operate in the clean air intake environment. Again, no debris deposit is evident on the blades except for dust clinging to the oily surface caused by "more than mild" oil or grease leakage. The maximum debris mass is approximated to be about 40 g, distributed over the lower third surface area of the blade. Rotational velocity is fixed at 930 rpm and operating temperatures vary from 20 °C to 60 °C.

1.3. Previous Work

This dissertation is a continuation of the work done by Smit [45]. Smit developed a methodology for detecting damage on a single blade of a fan assembly with sensors installed on the damaged blade. Smit made use of a simple finite element model to determine the sensitivity of blade natural frequencies to damage as well as to determine optimal sensor placement. He concluded that blade fatigue damage will nearly always be situated in the blade root region due to the blade loading stress distribution during operation.

Smit [45] designed the Experimental Fan Blade Damage Simulator (EFBDS) to conduct tests using piezoelectric accelerometers and piezoelectric strain sensors as

transducers and a slip ring assembly for signal transmission. The EFBDS was renamed to the FaBCoM TeSt for this dissertation.

Smit made use of Autoregressive Moving Average with Exogenous input (ARMAX) models to identify natural frequencies from the experimentally measured Power Spectral Densities (PSDs). Using frequency shifts obtained from these models, Smit was able to identify blade damage levels as low as 10%.

Smit [45] noted that frequency shifts could be very useful as features for use with neural networks. He concluded that damage levels can be detected on individual fan blades making use of one sensor per blade. The use of fewer sensors may be possible when used in conjunction with global mode shapes and neural networks.

1.4. Structural Health Monitoring Techniques

Doebling et al. [12] give a literature review on structural damage identification and health monitoring using vibration characteristics changes. They note that lower modal frequencies generally cannot provide spatial information with regards to structural changes.

Higher modal frequencies however overcome this limitation where the modes are associated with local responses. These modes can be difficult to identify due to high modal density. Multiple frequency shifts can provide structural damage spatial information. Of the papers reviewed in Doebling and his co-workers, several point out that there are often not a sufficient number of damage sensitive frequencies of a structure available for unique damage location.

Hu et al. [24] developed two identification algorithms for assessing structural damage using modal test data. Unlike most approaches, the developed algorithms are not strongly dependant on analytical models. For the identification of damage location, the researchers define a normalized damage index to judge the existence of damage in a set of members in a structure. The damaged index is a function of the modal parameters of the undamaged structure as well as of the damaged structure. The damaged index is calculated for each specified structural member, where when the index is large for a specific member, it can be thought that the possibility of damage in that specific member is very high.

For practical implementation, Hu and his co-workers [24] note that the problem of not being able to measure all of the structural Degrees Of Freedom (DOFs) in the vibration modes can be overcome by employing condensation techniques or modal expansion techniques. They also developed an algorithm to estimate the extent of

damage in the possible damaged members, obtained from the damage location identification algorithm.

Hu et al. [24] validated their algorithms experimentally and numerically on a fixed-fixed aluminium beam, damaged by means of a saw-cut approximating a crack. For the detection of damage location, good results were obtained. However, accurate estimation of the damage extent was not possible.

Quek et al. [40] performed a sensitivity analysis of crack detection in beams making use of the wavelet technique. They found the method to yield very good results for simple-supported and fixed-end beams. Only numerical problems, where the static deflection profiles were obtained using FEM, were evaluated. The method is very good in locating beam cracks and perturbations. However, the deflection profile of the beam needs to be measured, which yields the technique unsuitable for this dissertation.

1.5.   Measurement   Techniques   for   Fans   and   Rotating Structures

Maynard and Trethewey [34] summarize field demonstrations of the feasibility of blade and shaft natural frequency changes associated with blade and shaft cracks using torsional vibration measurements. This is done using non-contact, non-intrusive measurements on operating machinery including a large wind tunnel fan, a jet engine high-pressure disk, a hydro station turbine and a large ID fan motor at a coal-fired power plant. The transducer consists of a tape shaft encoder, infrared fibre optic probe, an analogue incremental demodulator and an Analogue to Digital (AD) converter.

Williams et al. [54] describe a methodology for using rotational data acquisition techniques and rotational noise path analysis for rear wheel drive vehicle transmission and driveline development for noise vibration harshness performance. Three rotational vibration data acquisition methods are compared namely the use of a laser rotational vibrometer, paired tangential accelerometers and torsional strain gauges. For the laser rotational vibrometer, data is obtained from a reflective tape circumventing the propeller shaft. For the accelerometers and strain gauges, data transmission occurs by means of slip rings. These researchers found the accelerometer and strain gauge methods to obtain better measurements for low-level rotational vibrations levels than the laser method.

1.6.   Modal Analysis of Rotating Structures

A number of researchers ([26], [31], [51]) note that modal parameter changes, whether it is mode shape, modal frequency or mass, stiffness and damping matrices,

are sensitive indicators of structural damage. For this reason, it was decided to look into the modal analyses of operational structures. Authors such as Ewins [13] and Bucher [6] give in-depth theoretical discussions of in-operation modal analysis of rotating structures.

Carne and Nord [8] developed a technique to measure the vibration modes of a rotating vertical axis wind turbine. Use was made of a snap-release device installed on the rotating shaft of the turbine to excite one blade during rotation at a specific rotational speed. The device provides the ability to induce repeatable pulse inputs to a blade which allows the input force to be measured as needed for a modal analysis.

A detailed modal test of the parked turbine (or a normal static modal analysis) was performed prior to the rotating modal test in order to understand the modal characteristics well. These results were then used to update a FEM of the parked turbine. A rotating modal test was then performed and the results compared to the predictions of the FEM taking rotational effects into account. Excellent agreement was obtained.

Carne and Nord [8] also raise a very important point: As use is made of a rotating coordinate system, Coriolis effects influence the results obtained. Together with centrifugal effects, they cause the modes of the rotating system to be complex. These researchers did a thorough study on other methods of excitation during rotation such as piezoelectric crystals and gas jets. Evacuated chambers were used for testing, thus eliminating unwanted excitation forces by winds.

Wilkie et al. [53] experimentally determined rotating blade frequencies for a model generic helicopter blade for different rotational velocities. The blades were excited during rotation by means of rotor collective pitch oscillation, the frequency of which was varied over a maximum of 20 Hz frequency band in the vicinity of each modal frequency of interest. Strain gauges mounted onto the blades were used for output signals, while the strain gauge measurement of the pitch-link was used as input signal in order to generate FRFs.

No attempt was made to measure blade mode shapes during operation. The experimental results were compared to the results obtained from FEM modal analyses. Only centrifugal forces were considered during the numerical analyses that were performed in two steps namely static analysis with the centrifugal forces and a modified normal mode analysis performed as a "restart" analysis. The authors ignored the effect of damping and Coriolis terms. Good correlation between the FEM

results and experimental results were obtained although discrepancies were observed for blade torsional frequencies.

Marscher [32] presents a method involving cumulative time averaging of an exponentially windowed output prior to Fourier transformation in order to determine modal characteristics of industrial and aerospace rotating machinery. The structure is artificially excited at a stationary point during machine operation and vibration measurements are taken on the machine casing. Response due to artificial excitation is separate from response due to operational excitation by means of cumulative time averaging.

Shu and Cutts [44] present two analysis methods for modal parameter extraction from strain responses of rotating bladed assemblies. The two methods are frequency spectrum interpolation and time domain modal curve fitting. Shu and Cutts found both techniques to be very reliable, efficient and easy.

1.7.   *Fan Blade Condition Monitoring Techniques*

Ghoshal et al. [21] tested four different algorithms for damage detection in wind turbine blades namely transmissibility function, resonant comparison, operational deflection shape and wave propagation methods. The transmissibility functions were calculated as the ratios of the velocity responses at different points on the structure. Velocities were used, as this is the direct output of the scanning Laser Doppler Vibrometer (LDV) used.

These researchers identify certain advantages of using transmissibility functions:
- The excitation force is cancelled and therefore does not need to be measured if it is equal in amplitude at all points where applied.
- The ratio of responses partially cancels changes in the transmissibility functions due to environmental effects such as temperature changes.
- Transmissibility functions are ratios of two continuous functions with peaks and valleys and are therefore quite sensitive to shifts in frequencies or damping caused by damage.

It should be noted that Ghoshal et al. [21] conducted the tests for a stationary blade.

Ghosh and Rajamani [20] describe a transfer matrix approach for the vibration analysis of a rotating fan. They also developed an analytical procedure for computation of the free vibration behaviour of a rotating fan assembly. The number of blades is assumed to be large enough in order to consider the resultant blade loadings as continuously distributed.

Südmersen et al. [50] present global monitoring techniques for industrial fans and pumps including time domain analysis, spectrum analysis, correlation analysis and cepstrum analysis. The authors note that a common method to identify speed related information is time averaging of signals using external signal triggering. They also note that operating conditions with exceeded vibration levels such as during start up and shut down procedures, reduce total machine life time.

Corbelli et al. [10] investigate the applicability of damage detection using FRF data to rotating helicopter rotors. Modal parameters were extracted from FRF data obtained from a finite element model of helicopter rotor blades for the hovering condition. This was done for both an undamaged and damaged configuration. The FRF-based identification procedure was used to evaluate structural stiffness variation.

Corbelli and his co-workers found that damage detection presented in terms of stiffness variation show a good capability for damaged detection, location and quantification. As these results were obtained from numerical calculations, the authors note that future work must be done to study the influence of noise in measured FRF data on damage identification capability. They also suggest studies into the influence of torsional FRF measurements on damage identification.

1.8.   Telemetry Identification

1.8.1.   Data Transmission

A lot of effort was put into identifying a suitable telemetry system for data or signal transmission from a rotating machine. Two options presented themselves, namely slip ring assembly and wireless data transmission. Slip rings are most commonly used but have disadvantages such as limited operating life due to sliding contact wear, which in turn produces electrical noise ([42]). Also slip rings are usually practical only when the slip ring can be installed onto the shaft end. Due to these limitations, it was decided to look into the suitability of wireless telemetry.

The following considerations should be taken into account when selecting wireless telemetry for vibration analysis ([46]):
- Type of signal transmitted (analogue or digital)
- Digital resolution required when a digital signal is used
- Required transmission signal gain
- Signal domain type to be measured (e.g. time domain or frequency domain)
- Transducers used
- Number of channels required
- Size and weight of transmitter
- Power supply to transmitter

- Transmission range
- Type of signal transmission. Preference should be given to frequency modulated transmission of a digitised signal
- On-line transmitter configuration by base station
- Installation of the transmitter on the rotating component

The biggest limitations of currently available wireless telemetry was found to be
- Size
- Power supply to the transmitter side of the system
- Speed, as most telemetry systems are digital. Thus pre-processing is required.
- Cost

1.8.2. Advances in Wireless Telemetry

Bult et al. [7] present new methods providing diverse sensor capability with new low power solutions for wireless sensor networks. The technology reported in this paper differs from prior work in wireless sensor technology in that the sensor, control and communication system are integrated into a single unit.

The applications of Micro-electromechanical Systems (MEMS) are being expanded by a new technology called Low Power Wireless Integrated Microsensors (LWIM). Bult et al. [7] note that LWIM nodes may be in particular applied to rotating machinery without complex slip ring systems normally required for sensor electrical interface.

The requirements for individual low cost sensors nodes are that the nodes must be
- Reconfigurable by their base station
- Autonomous to permit local control of operation and power management
- Self-monitoring for reliability
- Power efficient for long term operation
- Able to incorporate diverse sensors capability with highly capable microelectronics

Bult et al. [7] note that for typical low duty cycle of a LWIM, a conventional lithium coin cell is able to provide more than three years of unattended operating life. Unfortunately, typical frequency ranges of LWIMs are not reported.

Miettinen et al. [36] developed a wireless data transfer system for measuring on-line acoustic emission, temperature distribution and angular position of polymer covered cylindrical rolls. The measured signal is transferred from the rotating rolls via Wireless Local Area Network (WLAN) to the measurement computer. An interesting

8

advantage of using on-line monitoring mentioned by the authors, is that it can be used to determine optimum operating conditions of machinery.

The measurement system consists of amplifiers for the different sensor types, anti-aliasing filters, AD-converters and a radio transmitter. The sampling rate used was 1 MHz. Miettinen et al. [36] also describe the principles of acoustic emission.

Li et al. [28] designed a polysilicon cantilever rotation sensor able to measure angular speeds from 100 rpm to 6000 rpm. The authors used a transmission scheme in which the voltage signal from the sensor is mapped into frequency prior to transmission resulting in a very compact package (smaller than 3 cm^3). Unfortunately, Li et al. [28] tested the frequency response range of the system from about 30 Hz to only about 110 Hz. Li and his co-workers found the sensor to be temperature dependent.

Olofsson and Östling [39] investigate the implementation of Bluetooth technology in accelerometer data transmission. The concept is proven in a point-to-point sensor demonstration. Bluetooth transceivers operate in the Industrial, Scientific and Medical band at 2.4 GHz. The transceivers make use of frequency hop and spread spectrum communication in order to combat signal interference. Data transmission of up to 720 kbps over a range of up to 100 m is possible with line of sight not necessary. Bluetooth technology is already implemented in equipment such as cellular phones and wireless modems. Although Bluetooth systems are very cheap to purchase, they are expensive to develop.

1.8.3. Transducers

Brooks [5] gives an overview of different sensor generations. Currently, third-generation devices are available containing internal digital datasheets of information such as manufacturer and calibration data. The devices use mixed-mode analogue and digital transmission through on-board electronics.

Fourth-generation devices are being developed. These sensors are processor-based and will be characterised by bi-directional command and data communication, all digital transmission, local digital processing, pre-programmed decision algorithms, user-defined algorithms, internal self-verification/diagnosis, compensation algorithms, on-board storage and extensible sensor object models.

Staszewski [47] presents an overview of the suitability of emerging sensor technologies for operational load monitoring and damage detection in airframe structures. Sensor technologies viable for on-line damage monitoring include

acoustic emission, optical fibre sensors, Lamb wave techniques and acousto-ultrasonic sensors.

LDVs are very suitable for in-operation fan blade vibration measurements as they are non-contact devices. Farrar et al. [15] note that the LDV is very useful in field modal tests of the mounting time associated with traditional transducers such as accelerometers is eliminated. The authors also report on a project involving the field-testing of a wind turbine blade using a LDV and a Natural Excitation Technique (NExT) procedure. At the printing time of the paper, the analysis of the project was not yet completed.

Lomenzo et al. [30] introduce a self-tracking laser vibrometry system for rotating fans. This would be an ideal solution for use in this dissertation as this system is non-contact. However, the costs involved make this system not viable.

1.8.4.   Available Systems

There are quite a number of telemetry systems available for signal transmission from a rotating structure. A few of these are presented below.

Microstrain features the wireless Micro Datalogging Transceiver that is configured for conventional strain gauges. The system has a transmission range of up to 30 m with up to 1000 Hz bandwidths and has up to 8 input channels with 10 bits digital resolution. The transceiver has a storage capacity of up to 1 million data points and can operate with a 3.6 V lithium battery for up to 95 hours. The system can be upgraded in terms of measuring bandwidth (up to 10 kHz per channel) and storage capacity (up to 4 million data points) and can be modified for use with piezoelectric accelerometers. The costs of these upgrades unfortunately render the system unsuitable for this dissertation.

Krauss Messtechnik has a number of available wireless systems. One of these is the MT32 system with a measurement bandwidth of up to 3000 Hz for four channels with a 12-bit resolution. Power supply to the system can occur by means of inductive power supply, thus eliminating the need of batteries. Transmission distance is limited to a maximum of 0.5 m. The system is configurable for strain gauges, piezoelectric transducers, thermocouples and voltage inputs. Unfortunately, costs again render this system unsuitable.

Haase and Drumm [22] report on the HiBand Vibration Measurement System from ExSell that was developed for blade vibration sensing in gas turbine engines with a measurement bandwidth of up to 20 MHz. This is not a wireless system and uses a capacitive measuring system that can measure individual blade vibrations, Time-of-Arrival, radial vibration, blade tip clearance and change in rotor centre of mass. The

system provides advance warning of a blade crack, foreign object damage and other engine anomalies. This system unfortunately falls outside the budgetary boundaries of this dissertation.

M-Tek has a 20-way capsule slip ring assembly namely the C-20 Slip Ring Assembly. It has a minimum life span of 12 million revolutions and a recommended maximum rotational speed of 600 rpm. As this system was used by Smit [45] and was subsequently freely available, it was decided to use it for signal transmission for this dissertation.

1.9. Neural Networks

Boek et al. [4] describe their approach to the application of intelligent information processing in large engineering systems for machine condition monitoring, making use of in-operation vibration signals. According to them this technique involves machine specification, signature recording, data acquisition, feature analysis, condition analysis and recommendations.

These researchers performed on-line condition monitoring of an oscillating desktop fan for different damage modes such as load imbalance, shaft imbalance and a cracked blade. The transducers used were two accelerometers attached to the fan motor cover. They were positioned in the radial and axial planes of the shaft.

According to Boek et al. [4] spectra of vibration data are to a large extent contaminated by noise for rotating machines. It is also known that important information is carried in the amplitudes of the rotational frequency and its associated harmonics. In some of the experiments, the authors made use only of the peak values of the rotational frequency harmonics as a representation of the fan condition, drastically reducing the dimensionality of the neural network input space. As it is virtually impossible to determine precise feature values characterising a specific machine condition beforehand, trying different combinations of harmonics, and observing which appeared to vary the most for different fan conditions determined the features selected for the experiments.

Training of the network was conducted using a back-propagation algorithm. The network consisted of a single hidden layer containing between 5 and 20 processing units. The learning rate was fixed at 0.02 and the momentum control parameter at 0.9. Best results were obtained in the detection of imbalance, but the classification thereof was in general poor. Good results were obtained for distinguishing between physically different faults such as imbalance versus blade crack. The network could however not classify the state where both an imbalance and a blade crack were present. A network making use of overall values as inputs performed a bit better.

Boek et al. [4] recommend that further work in extracting better features could lead to improved performance.

Farrar and Sohn [16] view vibration based structural health monitoring fundamentally as a process of statistical pattern recognition composed of four portions namely operational evaluation, data acquisition and cleansing, feature selection and data compression, and statistical model development for feature discrimination. The basic premise of vibration-based damage detection is that damage will significantly alter certain properties of a system, such as the structural stiffness. This system property change will in turn alter the dynamic response of the system.

Inherent in the feature selection portion of the process, is the condensation of the data. Farrar and Sohn [16] note that robust data reduction techniques must retain sensitivity of the chosen features to the structural changes of interest in the presence of environmental noise. Features used for damage detection are application specific.

Farrar and Sohn [16] note that many reported studies for rotating machinery damage detection applications exist where statistical models have been used to enhance the damage detection process. There are different classes of algorithms used in statistical model development namely supervised learning and unsupervised learning. Supervised learning refers to the case where data from both the undamaged and damaged structures are available. Unsupervised learning refers to the case where data of only the undamaged structure is available.

The damage state of a structure is described as a five-step process: Damage existence, location, type, extent and prediction. Damage existence and location can be obtained from experimental structural dynamics techniques. Damage type identification can only be done when data from structures with the specific damage cases are available. According to Farrar and Sohn [16], analytical models are usually needed to determine damage extent and remaining life predictions. For the specific case of damage in the form of a crack, remaining life predictions can be calculated using fatigue crack growth principles when the crack growth rates and structural nominal stresses are known.

Farrar and Sohn [16] note that it is important for the statistical model to be tested on actual data. False identifications of damage fall into two categories namely false-positive and false-negative damage indications. False-positive damage indication refers to the case where damage is indicated when none is present. False-negative damage indication refers to the case where no indication of damage is given when damage is actually present.

Marwala [33] presents a committee of neural networks technique, which in essence is the use of a number of independent neural networks in parallel. In this case, three independent back-propagation or multi-layer perceptron neural networks were trained using frequency response functions, modal properties and wavelet transforms. This method was tested for a three degree of freedom mass-spring-damper system and was also implemented for damage identification in a population of ten seam-welded cylindrical shells.

Marwala [33] found the committee of neural networks to identify damage cases better than the three approaches, i.e. frequency response functions, modal properties and wavelet transforms, used individually.

Lew [27] presents a neural network approach to structural damage detection based on transfer function correlation. This approach requires only a few sensors as opposed to general finite element model updating techniques. This gives the approach certain benefits such as reduced experimental hardware costs and increased effectiveness for on-line health monitoring and data processing.

Waszczyszyn and Ziemianski [52] made use of a back-propagation neural network for notch location detection in an experimental steel cantilever beam. Natural frequencies, extracted from FRFs, were used as inputs to the neural network. The results from the experimental setup are compared to that obtained from a FEM. Both yielded good results.

Castellini and Revel [9] used a scanning LDV in conjunction with neural networks to detect, localize and characterize defects in structures. The authors made use of features extracted from numerically calculated FRFs of FEMs to train the networks. The technique was successfully applied to an aluminium plate, a composite fibreglass panel and a Byzantine icon of the 17th century. Castellini and Revel [9] note that laser vibrometry seems to be the only suitable measurement technique to be used with the processing algorithms they developed due to its ability to quickly supply vibration data in a wide frequency bandwidth with high spatial resolution.

1.10. Scope of Work

The main aim of this research is to develop a methodology for on-line fan blade damage detection and identification using neural networks and a minimum number of sensors.

13

Use will be made of a laboratory test structure namely the FaBCoM TeSt to develop such a methodology. A FEM of the FaBCoM TeSt will be developed to determine the feasibility of using GMSF shifts for damage quantification and qualification for single and multiple damaged blades. The results of this analysis will be used to help identify GMSFs that are sensitive blade damage indicators. The FEM will be verified by means of an EMA of the FaBCoM TeSt.

Measurements will be taken for several blade damage levels for single and multiple damaged blades for several sensor locations. Neural networks will then be trained for the task of damage identification. Two different approaches will be used with regards to network training. For the first approach, features from the measured data will be identified and extracted for neural network training. The neural networks will be used to determine whether it is feasible for a sensor installed on one blade, to quantify and qualify damage on other blades.

Secondly, the feasibility of using numerically calculated FRFs of the FEM for training a neural network to be used on the experimentally measured data will be determined. This is a crucial part of the dissertation in terms of the practical significance of the dissertation. It is much more desirable to train networks from computer generated features than to artificially damage the actual structure in terms of costs.

In detail, the scope of work for this dissertation can be laid out as follows:

- The development of an extensive FEM. Smit [45] made use of a FEM of a single blade to determine the sensitivity of local blade natural frequencies to local blade damage. In this dissertation, the concern lies with the sensitivity of GMSFs to local blade damage. For this reason, a more extensive FEM consisting of the FaBCoM TeSt shaft, hubs and four blades will be developed.

- A feasibility study of the use of GMSF shifts for damage quantification and qualification. This will be done by performing modal analyses on the FEM for different conditions such as rotational velocity, operating temperature, blade damage scenario and blade damage level. The reason for the inclusion of some operational variables namely rotational velocity and operating temperature is to study their effect on GMSFs in order to determine whether monitoring of the frequencies is practically feasible.

- The identification of suitable GMSFs from the above-mentioned study for damage quantification and qualification. Typically, a GMSF of interest here will be one that is relatively insensitive to operational variables, but at the same time is a good indicator of damage level and location.

- The validation of the FEM by means of an EMA. As this FEM is intended to be used to predict GMSF shifts as a result of blade damage as well as to provide features for neural network training, it has to be validated with the actual structure. The MAC matrix will typically serve as a measurement of FEM and FaBCoM TeSt correlation.

- The identification of a suitable data or signal transmission system. This will be a system that has as little as possible influence on behaviour of the structure. It must also be able to facilitate measurements with the identified measurement bandwidth.

- Measuring data on the FaBCoM TeSt for different blade damage scenarios and sensor location scenarios. Transducers used will be three piezoelectric strain sensors installed on three of the four blades for strain measurements and a single piezoelectric accelerometer for rotational acceleration measurements. Taking measurements at different sensor locations, it will be possible to determine whether it is feasible using a sensor installed on one blade, to measure changes due to damage in another blade.

- A feasibility study of the use of neural networks for blade damage level detection using previously measured data. This will be done on the measurements taken by Smit [45] for a single damaged blade.

- The development of an experimentally supervised neural network damage detection methodology. This will include the following:

   o Identification of features suitable for neural network training with experimental supervision. These features will mostly include the identified frequencies, but can also include other features such as those obtainable from time domain analysis.

   o Identification of suitable neural network architecture. Use will be made of the architecture used by Boek et al. [4] as a guideline although the quality of results from the networks will be the final determining factor.

   o The neural networks will be trained and tested for the different sensor locations at certain damage levels. The abilities of the networks to do damage level interpolation as well as extrapolation will also be determined. The networks will be tested for damage levels between the levels trained for in order to determine their damage level interpolation abilities. The damage level extrapolation abilities will

also be tested using data recorded for additional blade damage. These abilities will serve as a guideline of the number of damage levels and scenarios the networks need to be trained for in order to yield accurate results.

- The development of a numerically supervised neural network damage detection methodology. This will include the following:

  o FEM FRF generation for the same damage cases as will be simulated in testing of the FaBCoM TeSt. FRFs will be calculated for a single force input similar to that used on the FaBCoM TeSt in the EMA. The outputs used will be similar to those measured in the experimental testing of the FaBCoM TeSt in terms of measurement location and orientation as well measurement type (e.g. strain or acceleration).

  o Feature identification from the FEM FRFs. Features will be selected on the basis of correlation with experimental features. If a sufficient number of features are identified, a neural network will be trained on the numerical features and then tested using the experimental features.

Chapter 2   Initial FaBCoM TeSt Finite Element Model

2.1. Purpose

This dissertation is concerned with the development or formulation of a methodology for on-line fan blade damage detection. In order to formulate such a methodology, tests will be done on a laboratory test structure referred to as the FaBCoM TeSt.

In this chapter, a FEM of the FaBCoM TeSt is presented. Smit [45] made use of a FEM of a single fan blade for his dissertation concerning on-line blade damage detection for a single blade. Smit developed the technique using one sensor per blade and concluded that in order to make use of less than one sensor per blade, GMSFs in conjunction with neural networks will need to be used. For this reason, it was decided to develop a more extensive FEM of the FaBCoM TeSt.

This FEM will be used for several purposes namely
- A feasibility study of multiple blade damage detection using GMSFs.
- The identification of GMSFs suitable for experimental on-line damage detection for multiple blades.
- The numerical generation of FRFs for different blade damage levels and cases. Features of the FRFs will be used for training a neural network for damage detection on the FaBCoM TeSt.

Blade damage will be defined as the percentage of blade root crack length to total blade width in this dissertation.

2.2. Fan Blade Condition Monitoring Test Structure

The FaBCoM TeSt was originally named the Experimental Fan Blade Damage Simulator by its designer Smit [45]. The FaBCoM TeSt basically consists of four simple blades with variable pitches, an aluminium and a steel hub as well as a rotor with two radial roller element bearings and a drive pulley. A computer generated isometric assembly drawing of these parts except for the drive pulley is shown in Figure 2-1.

The blades are attached to the aluminium hub which in turn is attached to the rotor by means of the steel hub. These are enclosed by a steel structure and grid for safety reasons as shown in Figure 2-2. The rotor and its bearings are enclosed in a bearing housing that is attached to the steel structure. Drive of the FaBCoM TeSt occurs by means of a fan belt driven by a three phase 1.5 kW electric motor. This is shown in Figure 2-3. The speed of the electric motor is controlled by an AC Tech Variable Speed AC Drive.
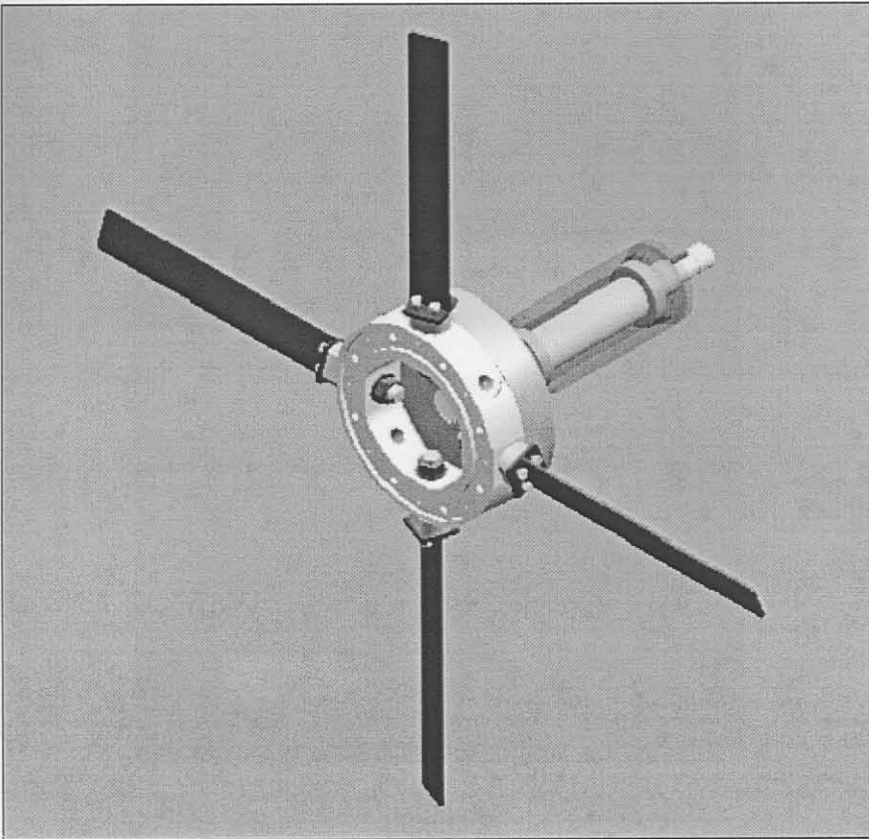
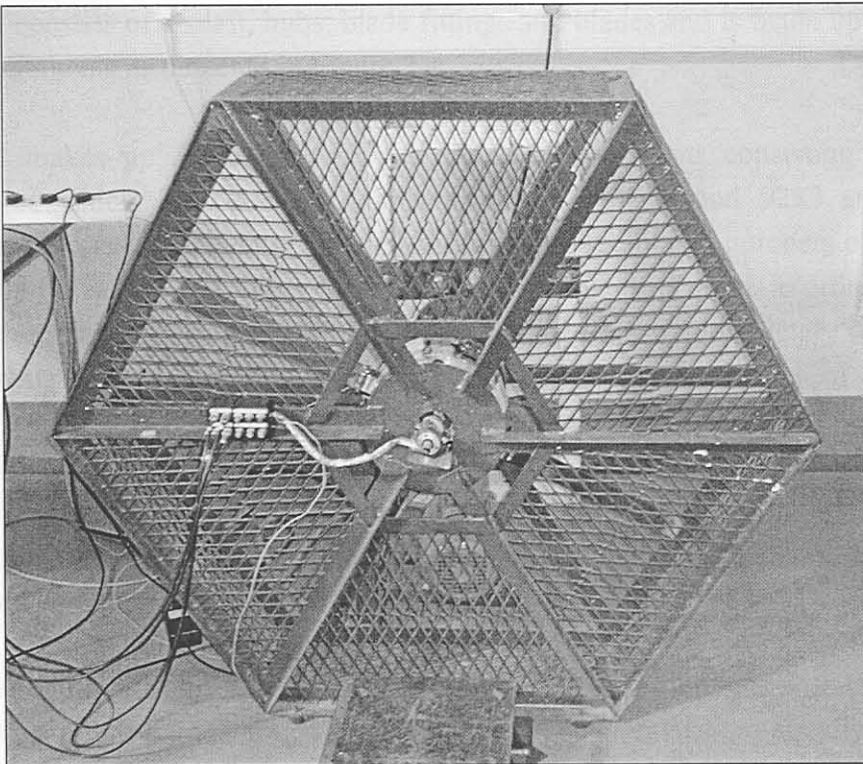**Figure 2-1: FaBCoM TeSt Rotor Assembly Isometric Drawing**
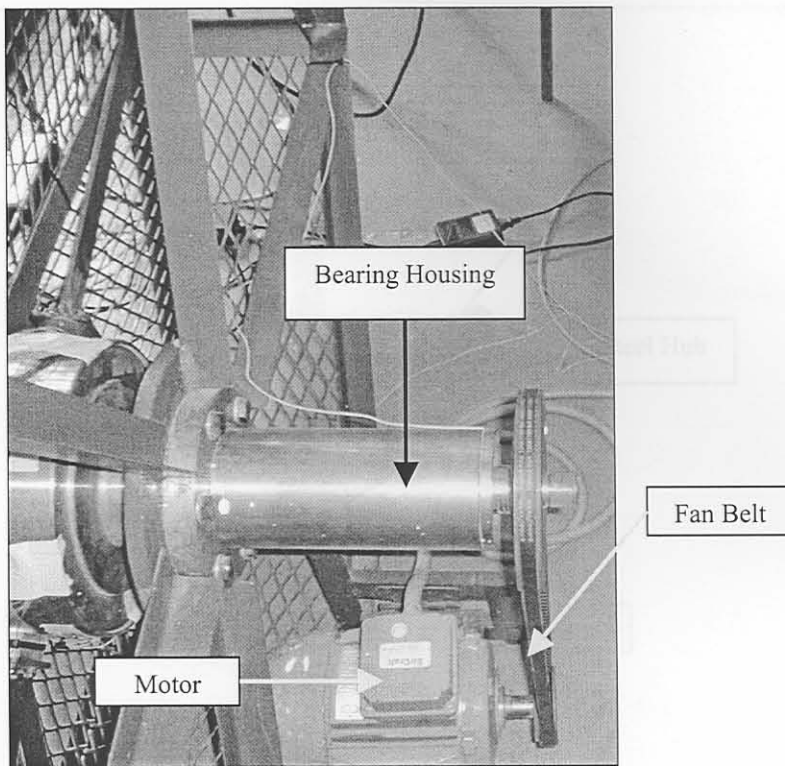

Figure 2-2: FaBCoM TeSt Enclosure

Figure 2-3: FaBCoM TeSt Fan Belt Drive

2.3. *Finite Element Model Description*

The FEM consists of a shaft, hubs, blade fittings and blades and is made up by a total of 13384 elements as depicted in Figure 2-4.

The shaft makes up the biggest part of the model elements consisting of 11464 elements of which 2160 are 8 node hexahedral elements and 9282 are 6 node pentahedral or wedge elements. The reason for using such large numbers of elements is to satisfy the default reliability thresholds as laid down by Patran, in order to obtain accurate results. Still, the reliability thresholds could not be completely satisfied as 113 elements exceed the Edge Angle threshold of 30° by a maximum of about 2.6° and 199 elements exceeds the Face Skew threshold of 30° by a maximum of also about 2.6°.

The aluminium hub consists of 1200 eight node hexahedral elements that satisfy all the Patran element reliability thresholds.

Each blade is made up of 120 four-node quadrilateral shell elements with the element dimensions of each blade being 4 x 30 elements. The elements are equally spaced in the blade width but not in the blade length as the element mesh is finer towards the blade root. Each blade fitting consists of 60 eight-node hexahedral elements. A 10° blade angle is obtained by twisting the hexahedral elements. All these elements satisfy the Patran element reliability thresholds.
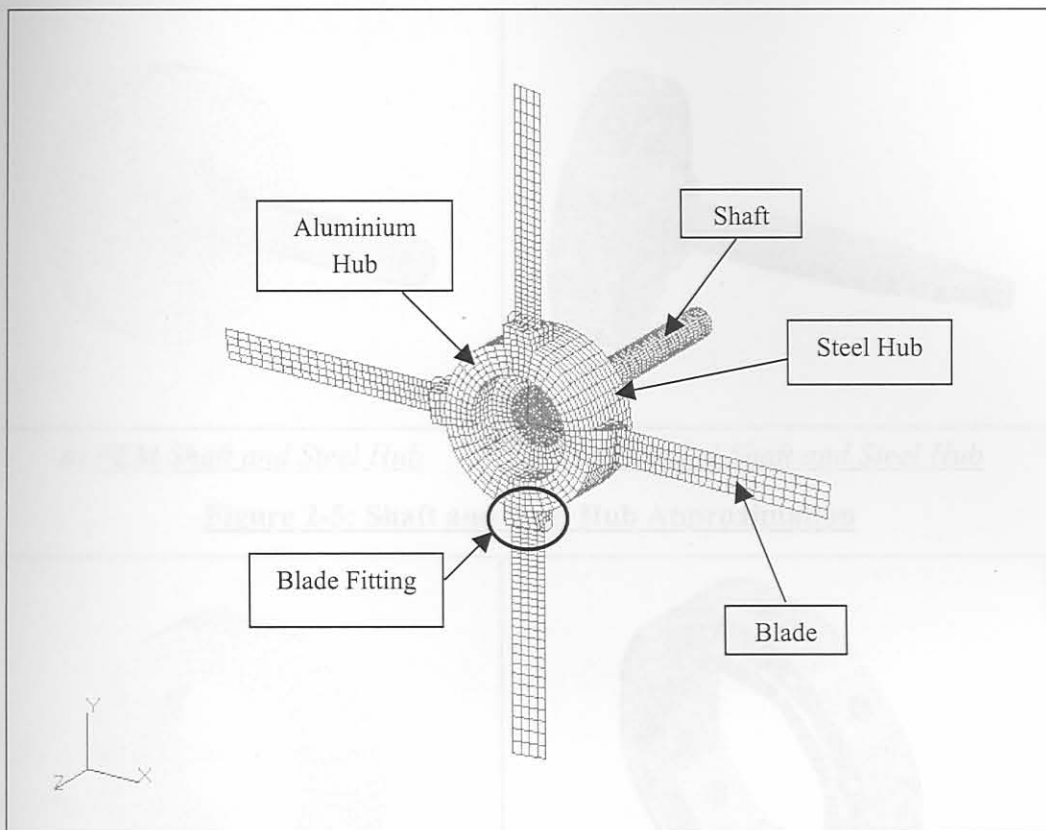
Figure 2-4: FaBCoM TeSt Finite Element Model

The choice of the specific elements used in the model was made on the basis of model simplicity. It was decided to make use of the simplest forms of the elements, as the element meshes were already more than fine enough to yield accurate results. All the elements used are suitable for static, modal and frequency response analyses ([37]).

2.4. Geometrical Approximations

The FEM is to a large extent a geometrical approximation of the FaBCoM TeSt. The shaft used in the FEM is a simple cylindrical approximation of the actual shaft as shown in Figure 2-5. The shaft diameter used in the FEM is 45 mm, which is the FaBCoM TeSt shaft diameter at the bearing locations.

The FEM aluminium hub is a ring approximation of the actual hub as shown in Figure 2-6. A comparison between the actual and approximated blades and blade attachments can be seen in Figure 2-7.

The edge quadrilateral shell elements at the blade roots are connected to the hexagonal elements of the blade fitting by making use of Multi-Point Constraints (MPCs) as shown in Figure 2-8:
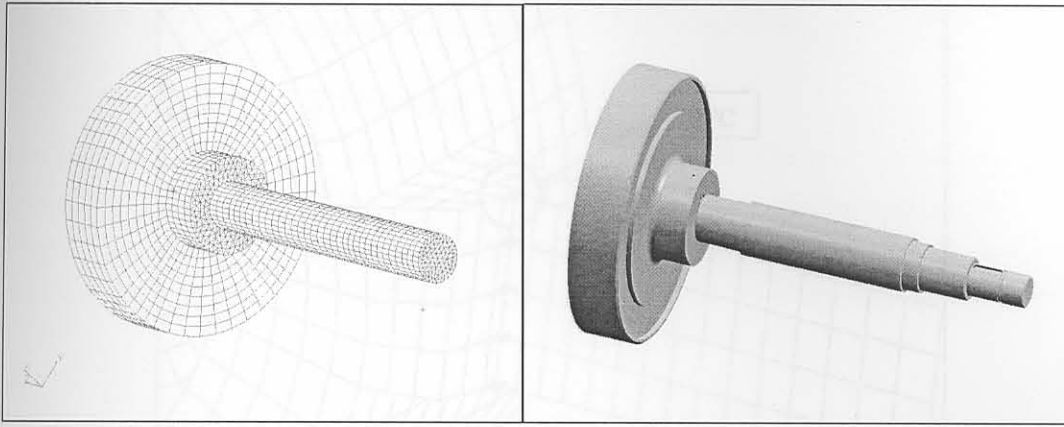
a) *FEM Shaft and Steel Hub*   b) *Detailed Shaft and Steel Hub*

Figure 2-5: Shaft and Steel Hub Approximation
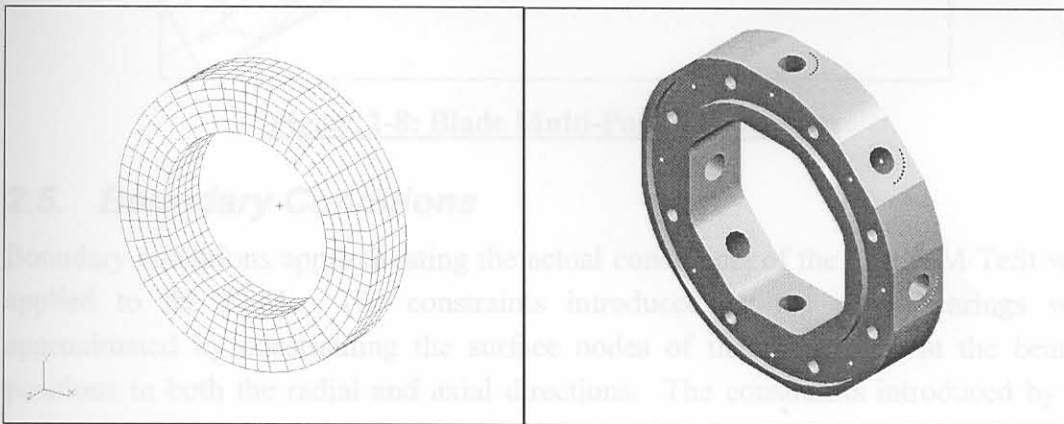
a) *FEM Aluminium Hub*   b) *Detailed Aluminium Hub*

Figure 2-6: Aluminium Hub Approximation
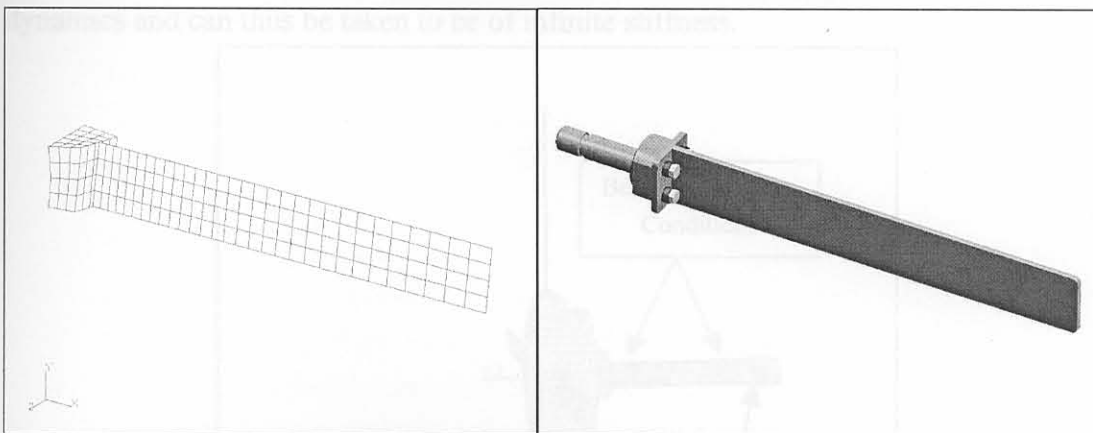
a) *FEM Blade and Fitting*   b) *Detailed Blade and Fitting*

Figure 2-7: Blade and Fitting Approximation

b163372zo
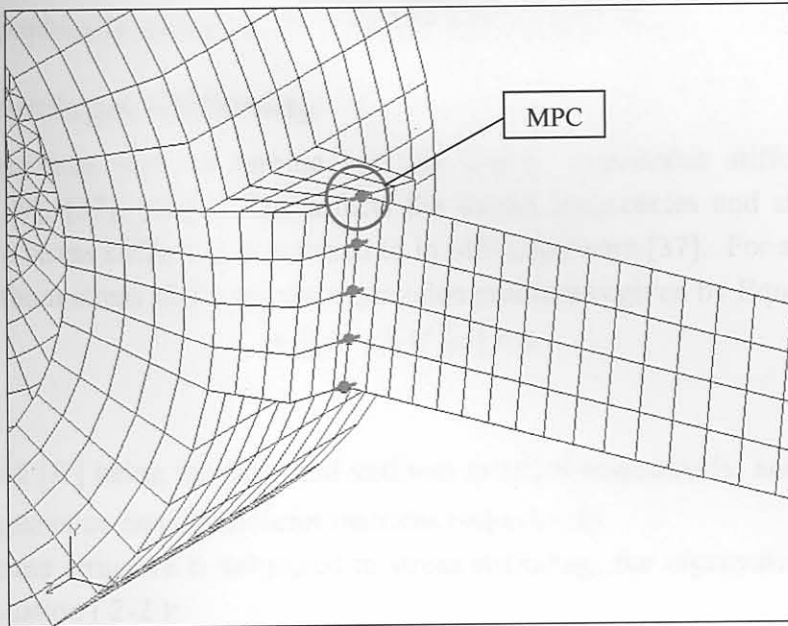
Figure 2-8: Blade Multi-Point Constraints

2.5. Boundary Conditions

Boundary conditions approximating the actual constraints of the FaBCoM TeSt were applied to the FEM. The constraints introduced by the shaft bearings were approximated by constraining the surface nodes of the FEM shaft at the bearing positions in both the radial and axial directions. The constraints introduced by the pulley were approximated by constraining the surface nodes of the FEM shaft in all 6 degrees of freedom. It must be noted that the assumption is made here that the stiffness of the belt used for driving the fan does not contribute to the structure dynamics and can thus be taken to be of infinite stiffness.
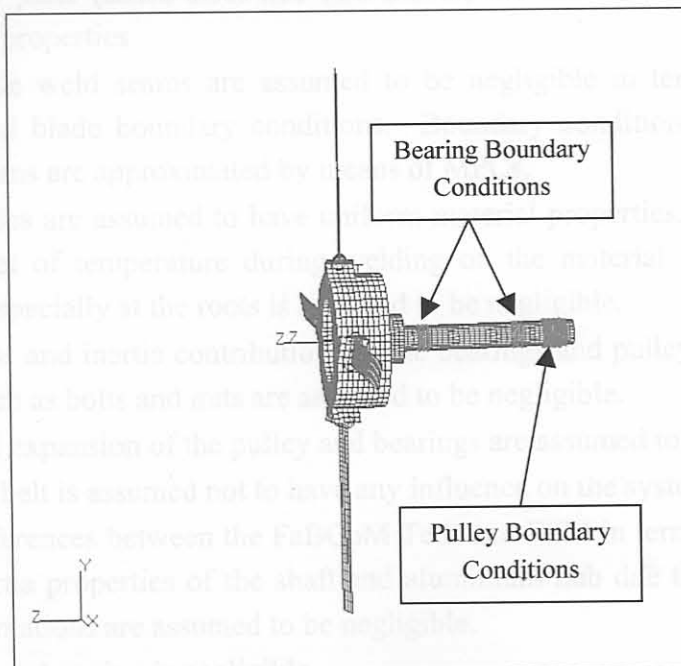
Figure 2-9: Finite Element Model Boundary Conditions

Figure 2-9 graphically represents the FEM boundary conditions.

2.6. *Centrifugal Stiffening*

Rotating structures such as turbine and fan blades, experience stiffening during operation ([29], [37], [48]). This affects the modal frequencies and shapes of the blades due to stress stiffening as referred to in MSC.Software [37]. For an undamped structure without stress stiffening the eigenvalue problem is given by Equation (2-1):

$$[K]\{\psi\} - \lambda[M]\{\psi\} = 0$$

(2-1)

with $[M]$ and $[K]$ being the mass and stiffness matrices respectively, and λ and $\{\psi\}$ being the eigenvalue and eigenvector matrices respectively.

When the same structure is subjected to stress stiffening, the eigenvalue problem is given by Equation (2-2):

$$([K] + [K_g])\{\psi\} - \lambda[M]\{\psi\} = 0$$

(2-2)

with $[K_g]$ the geometric stiffness matrix calculated by means of the Theory of Elastic Stability.

Fortunately, it is very easy to implement centrifugal stiffening in Patran.

2.7. *Assumptions*

This section summarizes the assumptions made during the FEM construction:

- All steel parts (shaft, steel hub and blades) are assumed to have the same material properties
- The blade weld seams are assumed to be negligible in terms of mass and additional blade boundary conditions. Boundary conditions applied by the weld seams are approximated by means of MPCs.
- The blades are assumed to have uniform material properties. In other words, the effect of temperature during welding on the material properties of the blades especially at the roots is assumed to be negligible.
- The mass and inertia contributions of the bearings and pulley as well as other parts such as bolts and nuts are assumed to be negligible.
- Thermal expansion of the pulley and bearings are assumed to be negligible.
- The fan belt is assumed not to have any influence on the system dynamics.
- The differences between the FaBCoM TeSt and FEM in terms of the stiffness and inertia properties of the shaft and aluminium hub due to the geometrical approximations are assumed to be negligible.
- Structural damping is negligible.

23

Chapter 3 Numerical Global Mode Shape Frequency Sensitivity Analysis

3.1. Purpose

The purpose of the GMSF sensitivity analysis on the FEM was in the first place to investigate the feasibility of damage quantification and qualification in a fan assembly by making use of the frequency shifts of global mode shapes. Secondly, it was used to identify certain GMSFs that may be useful in damage detection of the FaBCoM TeSt during testing.

The influences of several operational variables on GMSF shift were studied in order to identify GMSFs that are not only insensitive to these variables, but are also good indicators of damage location and extent. The variables used in the analysis included temperature, accumulated debris mass and rotational velocity. Different damage case scenarios in terms of number and position of cracked blades were also considered.

This analysis will be done by performing modal analyses on the FEM for each of the different variables and then comparing the obtained GMSFs for each set of results.

3.2. Description

For each operational condition variable, numerical modal analyses were performed on the FEM over a 2 kHz bandwidth for different levels of damage in the east blade (see Figure 3-1) at 0%, 25% and 50% damage. The damage level of an individual fan blade is defined in this dissertation as the percentage of blade root crack length of the total blade width.

3.2.1. Material Properties

Initially, the modal sensitivity analysis was performed for material properties obtained from Benham et al. [3] for carbon steel and aluminium alloy. These properties are listed in Table 3-1 for the FEM before and after model updating.

Table 3-1: Material Properties Used in FEM

Material Name	Pre/post Model Updating	Young's Modulus [GPa]	Density [kg.m^{-3}]	Temperature Expansion Coefficient [x10^{-6}.$^{\circ}$C^{-1}]	Poisson's Ratio
Steel	Pre	208	7850	12	0.3
	Post	192.6	7756.3	12	0.3
Aluminium	Pre and Post	70	2710	23	0.33

It was discovered that the modal frequencies obtained from the FEM modal analysis were rather quite sensitive to material properties. For this reason, model updating was performed in terms of material property updating for all the FEM elements to which the steel properties were assigned. The specific material properties updated were Young's modulus and material density.

The procedure of experimentally determining these material properties is described in Chapter 4.
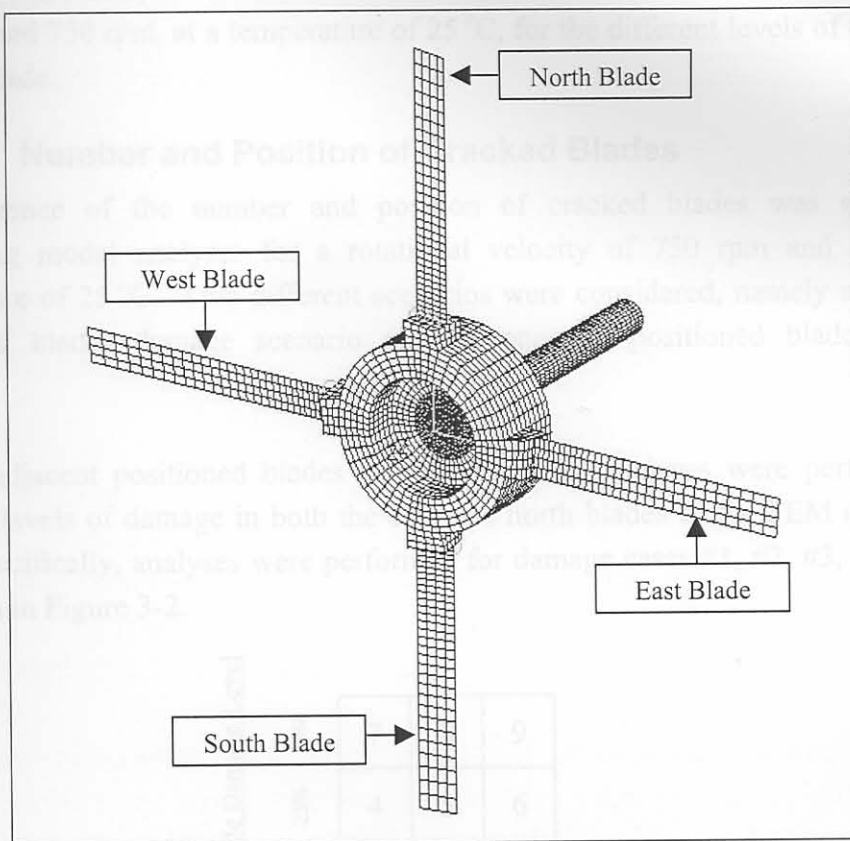
Figure 3-1: Blade Naming on FEM

3.2.2.   Thermal Sensitivity

Thermal sensitivity was investigated by performing modal analyses for three different levels of temperature namely 25 °C, 50 °C and 75 °C at a rotational velocity of 750 rpm, for the different damage levels of the east blade.

3.2.3.   Debris Mass Sensitivity

The purpose of this part of the analysis was to determine the effect of accumulated debris on modal frequencies. As a first approach, analyses were run for single point masses added to the leading tip of each blade. The masses used were 2.1 g, 4.2 g and 6.3 g, with 2.1 g being the mass of a typical accelerometer such as used in the EMA.

As obtained from Garnett-Bennett [19], debris mass accumulation on an actual fan found at Majuba Power Station is negligible at a maximum of 40 g spread over the

25

lower third surface area of a fan blade, taking into account that the length of a single blade is over 0.7 m. However, this part of the analyses did prove useful as added point masses showed rather noticeable frequency shifts. This was taken into account when the experimental modal analysis was performed.

3.2.4.   Rotational Velocity Sensitivity

This part of the analysis was performed for different rotational velocities of 150 rpm, 450 rpm and 750 rpm, at a temperature of 25 °C, for the different levels of damage of the east blade.

3.2.5.   Number and Position of Cracked Blades

The influence of the number and position of cracked blades was studied by performing modal analyses for a rotational velocity of 750 rpm and a material temperature of 25 °C. Two different scenarios were considered, namely an adjacent positioned blades damage scenario and an opposite positioned blades damage scenario.

For the adjacent positioned blades damage scenario, analyses were performed for different levels of damage in both the east and north blades of the FEM (see Figure 3-1). Specifically, analyses were performed for damage cases #1, #2, #3, #5, #6 and #9 shown in Figure 3-2.

Figure 3-2: Adjacent Positioned Blades Damage Case Matrix

The reason why only these six damage cases are analysed, is that the assumption is made that the frequency shift result matrices are symmetric. In other words, the assumption is made that the analyses for damage cases #2, #3 and #6 will yield the same results as for damage cases #4, #7 and #8 respectively in terms of GMSFs.

For the opposite positioned blades damage scenario, analyses were performed for different levels of damage in the east as well as the west blade (see Figure 3-1). The same damage cases are considered as for the adjacent blade damage scenario, if Figure 3-2 is drawn for west blade damage level on the vertical axis.

3.3. *Ideal Results*

The ideal mode shape will be one of which the frequency shift is independent of operational variables such as rotational velocity and temperature but at the same time is a very good quantifier and qualifier of damage. This means that the GMSF should be sensitive to a specific damage scenario to allow for easy damage detection for that damage scenario. This in turn means that different GMSF should be identified for each damage scenario in order to detect damage for all damage scenarios.

3.4. *Typical Results*

It is not possible to identify fixed trends of the results in terms of sensitivity of mode shape order to damage. However, GMSFs above 240 Hz (global mode shapes #10 and up) are much more sensitive to the considered variables with maximum frequency shifts of 10 Hz and higher. Overall, GMSFs above 1200 Hz (global mode shapes #28 and up) tend to yield the best results in terms of damage sensitivity with a few exceptions being sensitive to rotational velocity and temperature.

The results obtained from the modal sensitivity analysis are graphically represented for four sensitivity parameters namely rotational velocity, temperature, adjacent positioned blades damage levels and opposite positioned blades damage levels in Figure 3-3 to Figure 3-6 for the 4th, 5th, 34th and 35th mode shapes respectively. The results for all the mode shapes within a 2 kHz bandwidth with a maximum absolute frequency shift of at least 10 Hz are given in Appendix B.

Each figure represents the absolute frequency shift for that mode shape relative to that particular mode shape's reference frequency at a rotational velocity of 750 rpm and a temperature of 25 °C for the undamaged case. This is given on the vertical axes as well as the colour bars. All the vertical axes and colour bars are scaled to the maximum frequency shift result for all four variables for each individual mode shape. From the top left, going in a clockwise direction, the frequency shift results are given for the rotational velocity, temperature, opposite positioned blades damage level and adjacent positioned blades damage level variables.

In Figure 3-3 the results for the 4th mode shape with a reference frequency of about 35 Hz is given. The frequency of the 4th mode shape is an example of a GMSF that is much more sensitive to rotational velocity than to the other variables. Other similar mode shapes within a bandwidth of 2000 Hz were found to be mode shapes #1, #2, #3, #6 to #9, #20, #21, #23, #24, #27 and #31. This implies that the frequencies of these mode shapes are more affected by rotational stiffening than damage.

In Figure 3-4, the results for the 5th modal frequency at about 70 Hz, which is first torsional mode of the shaft, are shown. The reason for the temperature dependency of

the mode shape is that the FEM boundary conditions, as discussed in Chapter 2, also constrain the shaft in the axial direction. In other words, the shaft is not allowed to expand in the axial direction as a result of temperature effects at the constrained nodes. This introduces axial stress of the shaft between the constrained nodes, affecting the stiffness of the shaft.
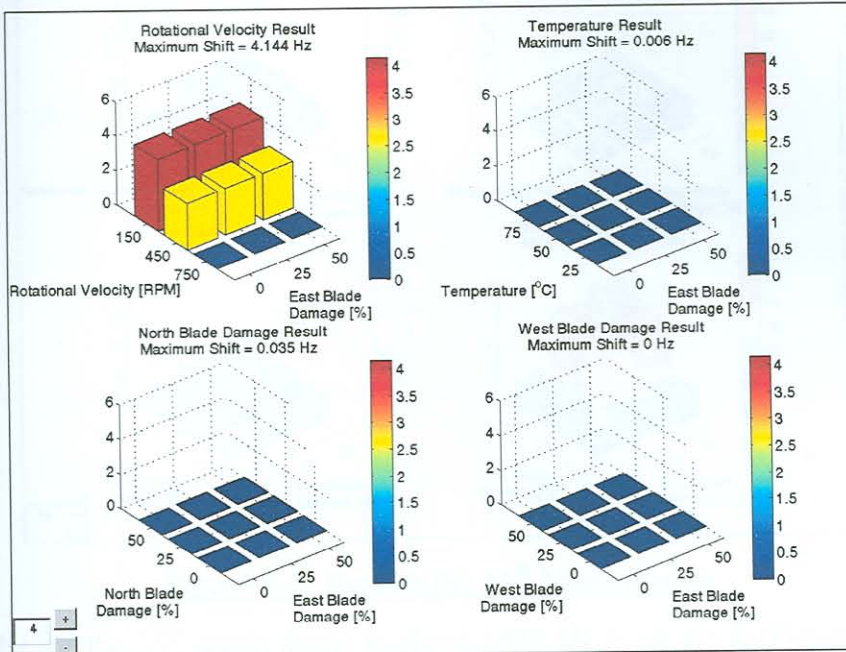
Figure 3-3: Results of 4th Mode Shape
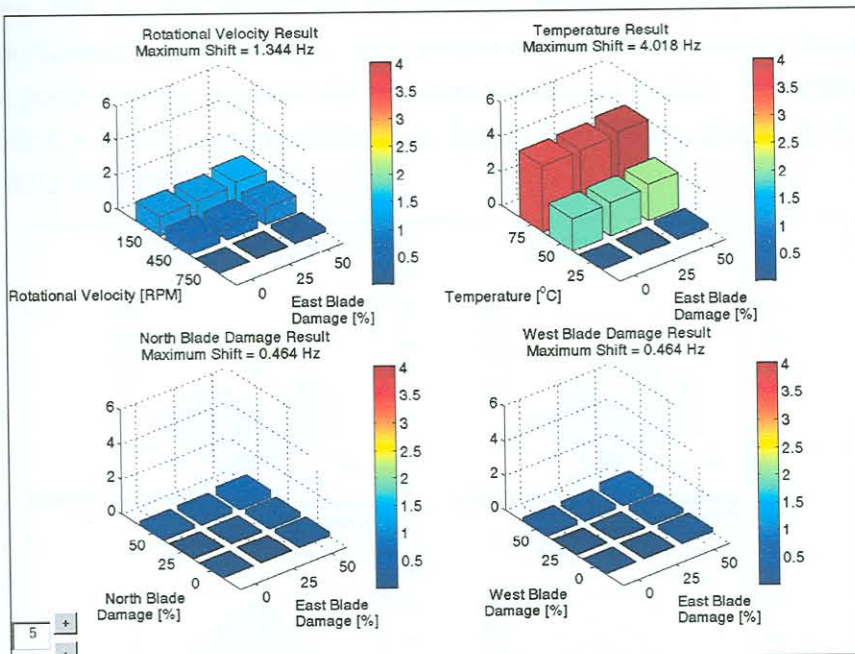
Figure 3-4: Results of 5th Mode Shape

Figure 3-5 shows the results for the 34th mode shape that has a reference frequency of about 1648 Hz. This mode shape is an example of a mode of which the frequency is relatively independent of rotational velocity and temperature, and is more dependant on damage levels for opposite positioned blades than adjacent positioned blades. This

28

makes the frequency of this mode shape a good damage indicator for opposite positioned blades damage. Other similar mode shapes were found to be mode shapes #16, #21, #25, #29, #36 and #40 within a 2000 Hz bandwidth.
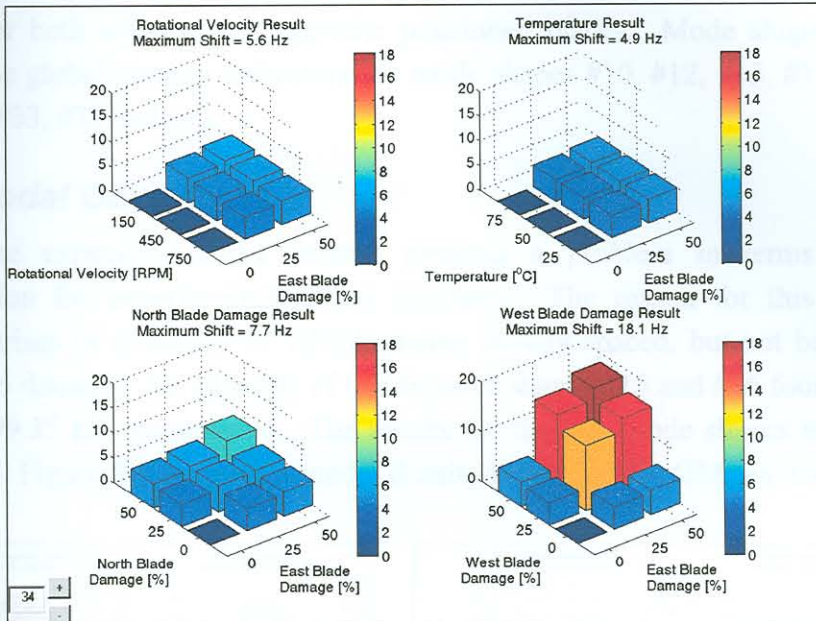
Figure 3-5: Results for 34th Mode Shape

The results for the 35th mode shape at about 1676 Hz is shown in Figure 3-6. This mode shape's frequency is again relatively independent of rotational velocity and temperature, and is more dependent on adjacent positioned blades damage than on opposite positioned blades damage. This means that the mode shape's frequency is in this case a good damage indicator for adjacent positioned blades. Other similar mode shapes within a 2000 Hz bandwidth were found to be mode shapes #11, #14, #18, #22, #26, #30, #37, #39 and #41.
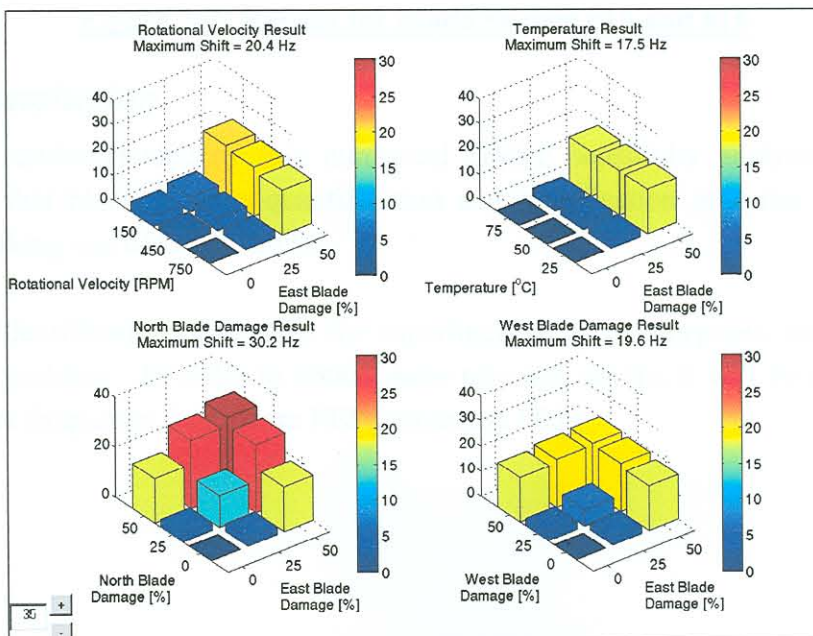
Figure 3-6: Results for 35th Mode Shape

29

Some mode shape frequencies were found to be good global structural damage indicators. In other words, these mode shapes' frequencies are again relatively independent of rotational velocity and temperature, and are dependent equally of damage for both adjacent and opposite positioned blades. Mode shapes that were found to be global damage indicators are mode shapes #10, #12, #13, #15, #17, #19, #28, #32, #33, #38 and #42.

3.5. Modal Density

As can be expected, modal density presents a problem in terms of GMSF identification for experimental testing purposes. The reason for this is that the situation arises of a number of GMSFs being closely spaced, but not being equally sensitive to damage. An example of this is mode shapes #15 and #16 found at 399.08 Hz and 399.35 Hz respectively. The results for the two mode shapes are shown in Figure 3-7. Figure 3-8 presents a modal density histogram for GMSFs using bin sizes of 10 Hz:

a) *Mode Shape #15*   b) *Mode Shape #16*
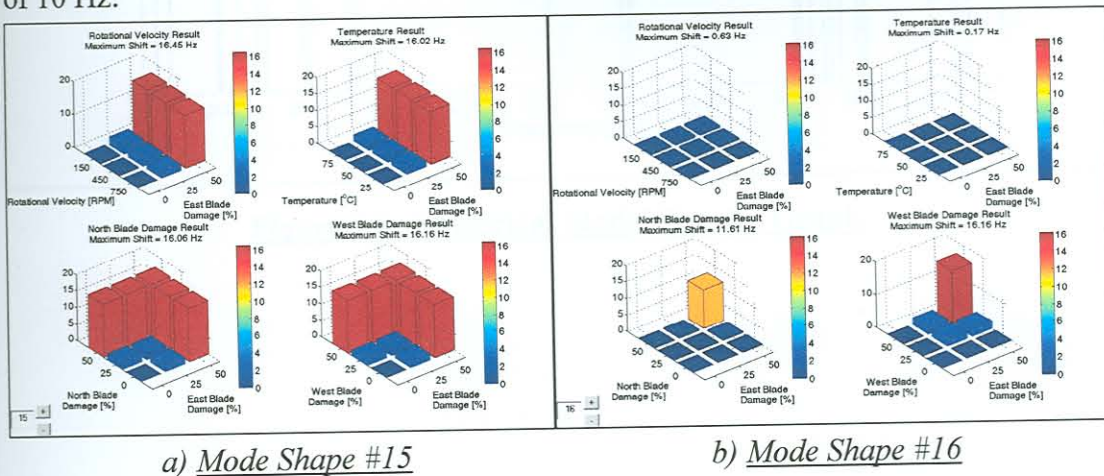
Figure 3-7: Results for Mode Shapes #15 and #16

3.6. Conclusion

From the results yielded by this numerical GMSF sensitivity analysis, it can be concluded that blade damage quantification and qualification of a fan assembly is feasible making use of GMSF shifts.

As to the identification of GMSFs for experimental testing purposes, modal density presents a problem. In order to obtain more relevant results, it will be necessary to look at peak frequency shifts from FEM generated FRFs.
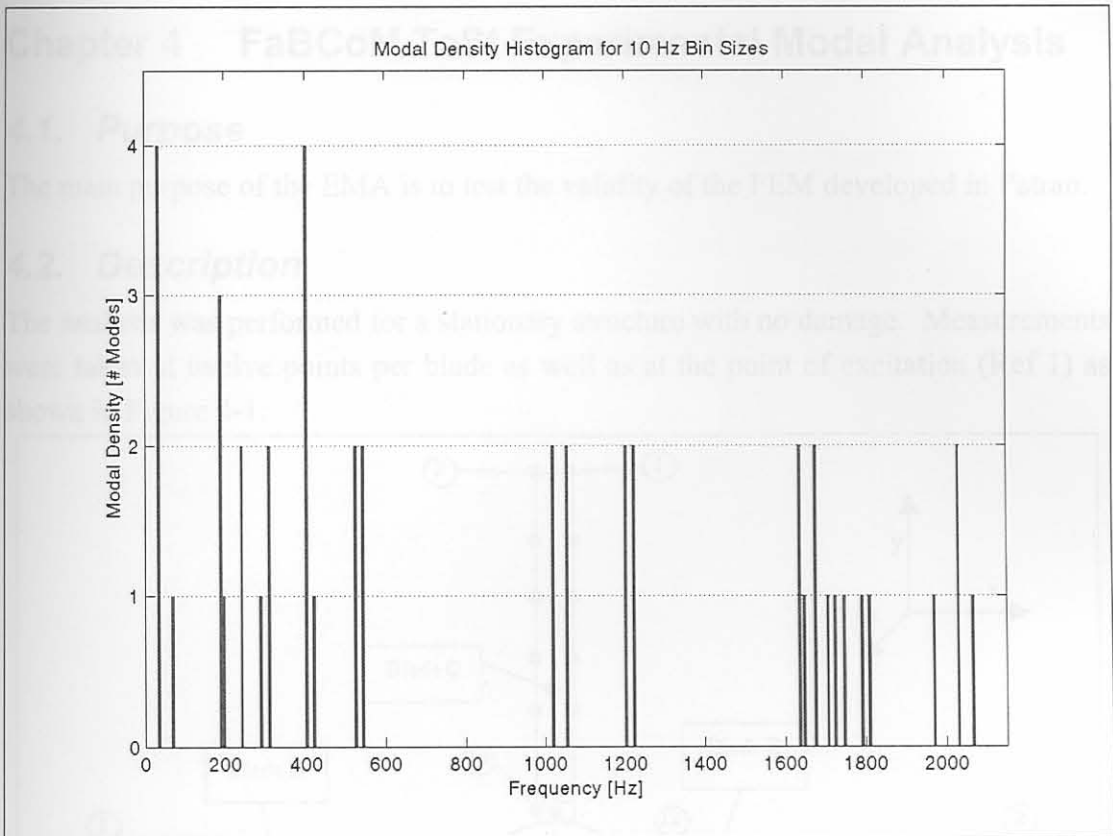
Figure 3-8: Numerical Modal Density Graph

Chapter 4   FaBCoM TeSt Experimental Modal Analysis

4.1. Purpose

The main purpose of the EMA is to test the validity of the FEM developed in Patran.

4.2. Description

The analysis was performed for a stationary structure with no damage. Measurements were taken at twelve points per blade as well as at the point of excitation (Ref 1) as shown in Figure 4-1:
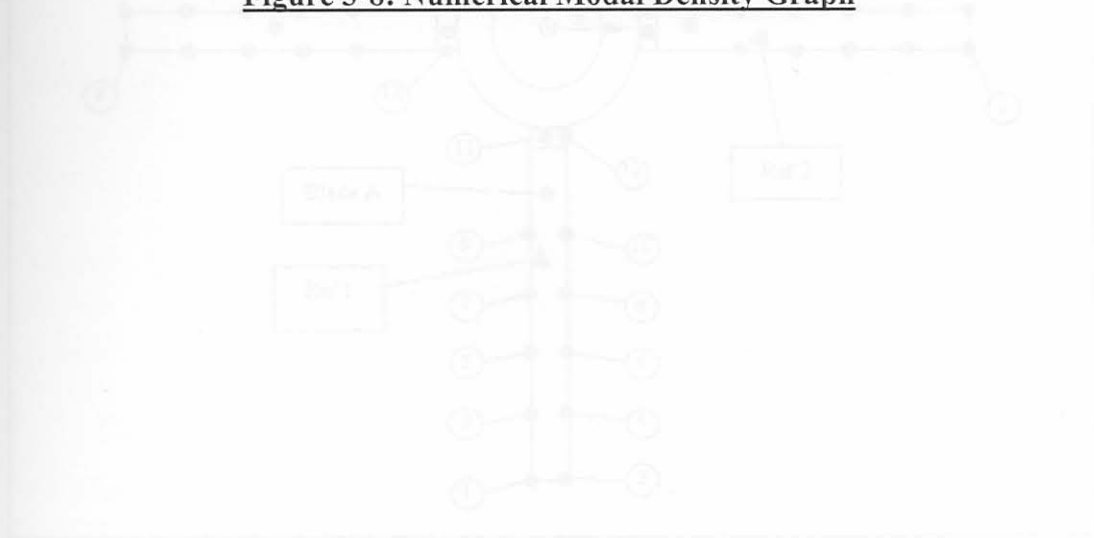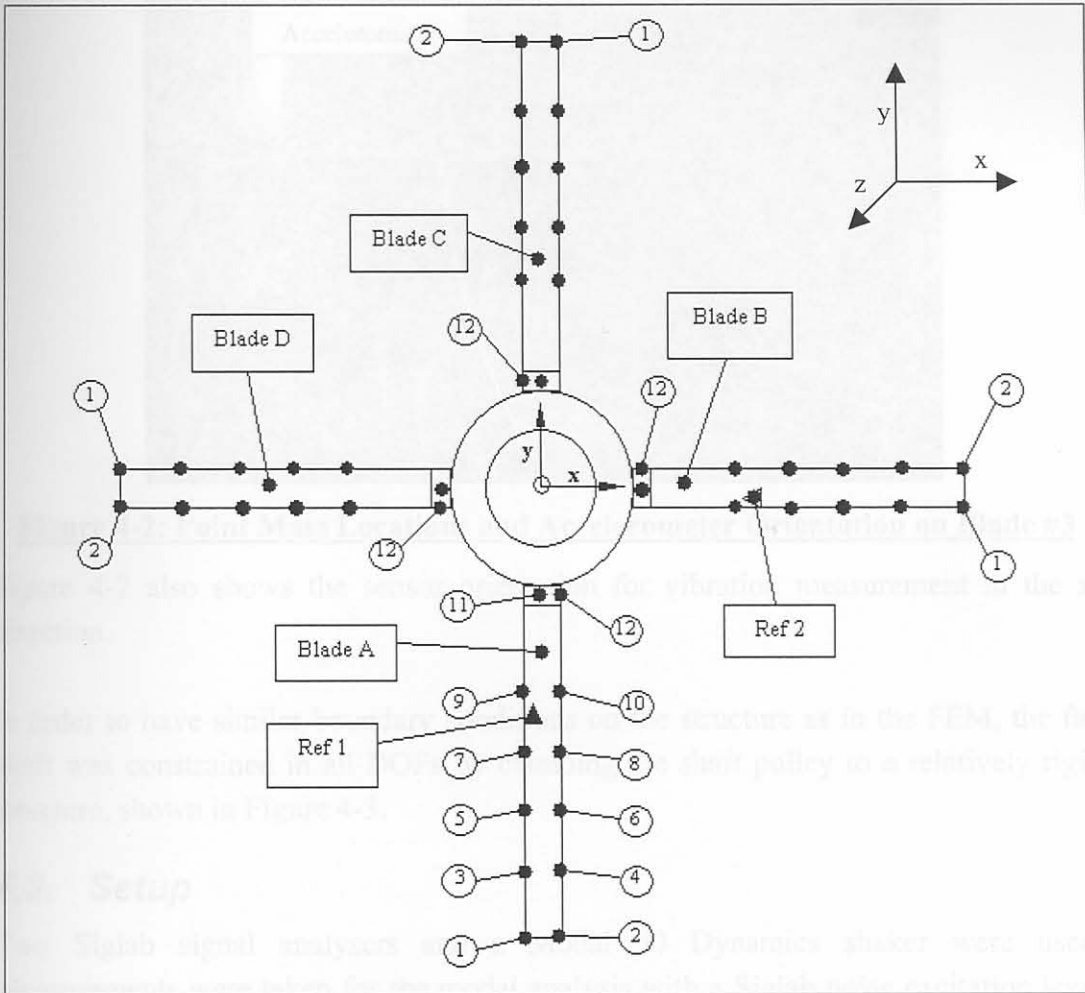
Figure 4-1: FaBCoM TeSt EMA Measurement Point Positions

Four PCB piezoelectric accelerometers were used (one for each blade) as well as an impedance head (consisting of a force transducer as well as an accelerometer) at the excitation points for transducers. The point Ref 2 was only used during the reciprocity test. Measurements were taken in the z-direction at all points except the 12th point on each blade. Also, sideways vibration measurements were taken at points 1, 3, 7, 9 and 12 of each blade. The positions of the sensors were obtained from the positions of nodes of maximum displacement at the 42nd mode shape obtained from the FEM, as this mode shape is the most complex mode shape in terms of flap wise

blade vibration within a 2000 Hz bandwidth. The position of the sensors can be found in table A-1 in Appendix A. The 10° blade angle was not taken into account.

As it was discovered in the sensitivity analysis that added point masses do have influences on some modal frequencies, it was decided to add point masses at points 1 to 10 on each blade with the same mass as that of the accelerometer used on each particular blade as shown in Figure 4-2:
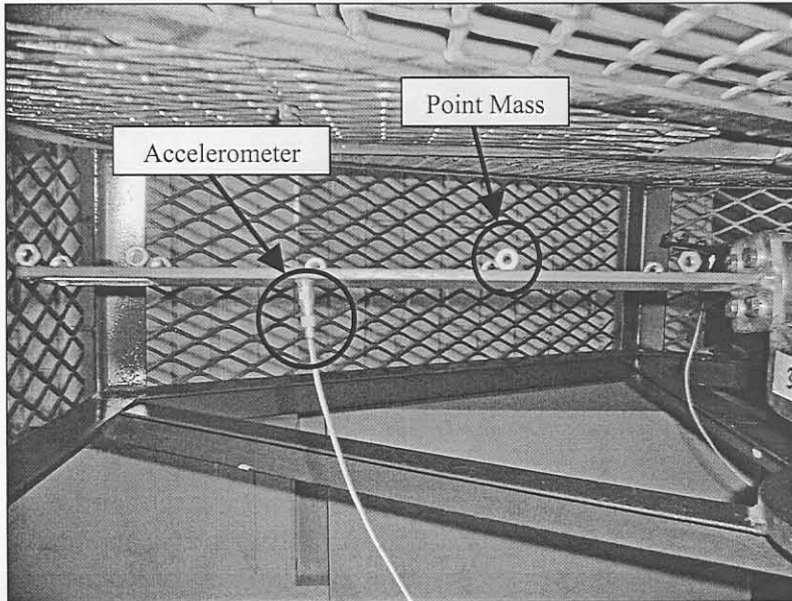
Figure 4-2: Point Mass Locations and Accelerometer Orientation on Blade #3

Figure 4-2 also shows the sensor orientation for vibration measurement in the z-direction.

In order to have similar boundary conditions on the structure as in the FEM, the fan shaft was constrained in all DOFs by clamping the shaft pulley to a relatively rigid structure, shown in Figure 4-3.

4.3. Setup

Two Siglab signal analysers and a Modal 50 Dynamics shaker were used. Measurements were taken for the modal analysis with a Siglab noise excitation level of 0.5 V RMS and an amplifier output level of 50%. Figure 4-4 shows the orientation of the Modal 50 Dynamics shaker with regards to the test structure. Figure 4-5 shows the excitation point on blade #1 with the impedance head in position as well as a sideways-orientated accelerometer. Figure 4-6 shows the overall telemetry setup with the two Siglabs and some PCB signal conditioning equipment for the accelerometers.
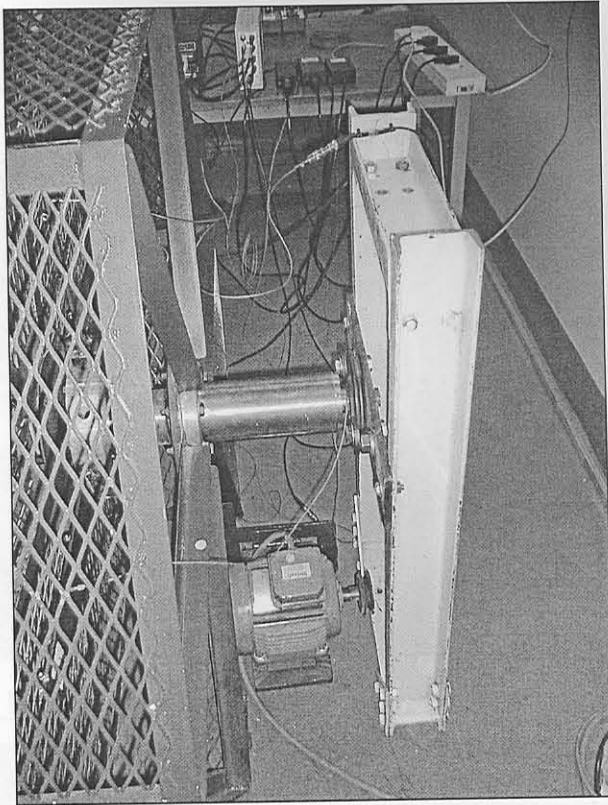
Figure 4-3: Shaft Clamping
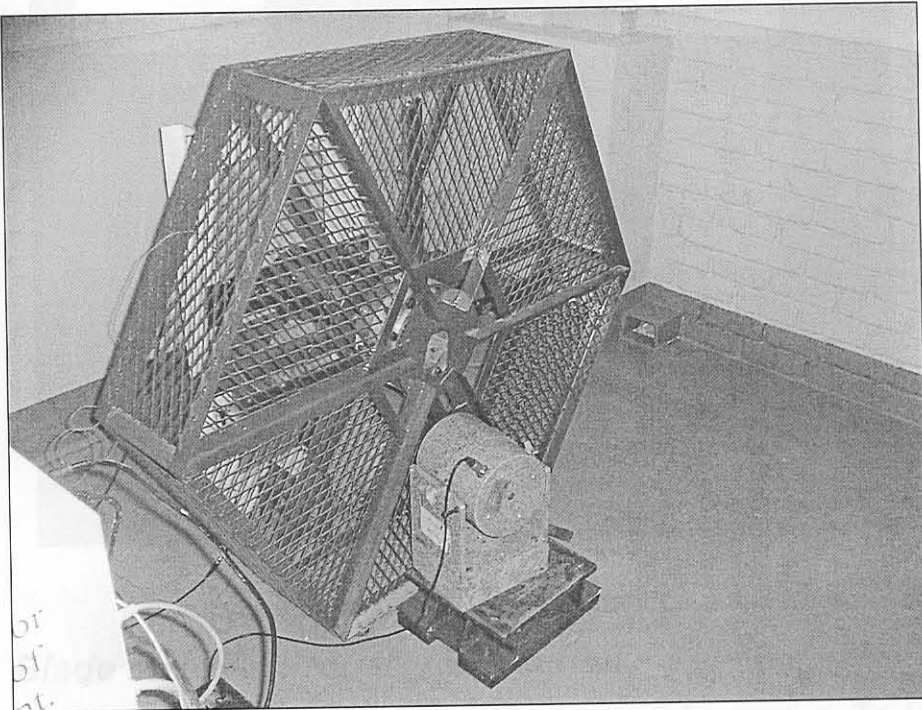
Figure 4-4: Modal 50 Shaker Orientation
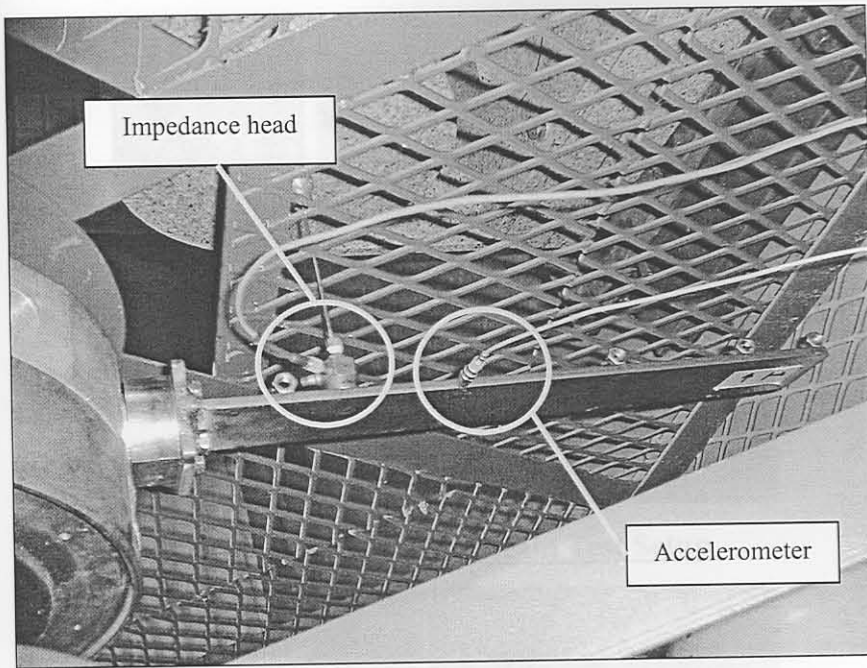
Figure 4-5: Excitation Point and Sideways-Orientated Accelerometer
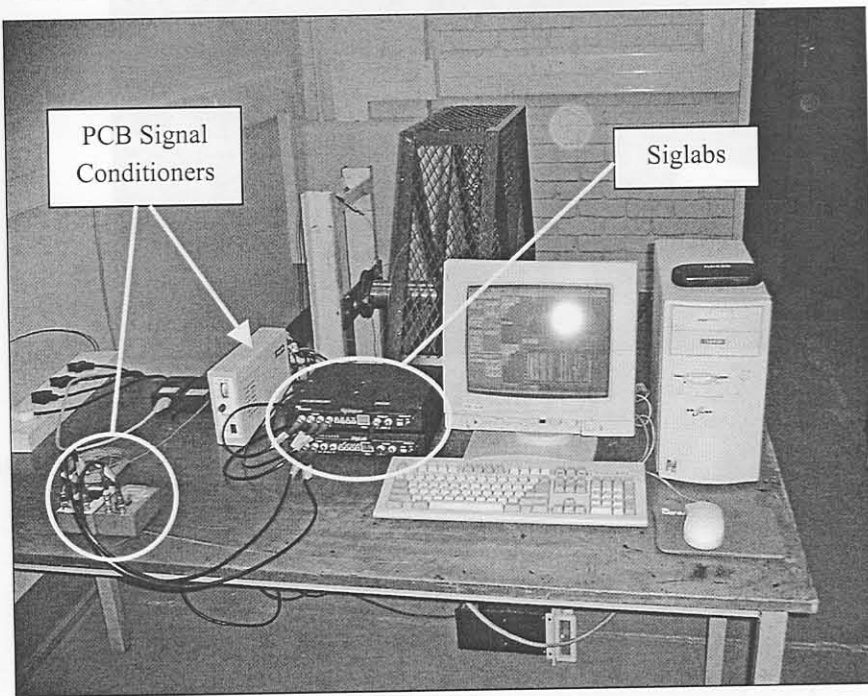
Figure 4-6: Telemetry Setup

4.4. *Blade Material Property Extraction*

The FEM results were found to be very sensitive to material properties. To determine the material properties of the steel used to manufacture the fan blades, the 1st natural frequency of a free-free beam of the same batch of steel was measured over a bandwidth of 500 Hz with excitation provided by a modal hammer. The test setup is shown in Figure 4-7 and Figure 4-8:
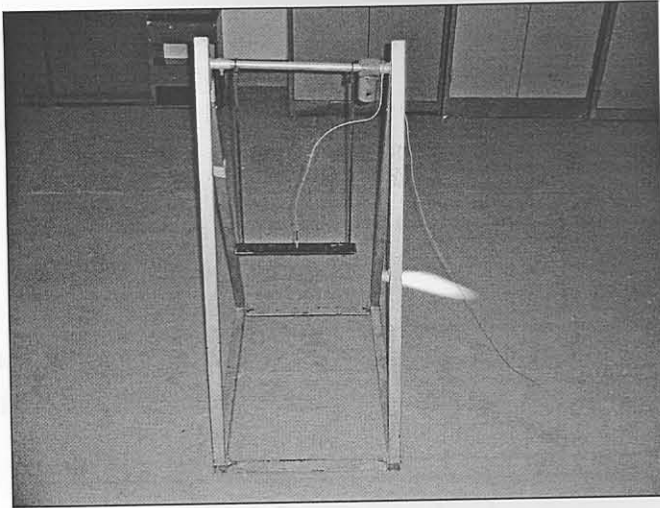
Figure 4-7: Free-free Beam Test Setup
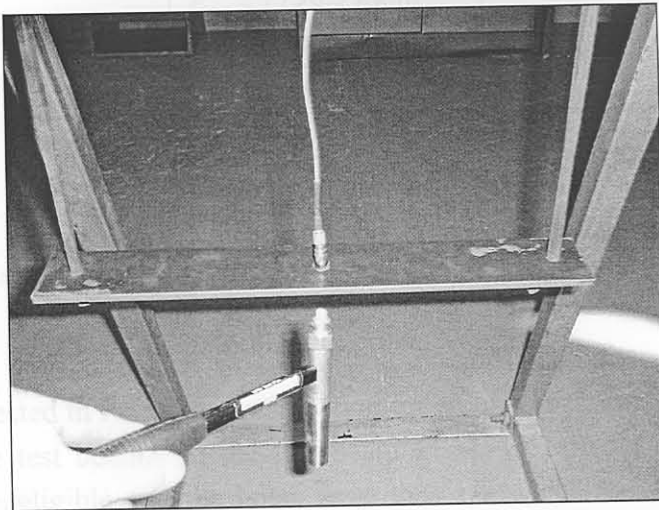
Figure 4-8: Beam Test

The measured FFT of the beam is shown in Figure 4-9:
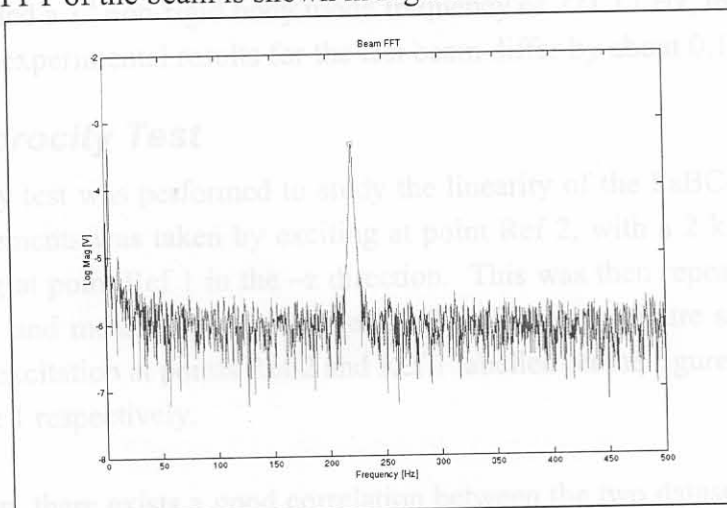
Figure 4-9: Beam FFT over 500 Hz Bandwidth

The 1st natural frequency of the test beam was found to be at 221.56 Hz. The material properties of a beam can be calculated from its 1st natural frequency using Equation (4-1) obtained from Rao [41]:

$$\omega = (\beta l)^2 \sqrt{\frac{E_y I}{\rho A l^4}}$$

(4-1)

Table 4-1 lists the values of the variables used with ω obtained from Figure 4-9 and ρ, A, l and I measured from the test specimen. $\beta l = \pi$ is given by Rao [41].

Table 4-1: Variable Values for Equation (4-1)

ω	1392.1 rad.s^{-1}
ρ	7756.3 kg.m^{-3}
A	2.5×10^{-4} m^2
l	0.34 m
I	5.208×10^{-10} m^4
βl	π

From Equation (4-1), Young's modulus for the material is calculated as

$$E_y \approx 192.6 \text{ GPa}$$

This result was tested in Patran for verification for an unconstrained beam of the exact properties of the test beam. In the test beam FEM, the effects of the holes were assumed to be negligible and the holes were thus excluded from the FEM. Figure 4-10 shows the 1st mode shape deflection of the FEM.

The FEM yielded a 1st non-rigid body mode frequency of 221.17 Hz, meaning that the numerical and experimental results for the test beam differ by about 0.18%.

4.5. Reciprocity Test

The reciprocity test was performed to study the linearity of the FaBCoM TeSt. One set of measurements was taken by exciting at point Ref 2, with a 2 kHz sine sweep, and measuring at point Ref 1 in the –z direction. This was then repeated by exciting at point Ref 1 and measuring at point Ref 2. The following figure shows the FRFs measured for excitation at points Ref 2 and Ref 1 labelled on the figure as Reference 2 and Reference 1 respectively.

As can be seen, there exists a good correlation between the two datasets up to 1 kHz. Beyond that, the correlation is not as good, but still very much acceptable.
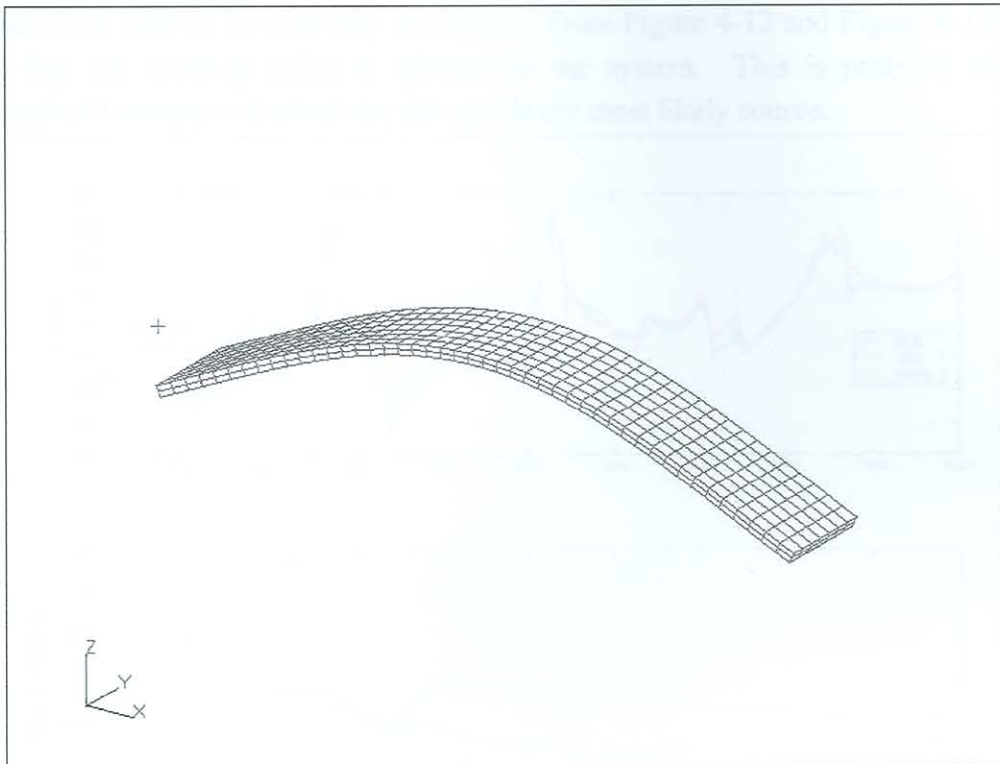
Figure 4-10: Beam Test FEM
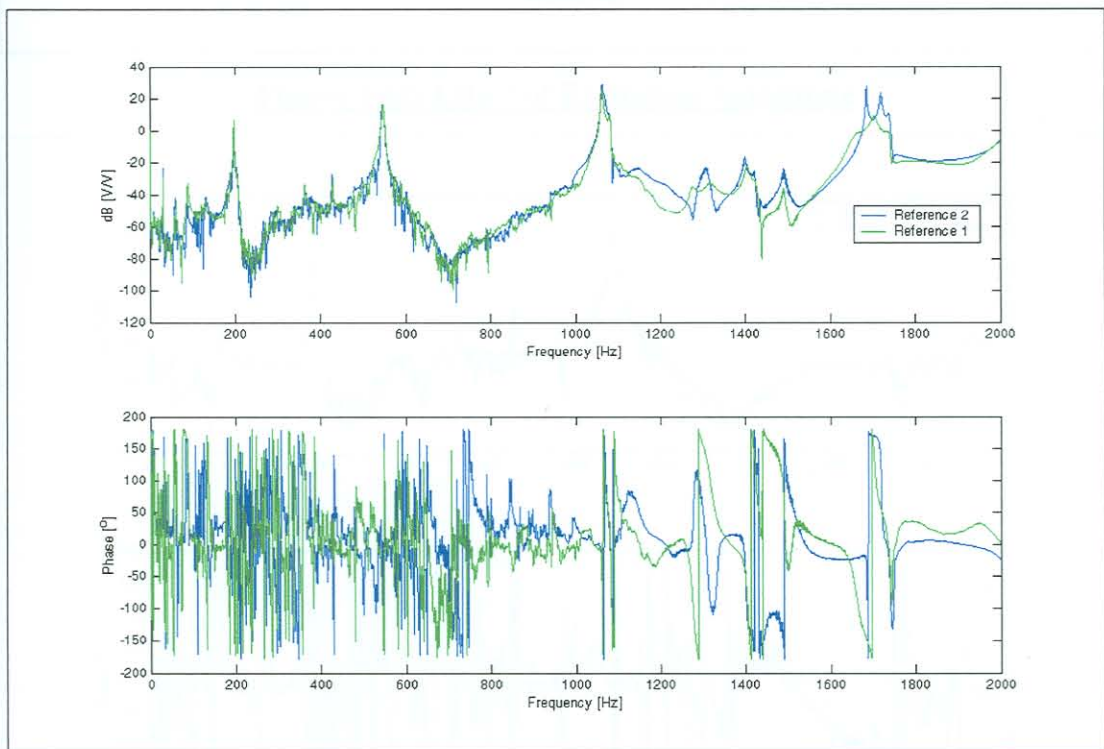
Figure 4-11: Reciprocity Test Results

4.5.1.   Noise Quantification and Qualification

From Figure 4-11, it seems that the FRFs are very noisy below 1 kHz. This was investigated by resampling the data for excitation at Ref 1 for different levels of

excitation as well as for sine step excitation. From Figure 4-12 and Figure 4-13, it is clear that the apparent noise is inherent to the system. This is probably due to mechanical looseness of which the fan grid is the most likely source.
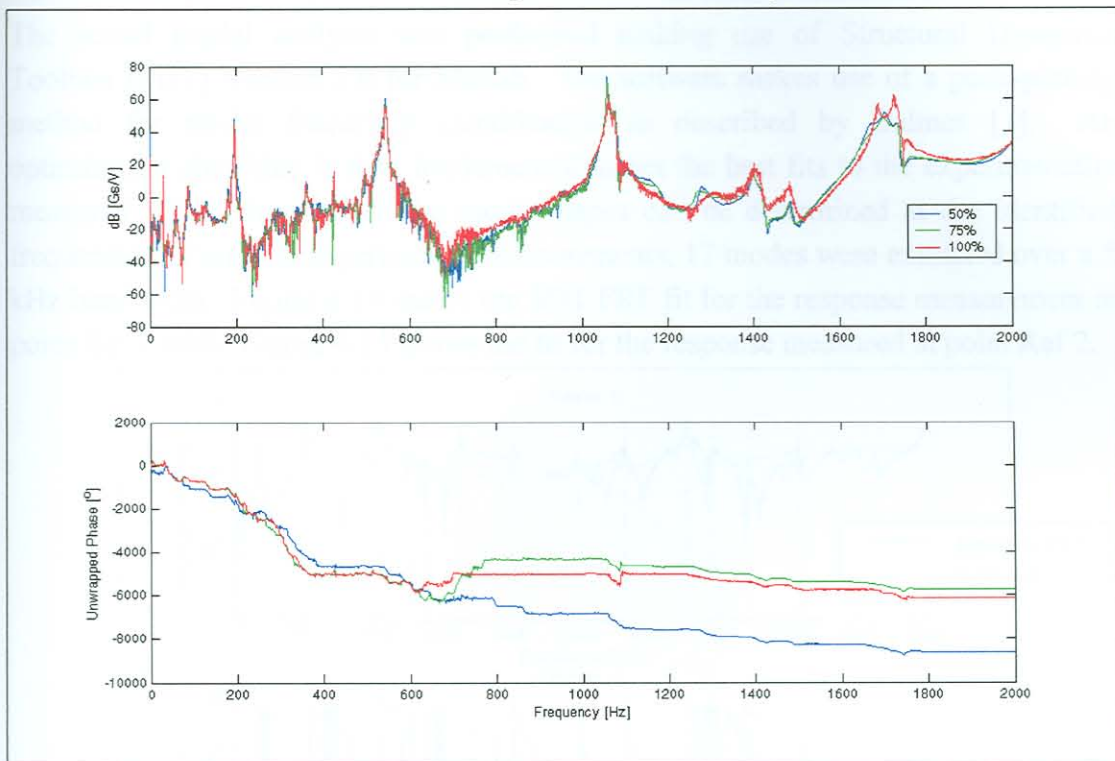
Figure 4-12: Effect of Excitation Amplitude
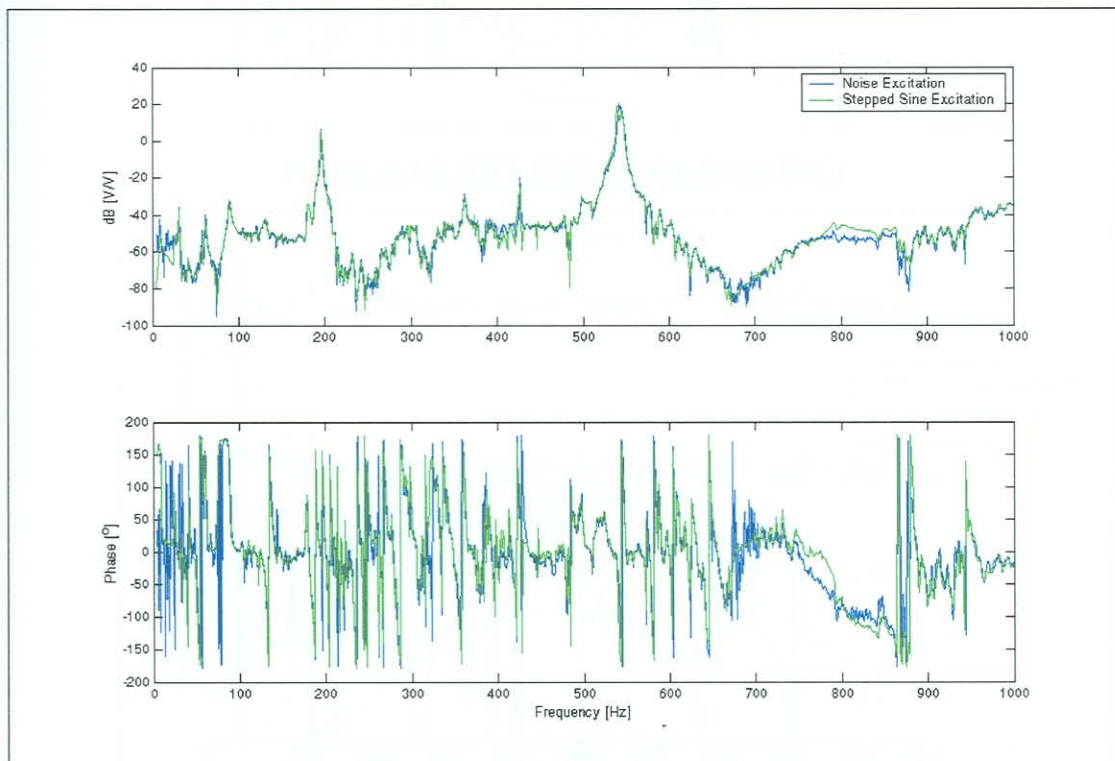
Figure 4-13: Noise and Stepped Sine Excitation Comparison

39

4.6. Modal Analysis

4.6.1. Modal Parameter Extraction

The actual modal analysis was performed making use of Structural Dynamics Toolbox (SDT) Version 3.0 for Matlab. The software makes use of a peak-picking method for modal frequency identification as described by Balmes [1]. An optimisation algorithm is then implemented to get the best fits to the experimentally measured FRFs, from which the mode shapes can be determined at the identified frequencies. From the experimental measurements, 17 modes were extracted over a 5 kHz bandwidth. Figure 4-14 shows the SDT FRF fit for the response measurement at point Ref 1 while Figure 4-15 shows the fit for the response measured at point Ref 2.
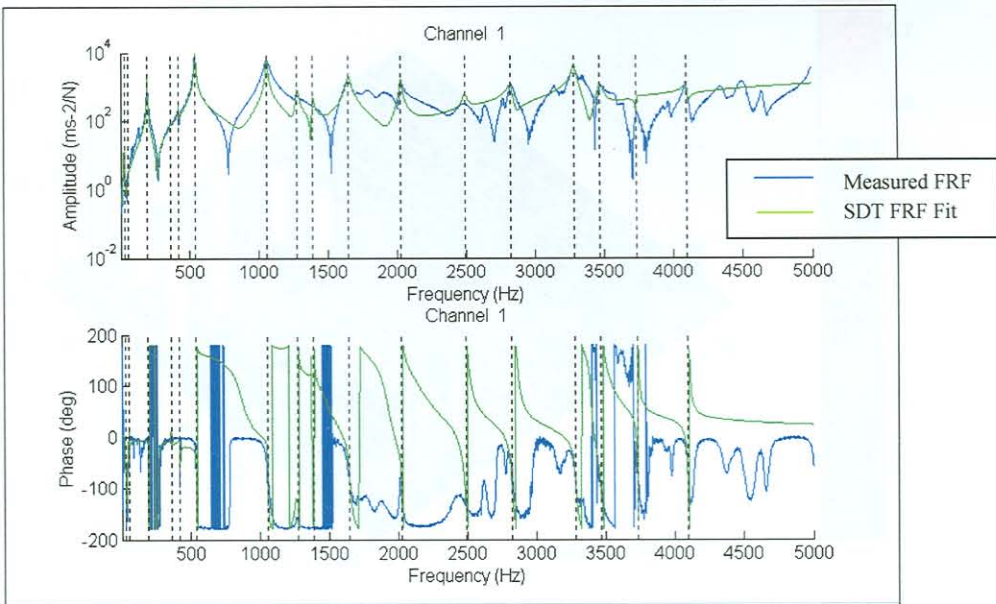
Figure 4-14: SDT FRF Fit for Point Ref 1
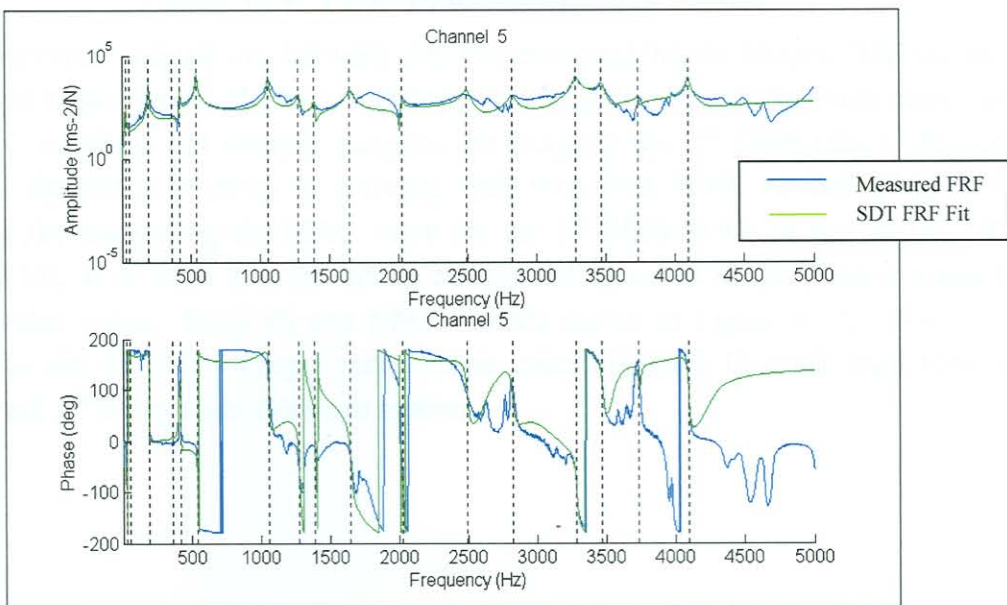
Figure 4-15: SDT FRF Fit for Point 2 on Blade #1, Sideways

4.6.2.   MAC Matrix Calculations

Figure 4-16 shows the results for the MAC matrix in a three dimensional format. A definite diagonal can be seen on the MAC matrices. Few of the values however, are very good. Possible reasons include that only one shaker was used in the test that may have resulted in insufficient amounts of energy supplied throughout the system for well defined responses.
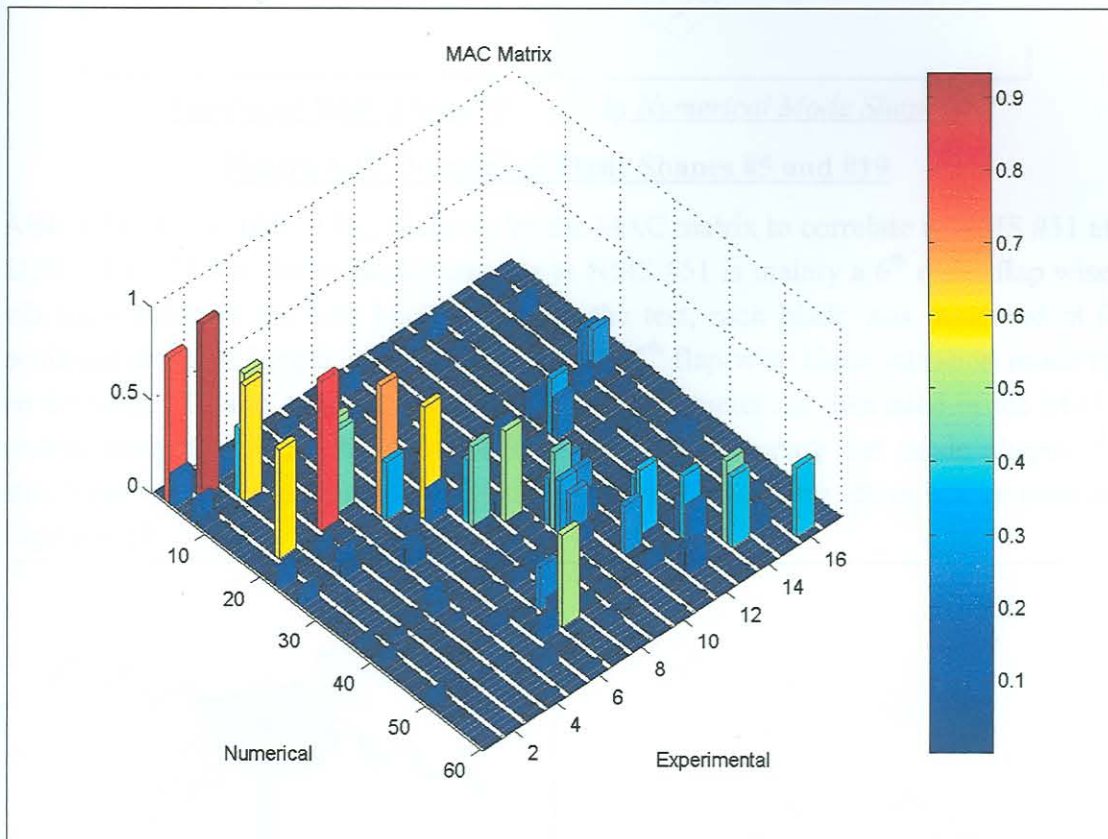
Figure 4-16: Three Dimensional MAC Matrix

From graphical comparison between the Experimental Mode Shapes (EMSs) and Numerical Mode Shapes (NMSs) with MAC values greater than 0.3, it was clear that the MAC matrix is not entirely accurate, for example the 2nd EMS (the 1st torsion mode of the shaft) is given to correlate well with both NMS #5 and NMS #19. However, by comparing the MAC value for the 5th NMS (0.93) to that of the 19th NMS (0.58), it is clear that the actual corresponding mode shape yielded a much higher MAC value. NMS #5 and NMS #19 are shown in Figure 4-17. The same occurs for the 4th EMS being a mode shape consisting of a 1st order shaft torsion motion and 2nd order blade sideways motion.

a) *Numerical Mode Shape #5*   b) *Numerical Mode Shape #19*
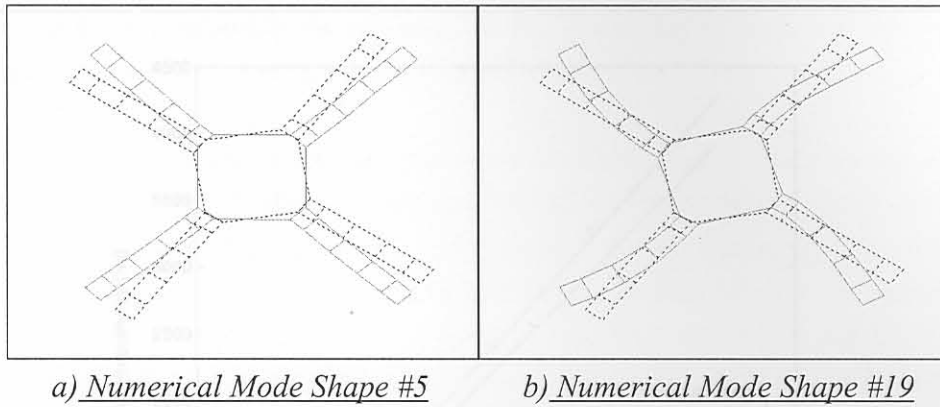
Figure 4-17: Numerical Mode Shapes #5 and #19

Also, EMS #7, at 1058.9 Hz, is shown by the MAC matrix to correlate to NMS #51 at 2630.6 Hz. This is due to modal aliasing as NMS #51 is mainly a 6th order flap wise vibration mode of the four blades. During the test, each blade was measured at 6 positions along its length, allowing for only the 5th flap-wise blade vibration mode to be detected. This in effect is the same case for the numerical data used in the MAC matrix computation, as the software used can only compare the mode shapes of structures with an equal number of nodes. The modal aliasing effect can be seen in Figure 4-18.

a) *Actual Numerical Mode Shape*   b) *Aliased Numerical Mode Shape*
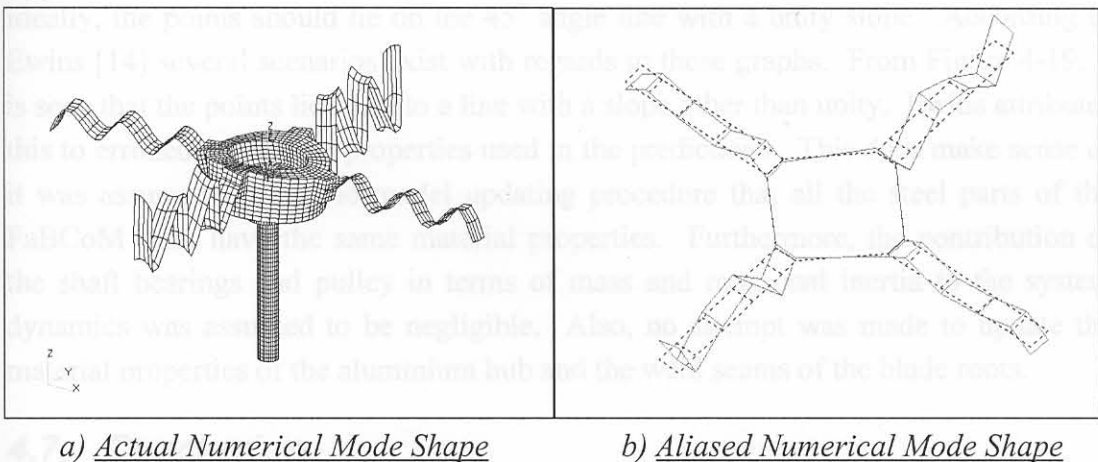
Figure 4-18: Modal Aliasing of Numerical Mode Shape #51

When these discrepant mode shapes are ignored when a scatter plot of the numerical and experimental frequencies is drawn, Figure 4-19 is obtained. Equation (4-2) gives the function of the linear fit calculated using Excel and Matlab:

$$f_{exp} = 1.1034 f_{num} - 55.166$$

(4-2)

with R^2 = 0. 9902.
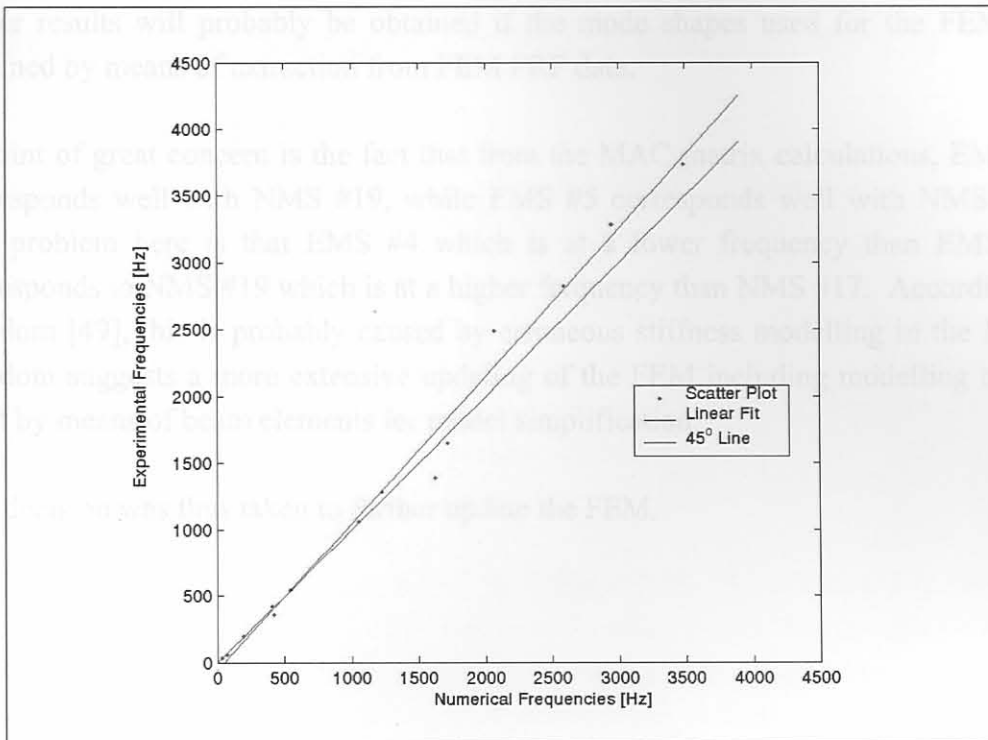
Figure 4-19: Comparison of Experimental and Numerical Natural Frequencies

Ideally, the points should lie on the 45° angle line with a unity slope. According to Ewins [14] several scenarios exist with regards to these graphs. From Figure 4-19, it is seen that the points lie close to a line with a slope other than unity. Ewins attributes this to erroneous material properties used in the predictions. This does make sense as it was assumed during the model updating procedure that all the steel parts of the FaBCoM TeSt have the same material properties. Furthermore, the contribution of the shaft bearings and pulley in terms of mass and rotational inertia to the system dynamics was assumed to be negligible. Also, no attempt was made to update the material properties of the aluminium hub and the weld seams of the blade roots.

4.7. Conclusion

Although not extremely good values were obtained from the MAC matrix, a well-defined diagonal does exist. This means that the FEM does correspond sufficiently to the FaBCoM TeSt in terms of mode shapes. One reason for the poor overall MAC values may be the assumptions used in the FEM as described in Section 2.7. To obtain better results, a more intensive model updating procedure of the FEM is necessary.

Another likely reason for the low MAC values is the effect of modal density as up to four mode shapes of the FEM were found at around the same frequency as described in Section 3.5. During calculation of the MAC matrix, each EMS is compared to each NMS. This presents a problem, as closely spaced mode shapes around some frequency will appear as a single hybrid mode shape in the experimental structure.

43

Better results will probably be obtained if the mode shapes used for the FEM are obtained by means of extraction from FEM FRF data.

A point of great concern is the fact that from the MAC matrix calculations, EMS #4 corresponds well with NMS #19, while EMS #5 corresponds well with NMS #17. The problem here is that EMS #4 which is at a lower frequency than EMS #5, corresponds to NMS #19 which is at a higher frequency than NMS #17. According to Strydom [49], this is probably caused by erroneous stiffness modelling in the FEM. Strydom suggests a more extensive updating of the FEM including modelling of the shaft by means of beam elements for model simplification.

The decision was thus taken to further update the FEM.

Chapter 5   Updating of the Finite Element Model

5.1. FEM Updating

In the process of updating the FEM, a number of issues were addressed:

5.1.1.   Structural Damping

It was decided to incorporate structural damping in the FEM in order to obtain more realistic FRFs from it. This is also suggested by Strydom [49]. The structural damping of all the materials in the FEM was assumed to be 1%, using Fredö et al. [18] as a guideline for weld seams and solid connections.

5.1.2.   Frequency Tuning

The first torsional modal frequency of the FEM (NMS #5) was tuned to the first torsional EMS frequency (EMS #2). This was decided upon in the aim of correlating the frequencies of NMS #19 to EMS #4 (the second shaft-related torsional mode shapes) as these mode shapes prove to be very important in terms of damage detection as described by Maynard and Threthewey [35] and noted in Section 3.4.

In order to do this, it was decided to revisit the design of the FEM. The solid element modelled shaft was replaced with a beam element modelled shaft. The reason for this is that it is much easier to adjust the diameter of the modelled shaft when beam elements are used as opposed to solid elements. This also serves to simplify the model ([49]). The beam element modelled shaft was connected to the rest of the FEM by means of an RBE2-type MPC as shown in Figure 5-1. The same nodal constraints were applied here as on the shaft of the previous FEM.

By performing modal analyses on the FEM for arbitrarily chosen shaft radii, a graph was drawn up relating the frequencies of NMS #5 to the different shaft radii as shown in Figure 5-2. A shaft radius that will yield the desired frequency was calculated as 21.08 mm. By updating the FEM accordingly, NMS #5 was changed from 68.3 Hz in the initial FEM to 57.28 Hz, corresponding very well with the 57.24 Hz frequency of EMS #2.

The frequency of the NMS corresponding with EMS #4 shifted from 416.96 Hz to 393.97 Hz, moving closer to the frequency of EMS #4 which is 361.07 Hz. This improved the frequency error from 15.5% to 6.4%.
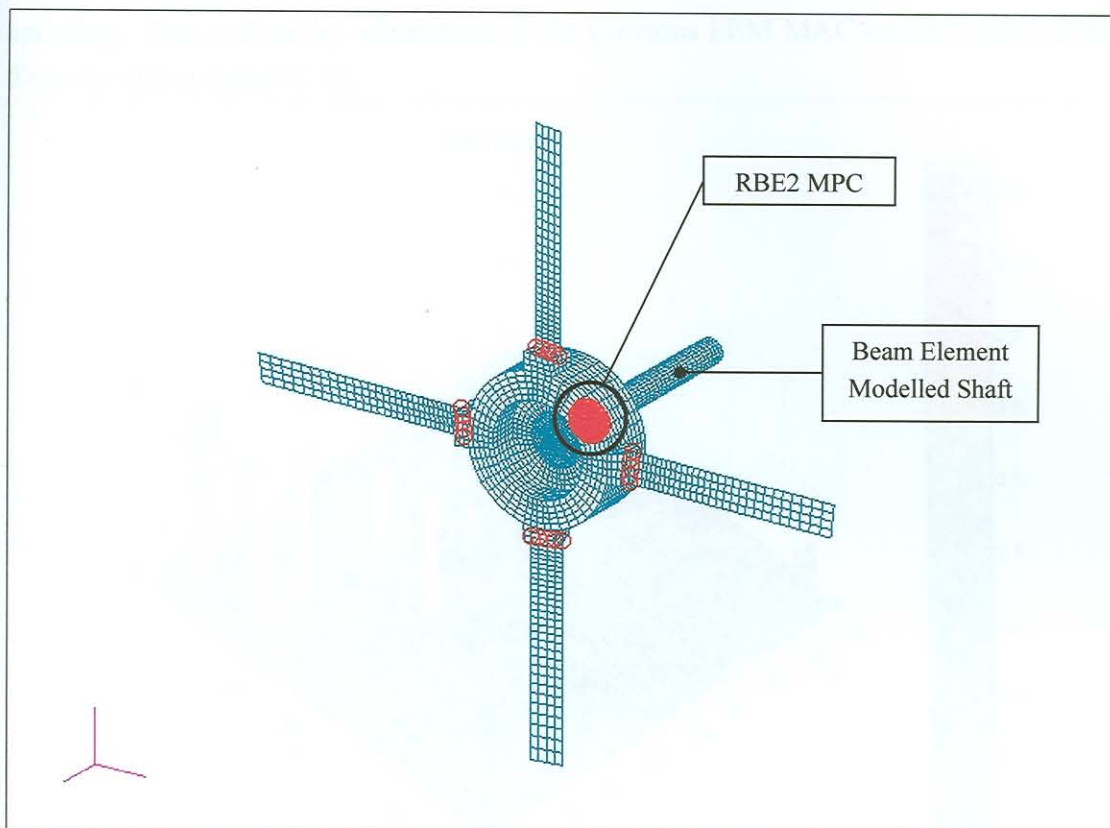
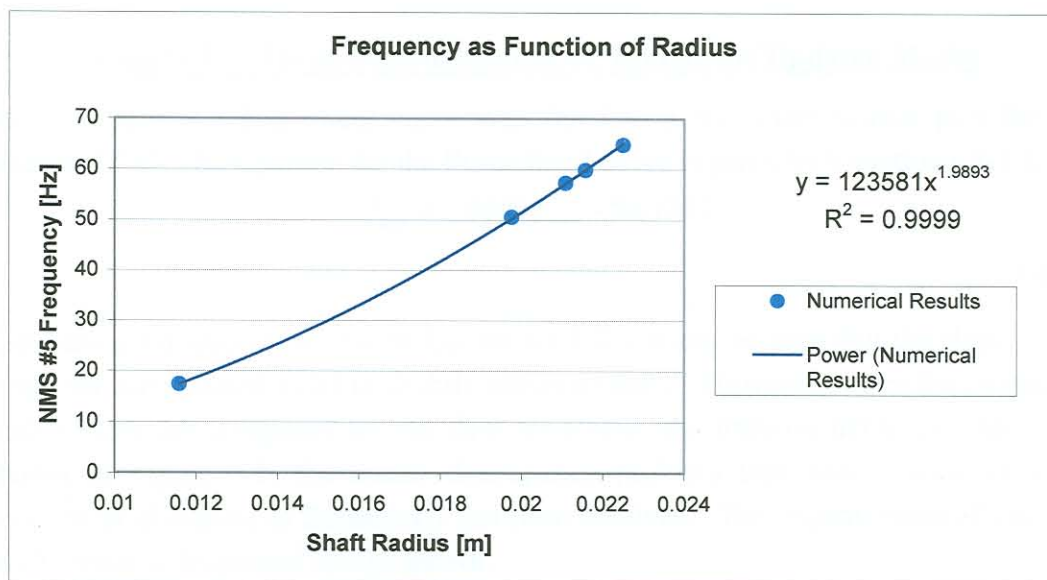**Figure 5-1: Updated Finite Element Model**

Figure 5-2: Shaft Radius Effect on First Shaft Torsional Frequency

5.2. *MAC Matrix Calculations for Updated FEM*

Again, a MAC matrix was calculated for the updated FEM as shown in Figure 5-3. Compared to Figure 4-16, the MAC matrix for the updated FEM is less "noisy" and also has a bit better defined diagonal. Also, the MAC matrix values for the updated and previous FEMs are compared in Figure 5-4, showing the effects of the model

updating. This is done by subtraction of the previous FEM MAC matrix values from those for the updated FEM.
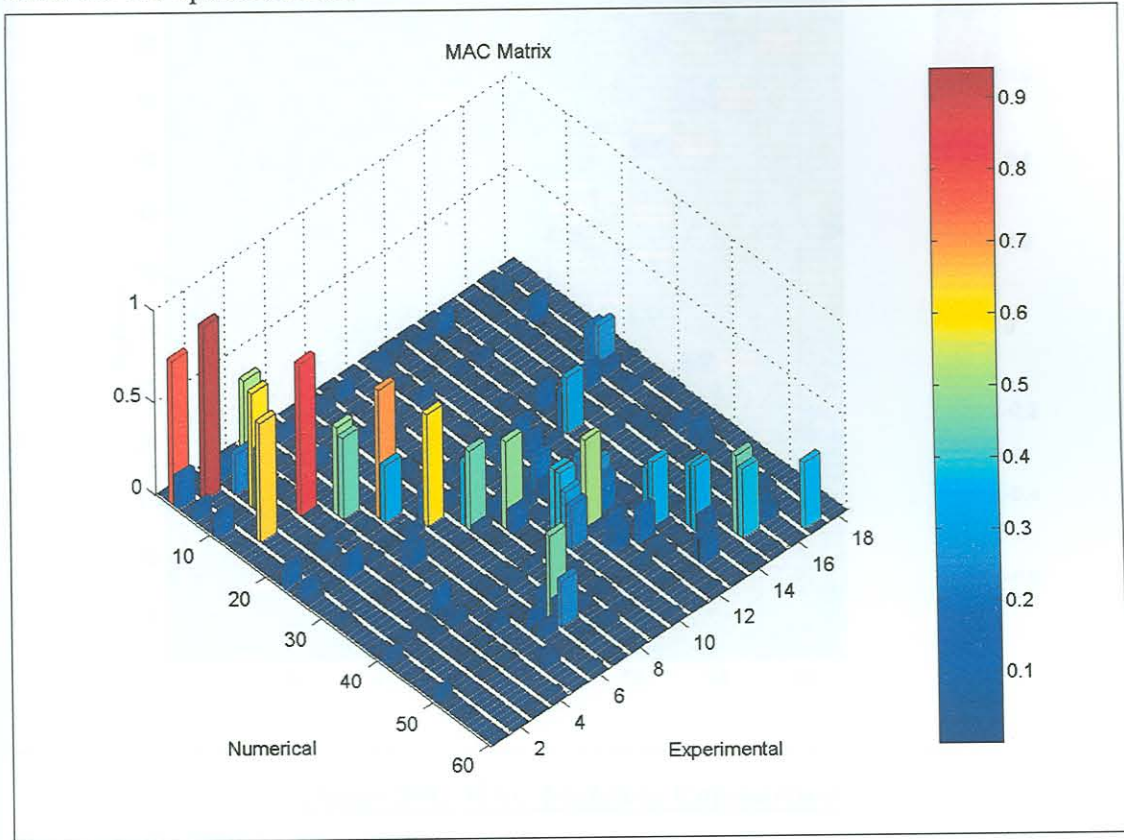
Figure 5-3: Three-Dimensional MAC Matrix for Updated Model

As in Section 4.6.2, a linear curve was fitted to a frequency scatter plot for the updated FEM. The equation for the linear fitted curve is given by Equation (5-1):

$$f_{exp} = 1.0859 f_{num} - 54.1252$$

$$(5-1)$$

Comparing Equation (5-1) with Equation (4-2), it can be seen that the slope of the graph for the updated FEM is slightly closer to unity. However, when the frequency scatter plots are compared for the first six EMSs, the improvements are clear. As shown in Figure 5-5, the modal discrepancy problem that was a cause of great concern as discussed in Section 4.7 has been resolved. The improvement of the first shaft torsional frequency is also shown.

An additional mode shape was identified at about 1800 Hz and was previously not used. This mode shape will be referred to as EMS #X. From MAC calculations it corresponds well to NMS #41 (MAC=0.5011) and NMS #42 (MAC=0.375). EMS #X and NMS #41 are graphically depicted in Figure 5-6.
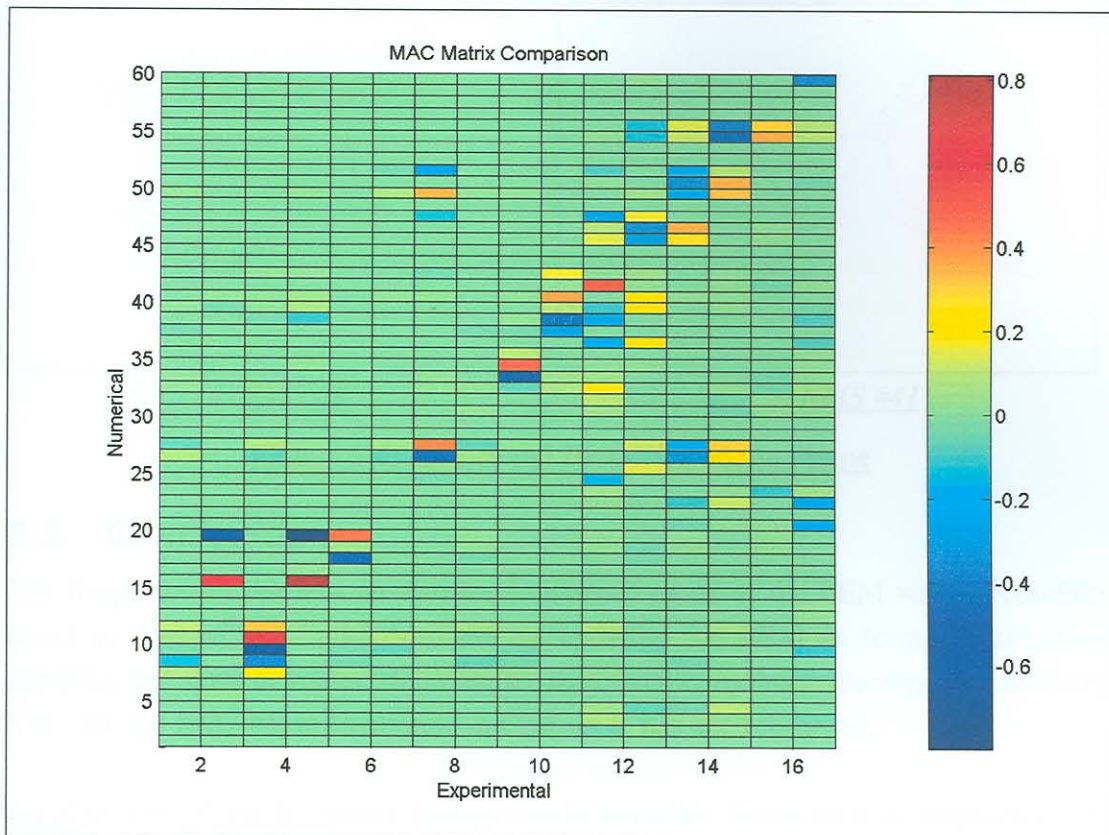
Figure 5-4: MAC Matrices Comparison
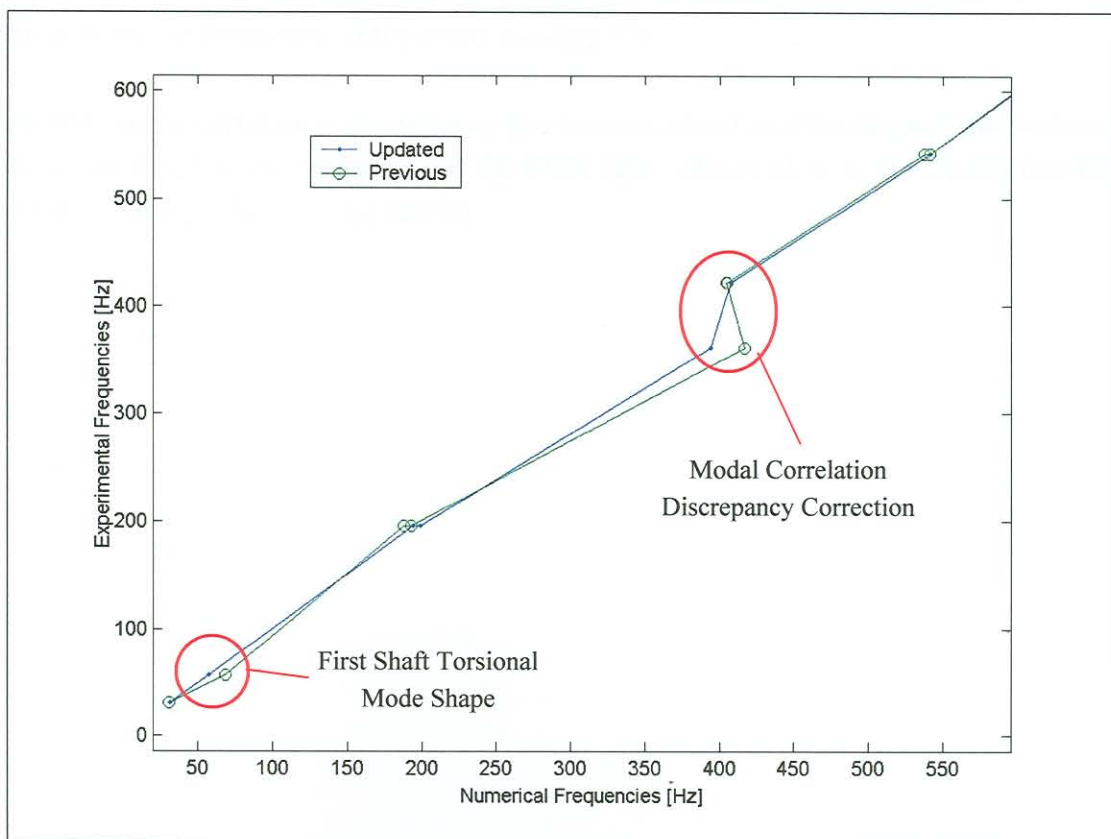
Figure 5-5: Frequency Scatter Comparison
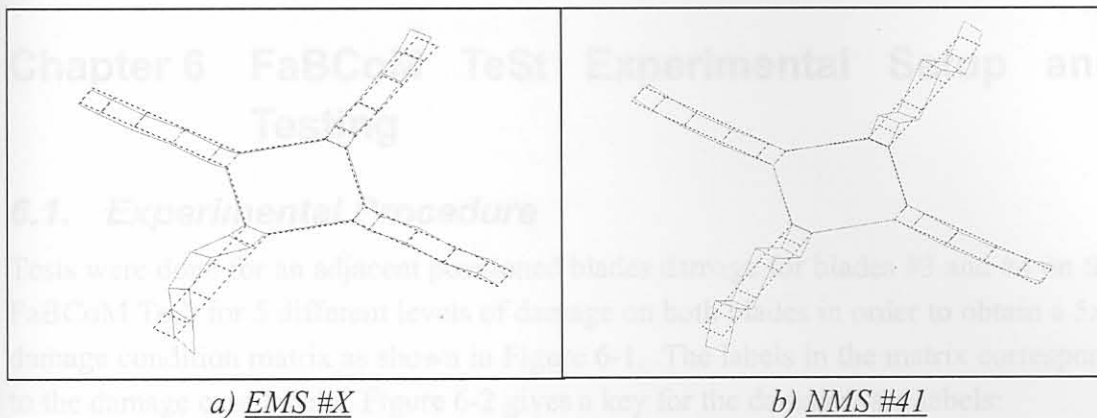

a) EMS #X   *b) NMS #41*

Figure 5-6: Additional Identified Mode Shape

5.3. Conclusion

The frequency of the first shaft-related torsional mode of the FEM was successfully tuned to that of the FaBCoM TeSt by updating the FEM in terms of structural damping and shaft diameter. In doing so, the modal correlation discrepancy involving EMS #4 and EMS #5 as mentioned in Chapter 4, has been resolved.

Another aim of the frequency tuning was to correlate the numerical frequency with the experimental frequency of the second shaft-related torsional mode shape. The frequency error of the NMS was more than halved, although still being about 33 Hz away from the frequency of the corresponding EMS.

As the modal correlation discrepancy has been resolved and the second shaft-related torsional mode shape frequency of the FEM been improved, it is concluded that the FEM updating effort was successful.

Chapter 6 FaBCoM TeSt Experimental Setup and Testing

6.1. Experimental Procedure

Tests were done for an adjacent positioned blades damage for blades #3 and #4 on the FaBCoM TeSt for 5 different levels of damage on both blades in order to obtain a 5x5 damage condition matrix as shown in Figure 6-1. The labels in the matrix correspond to the damage case labels. Figure 6-2 gives a key for the damage case labels:

	50%	4e2	4e3	4e4	4e5	4e6
Blade #3 Damage Level	37.5%	4d2	4d3	4d4	4d5	4d6
	25%	4c2	4c3	4c4	4c5	4c6
	12.5%	4b2	4b3	4b4	4b5	4b6
	0%	4a2	4a3	4a4	4a5	4a6
		0%	12.5%	25%	37.5%	50%

Blade #4 Damage Level

Figure 6-1: Adjacent Positioned Blades Damage Case Matrix

4a 2

Blade #4 Number [#]   Blade #3 Number [#]
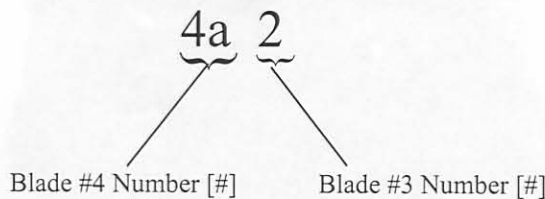
Figure 6-2: Damage Case Label Key

The test procedure will involve measuring for the undamaged case. After that, a certain blade will be damaged at a certain level after which measurements will be taken. This will be repeated until that blade has been damaged to a pre-determined extent. Then that blade will be replaced with an undamaged blade after which an adjacent blade's damaged will be incremented. This whole procedure will be repeated until both blades have reached the pre-determined damage level. Figure 6-3 gives a flow chart for the test procedure.
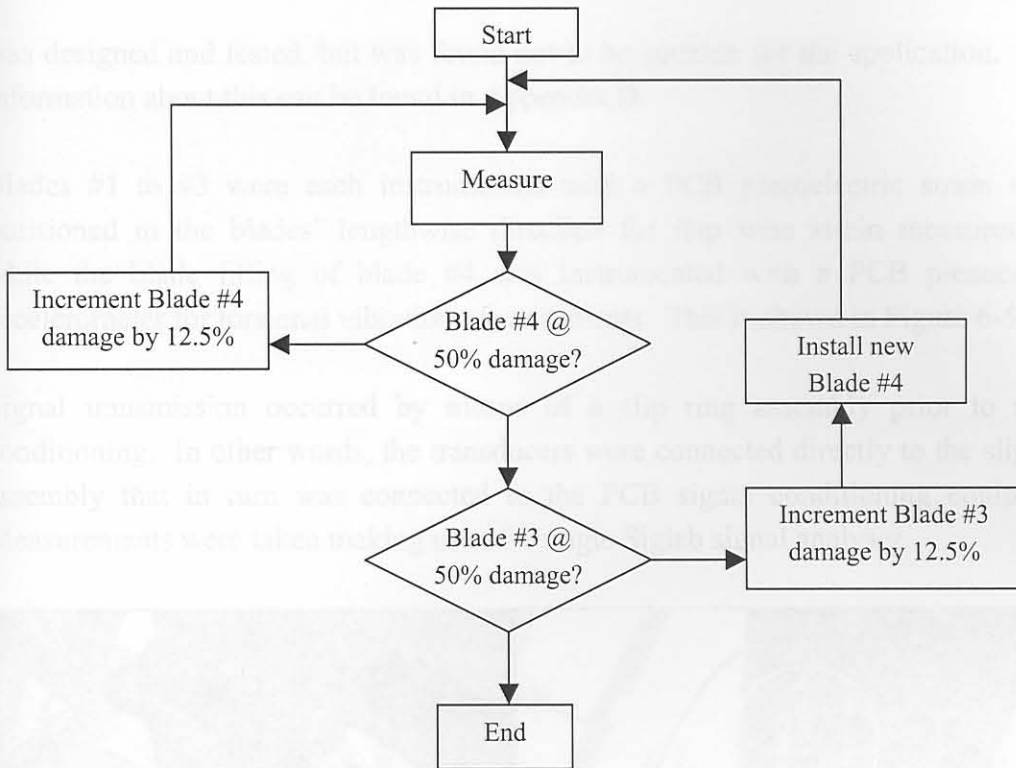
Figure 6-3: Test Procedure Flow Chart

Damage will be simulated in the FaBCoM TeSt by means of hack saw cuts into the blade roots as shown in Figure 6-4. This is the same procedure used by Smit [45].
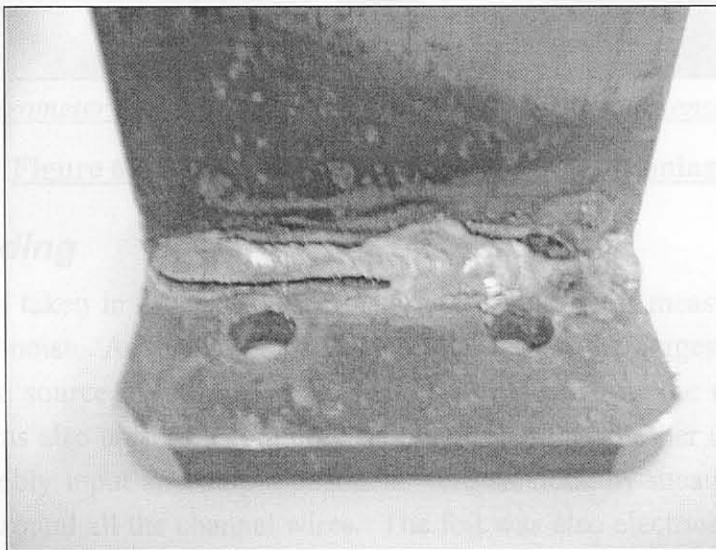

**Figure 6-4: Experimental Blade Damage Simulation**

6.2. *Telemetry*

Initially, it was decided to make use of normal strain gauge rosettes as transducers as they are commonly used in industry. However, no equipment was available for bridge excitation and amplification of the strain gauges for the 2000 Hz measurement bandwidth of interest. For this reason, a 4-channel strain gauge half bridge amplifier

was designed and tested, but was found not to be suitable for the application. More information about this can be found in Appendix D.

Blades #1 to #3 were each instrumented with a PCB piezoelectric strain sensor positioned in the blades' lengthwise direction for flap wise strain measurements, while the blade fitting of blade #4 was instrumented with a PCB piezoelectric accelerometer for torsional vibration measurements. This is shown in Figure 6-5.

Signal transmission occurred by means of a slip ring assembly prior to signal conditioning. In other words, the transducers were connected directly to the slip ring assembly that in turn was connected to the PCB signal conditioning equipment. Measurements were taken making use of a single Siglab signal analyser.
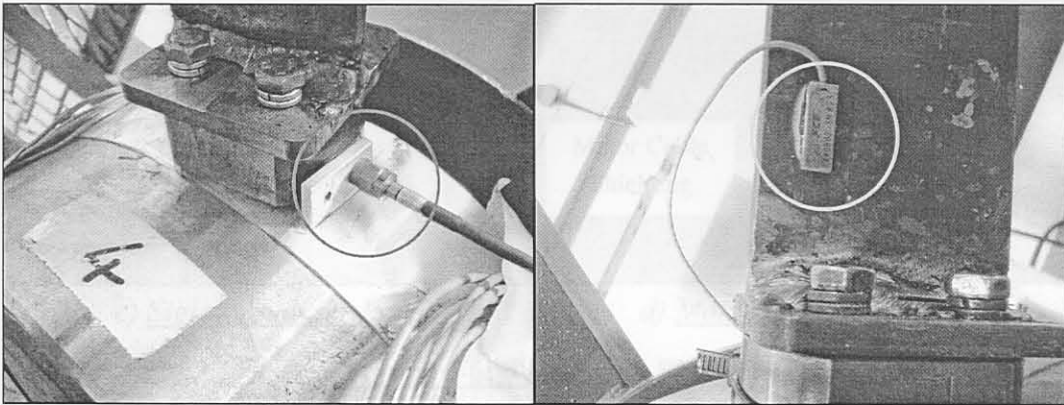
a) *Accelerometer Orientation*   b) *Piezoelectric Strain sensor Orientation*

Figure 6-5: Transducer Orientation and Positioning

6.3. Shielding

Great care was taken in order to obtain maximum shielding of measurement signals from electrical noise. As the motor speed controller was of the biggest concern for an electrical noise source, a hollow metal shield was placed over the controller. The metal shield was also used as a common shielding earth for all other equipment. The slip ring assembly input and output channels were shielded by means of aluminium foil wrapped around all the channel wires. The foil was also electrically isolated and connected to the common shielding earth together with the Siglab analyser, FaBCoM TeSt frame and motor cable shield as shown in Figure 6-6. Figure 6-7 shows the effect of shielding. It is clear from this figure that the noise to signal ratio is significantly reduced.

6.4. Measurements

As already discussed in section 6.2, simultaneous recording was done of strain signals on blades #1, #2 and #3 as well as the torsional acceleration signal from the fitting of
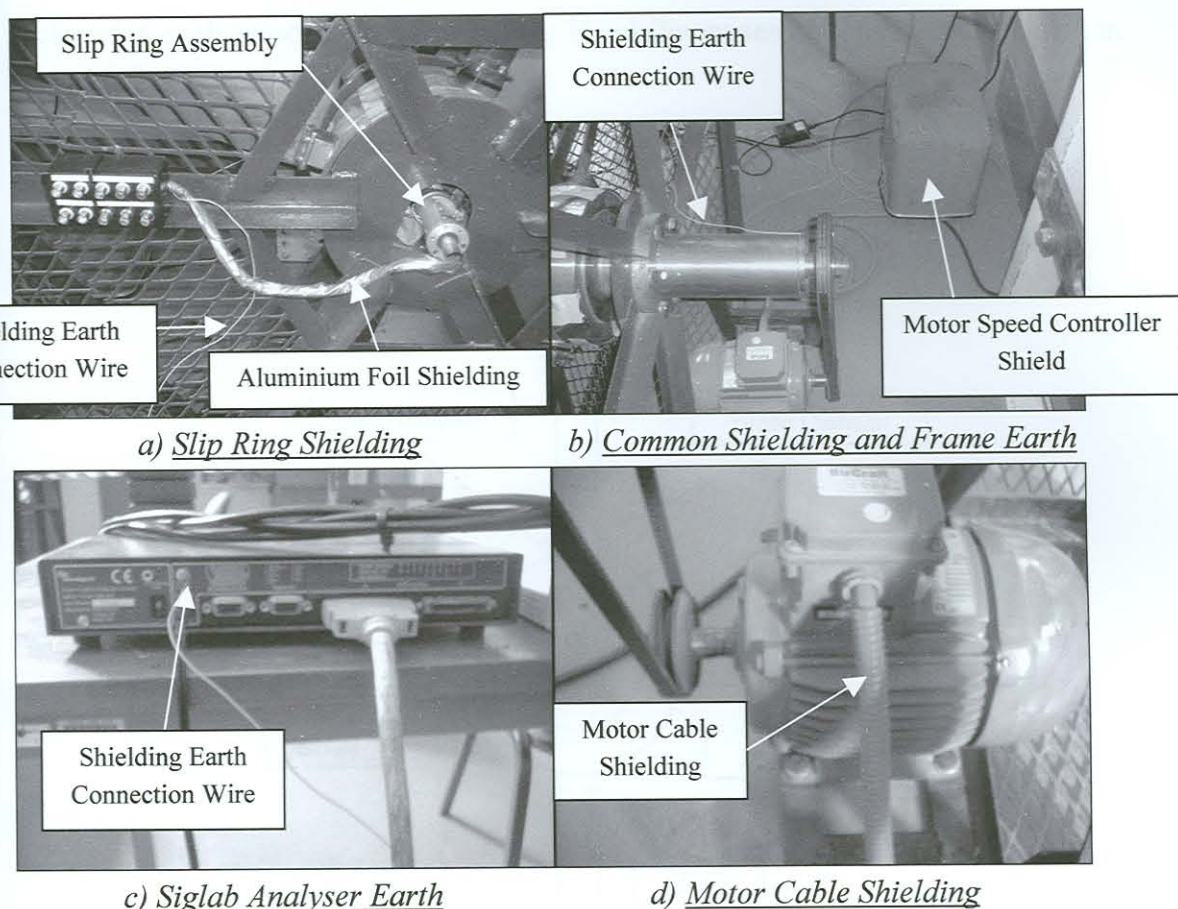
a) *Slip Ring Shielding*   b) *Common Shielding and Frame Earth*

c) *Siglab Analyser Earth*   d) *Motor Cable Shielding*
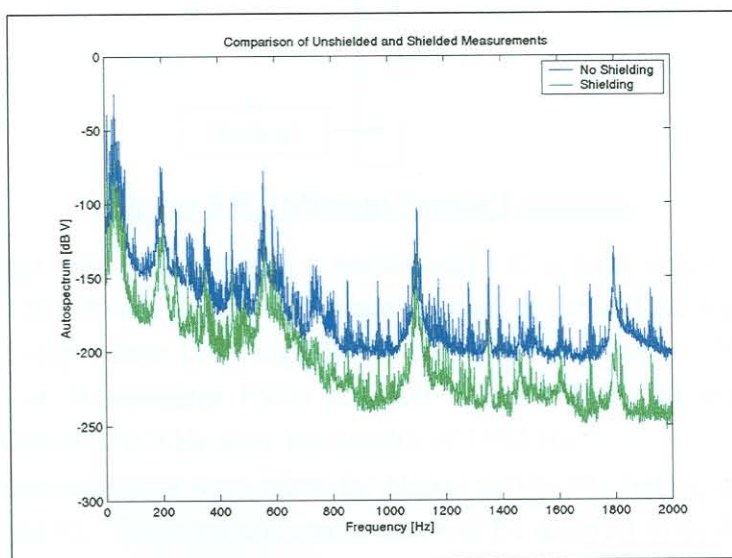
Figure 6-6: Test Setup Shielding

Figure 6-7: Comparison of Unshielded and Shielded Measurements

blade #4. This was done in order to simulate three different strain sensor location scenarios with regard to damage location namely Sensor Location (SL) #1, SL #2 and SL #3, where the sensor location number refers to the blade number on which the strain sensor is installed for that particular sensor location. The accelerometer is

53

included in each sensor location scenario. The different sensor locations are shown in Figure 6-8.
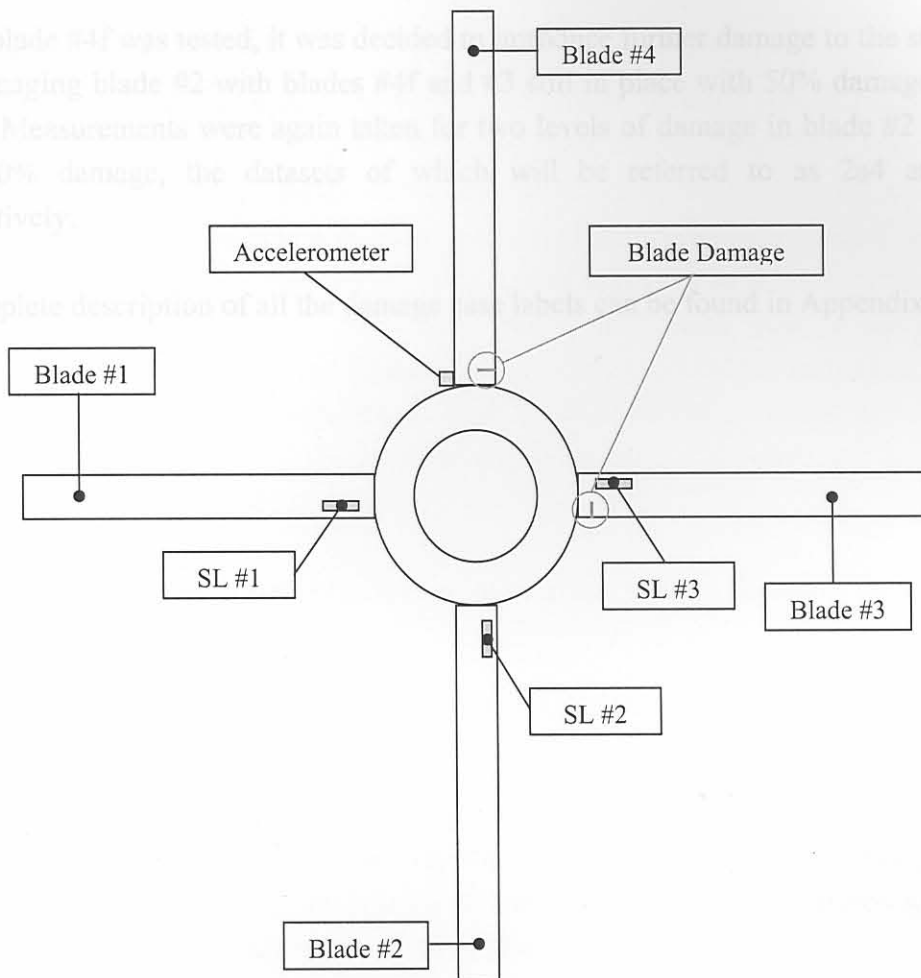
Figure 6-8: Different Sensor Locations

For each damage case (Figure 6-1), a continuous 192 s time sample at a sampling frequency of 5120 Hz was recorded for each channel of data. This was done in order to obtain 24 independent time signals with lengths 8 s each.   This allows the calculation of 24 independent PSDs for each channel from 20 averages using a frequency resolution of 2.5 Hz for a bandwidth of 2560 Hz.

Additionally, measurements were taken for blades #4b to #4e before any damage was inflicted on blade #3. These measurement sets will be referred to as 4b1 to 4e1. The reason why these measurements were taken was to see whether the methodology that will be developed is robust in terms of blade manufacturing and installation variables such as weld seam quality and blade attack angle. These two variables will differ from blade to blade due to manufacturing tolerances.

Also, it was discovered that the strain sensor on blade #2 came loose during testing of blade #4e. The sensor was installed at the same position on blade #2 again, after

which the same tests that were performed on blade #4e, were performed on an additional blade named blade #4f. The dataset labels for blade #4f ranges from 4f2 to 4f6.

After blade #4f was tested, it was decided to introduce further damage to the structure by damaging blade #2 with blades #4f and #3 still in place with 50% damage levels each. Measurements were again taken for two levels of damage in blade #2 at 25% and 50% damage, the datasets of which will be referred to as 2a4 and 2a6 respectively.

A complete description of all the damage case labels can be found in Appendix E.

Chapter 7 Neural Network Implementation with Experimental Supervision

7.1. Purpose

The reason for using neural networks for blade damage quantification and qualification is the complex nature of the problem faced. Smit [45] was able to identify damage on a single blade with sensors installed on the blade itself, using only the frequency shifts of a single frequency obtained from ARMAX models identified from the measured data. The aim of using neural networks in this dissertation is to train and test neural networks to quantify and qualify blade damage for multiple blades without the sensors being installed on the damaged blades themselves. In this chapter, neural networks will be trained with supervision from experimental measurements. This will be the practical situation faced with when use is made of less than one sensor per blade.

Although suitable neural networks take a lot of effort to train, they are very fast and easy to implement.

7.2. Network Feature Selection

It was decided to look at as many as possible features of the signals in order to identify useful those useful for damage detection. A number of the features considered are normally used for condition monitoring of impulse-related rotor defects such as rolling element bearing failure. However, these features were still considered in order to determine whether they will be able do provide additional information along with the use of other signal features. All the features considered are discussed in the following paragraphs and fall into two categories namely time domain features and frequency domain features.

7.2.1. Time Domain Features

Norton [38] outlines a number of time domain signal features, some of which are described in this section. Other time domain features include mean value and standard variation.

7.2.1.1. Root-Mean-Square Value

The mean-square value of a time dependant signal $x(t)$ over an interval T is the average value of $x^2(t)$ and is given by Equation (7-1) as

$$E[x^2] = \frac{1}{T} \int_0^T x^2 \, dt$$

(7-1)

The Root-Mean-Square (RMS) value can then be calculated by simply taking the positive square root of $E[x^2]$ as shown in Equation (7-2):

$$X_{RMS} = \sqrt{E[x^2]} = \sqrt{\frac{\int_0^T x^2(t)dt}{T}}$$

(7-2)

Simply stated, an RMS value is the square root of the average of a squared time dependant signal.

7.2.1.2.   Crest Factor

The crest factor is the ratio of the peak level of $x(t)$ to the RMS value of $x(t)$ and is calculated using Equation (7-3):

$$\text{Crest Factor} = \frac{X_{max}}{X_{RMS}}$$

(7-3)

This serves as a measure of the impulsiveness of a time signal and is commonly used to detect impulsive vibrations caused by damaged bearings.

7.2.1.3.   Kurtosis

The kurtosis of a signal is the fourth statistical moment of the signal's probability density function and is useful for detection of the presence of an impulse in a signal. This is given by Equation (7-4):

$$\text{Kurtosis} = \frac{1}{\sigma^4 T} \int_0^T x^4 dt$$

(7-4)

with σ^2 being the variance of $x(t)$ given by Equation (7-5):

$$\sigma^2 = E[x^2] - \{E[x]\}^2$$

(7-5)

$E[x^2]$ is calculated using Equation (7-1).

Similar to the crest factor, the kurtosis of a signal is normally used for detecting discrete impulse faults in rolling element bearings.

7.2.2.   Frequency Domain

7.2.2.1.   Operational Mode Shape Comparison

A modal analysis is usually performed on a stationary structure using the FRFs of a number of measurement points with one or more known artificial excitation forces as references.   There are however a number of ways to estimate mode shapes from output-only data, i.e. for an unknown input force such as is the case for a rotating fan.

Smit [45] made use of ARMAX models to do damage detection for single blade damage. With this method, natural frequencies and mode shapes as well as input forces can be estimated from output-only time domain data. The accuracy of these estimations depends on the accuracy of the ARMAX models used. Consequently, Smit found that the models need to be of very high order in order to get meaningful results e.g. for data with a sampling frequency of 5120 Hz, 48th order ARMAX models are needed. As an ARMAX model has to be identified for each measurement, this method results in long computational times.

For this reason, it was decided to rather make use of the mode shape extraction method as described by Felber and Ventura [17]. Felber and Ventura made use of Averaged Normalized Power Spectral Densities (ANPSDs) as well as MRFs.

An ANPSD, used for identifying natural frequencies, is calculated as the average of a group of p Normalized Power Spectral Densities (NPSDs) as given by Equation (7-6)

$$ANPSD(f_k) = \frac{1}{p} \sum_{i=1}^{i=p} NPSD_i(f_k)$$

(7-6)

with

$$NPSD_i(f_k) = \frac{PSD_i(f_k)}{\sum_{k=0}^{k=n} PSD_i(f_k)}$$

(7-7)

being the NPSD for f_k (the kth discrete frequency) and n the number of discrete frequencies. The function of the NPSD function is thus to normalize the values of different PSDs to their respective PSD energy levels in order to be comparable.

A PSD is calculated by Equation (7-8) as

$$PSD(f) = \frac{2}{N\Delta t} X(f) X^*(f)$$

(7-8)

for N the number of PSD data points, Δt the sampling increment, $X(f)$ the Fourier transform of $x(t)$ and $X^*(f)$ the complex conjugate of $X(f)$.

A MRF, used for estimating mode shapes, is calculated by

$$M_{a,b}(f) = |TF_{a,b}(f)| PW(f) CW(f)$$

(7-9)

with $TF_{a,b}(f)$ the transfer function, or more correctly, the transmissibility function between two records $\ddot{x}_a(t)$ and $\ddot{x}_b(t)$, $PW(f)$ a Phase-Window function and $CW(f)$ a Coherence-Window function.

$PW(f)$ is calculated as

$$PW(f) = \begin{cases} 1 \text{ for} & 0 \leq \theta(f) \leq \theta_c \\ 0 \text{ for} & \theta_c < \theta(f) < 180° - \theta_c \\ -1 \text{ for} & 180° - \theta_c \leq \theta(f) \leq 180° \end{cases}$$

(7-10)

with $\theta(f)$ the phase function.

$CW(f)$ is calculated as

$$CW(f) = \begin{cases} 1 \text{ for} & \gamma_c^2 \leq \gamma^2(f) \leq 1 \\ 0 \text{ for} & 0 < \gamma^2(f) < \gamma_c^2 \end{cases}$$

(7-11)

with $\gamma_c^2(f)$ the coherence function

Both θ_c and γ_c^2 are chosen arbitrarily.

This method is very simple to implement although it does not yield as accurate and clear results as the ARMAX method does.

7.2.2.2.   Rotational Speed Harmonics

Boek et al. [4] mention that vibrational information useful for distinguishing between different rotor defects of rotating machinery can be found in the amplitudes of the rotational frequency and its associated harmonics. Boek and his co-workers trained neural networks that were able to distinguish between physically different faults such as imbalance and a cracked blade in an experimental setup by using the first three rotational speed harmonics information and the average RMS values of the high frequency end of the measured spectra.

7.2.2.3.   Cepstrum Analysis

Cepstrum analysis is a spectral analysis technique that is used to identify harmonics from PSDs as described by Norton [38], Rao [41] and Wismer [55]. The power cepstrum of a PSD is the inverse Fourier transform of the logarithmic PSD as given in Equation (7-12):

$$C_{pxx}(\tau) = X^{-1}\{\log_{10}[PSD(f)]\}$$

(7-12)

The power cepstrum is useful for amongst others the detection of harmonic patterns in frequency spectra such as for turbine blade failures ([38], [41]). Norton recommends using this technique as a complementary tool to spectral analysis.

7.3. Neural Network Suitability Test

The suitability of neural networks for the purposes of this dissertation was tested on data as measured by Smit [45]. Smit took measurements on the FaBCoM TeSt for single blade damage using two piezoelectric strain sensors and one accelerometer position on the damaged blade as shown in Figure 7-1. An additional accelerometer was placed on an undamaged blade at the same position as the one installed on the damaged blade. For each damage level (0%, 10%, 20%, 30% and 40%), 12 time domain measurements of record length 4 seconds were taken for all four transducers at a sampling frequency of 5120 Hz.

Features which were extracted from the signals, included time domain features (as described in section 7.2.1) and the rotational harmonics values for the z-z direction orientated strain sensor, ANPSD features using the signals from all four transducers as well as MRF features for the two piezoelectric strain sensors with the x-x direction orientated strain sensor as reference.

It was decided to make use of back-propagation networks as used by Boek et al. [4]. A number of these networks were trained using these features, but the best results were obtained using only the rotational harmonic and MRF features. The network yielding the best results consisted of a 5 neuron Tan-Sigmoid Transfer Function (TSTF) input layer and a single neuron Linear Transfer Function (LTF) output layer. The network was trained on 10 of the 12 feature sets extracted for each blade damage level with a 0.01 learning rate and a performance goal of 1×10^{-5}. The network was tested on the remaining feature sets, the results of which are shown in Figure 7-2.
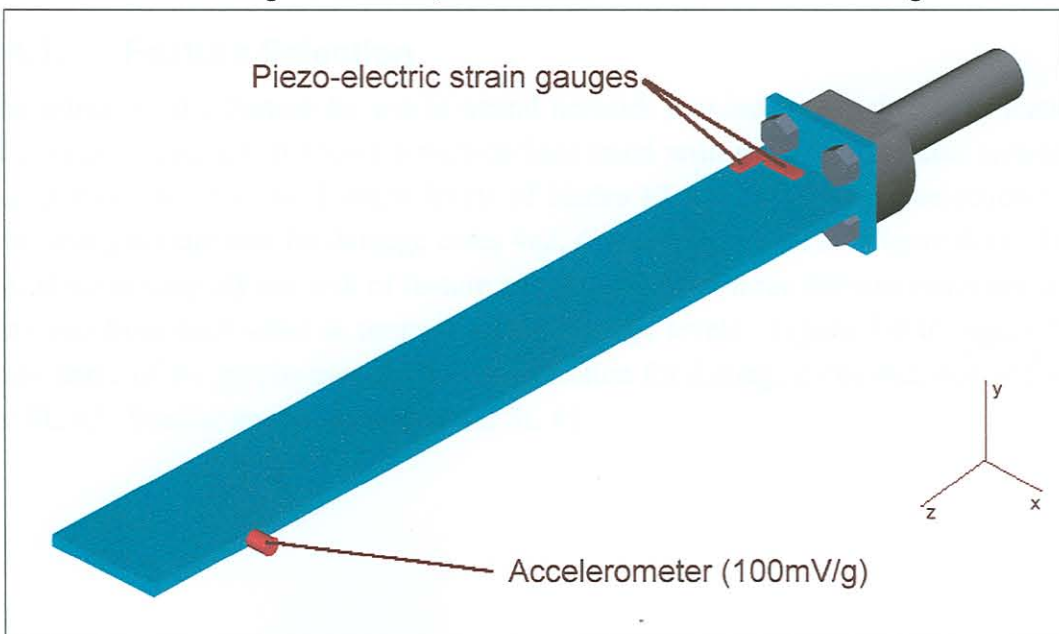
Figure 7-1: Sensor Orientation used by Smit

(from Smit [45])
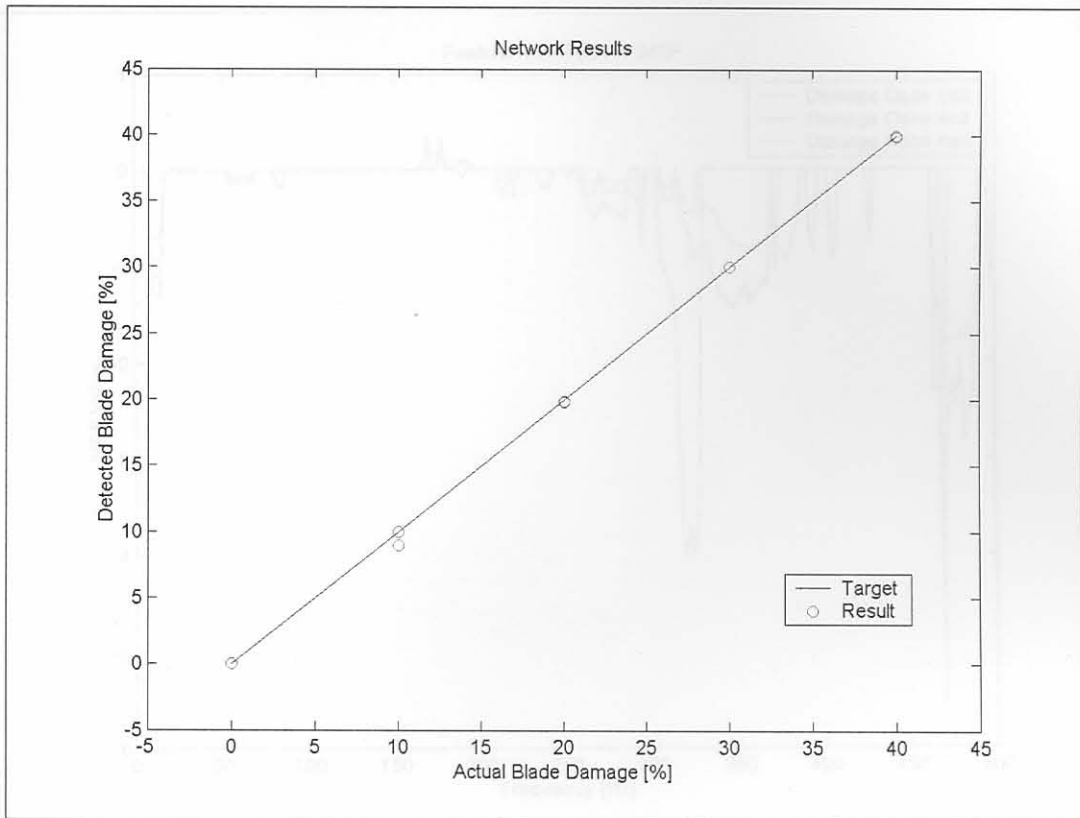
Figure 7-2: Results for Neural Network Suitability Test

From Figure 7-2 it can be concluded that a neural network was trained that is suitable for single blade damage detection when the setup of Smit [45] is used.

7.4. Neural Networks

7.4.1. Feature Selection

The selection of a feature for use in neural network training entails the identification of a dataset feature that shows a well-defined trend with regards to certain variables that in this case, are the damage levels of blades #3 and #4. Feature selection was done using feature sets for damage cases 4a2, 4c4 and 4e6 only (see Figure 6-1). This was done to simplify the task of feature selection as these three damage cases are well removed from each other in terms of blade damage levels. Figure 7-3 to Figure 7-6 show some of the graphs used for feature selection for damage cases 4a2, 4c4 and 4e6 for SL #3. Similar graphs were used for SL #1.
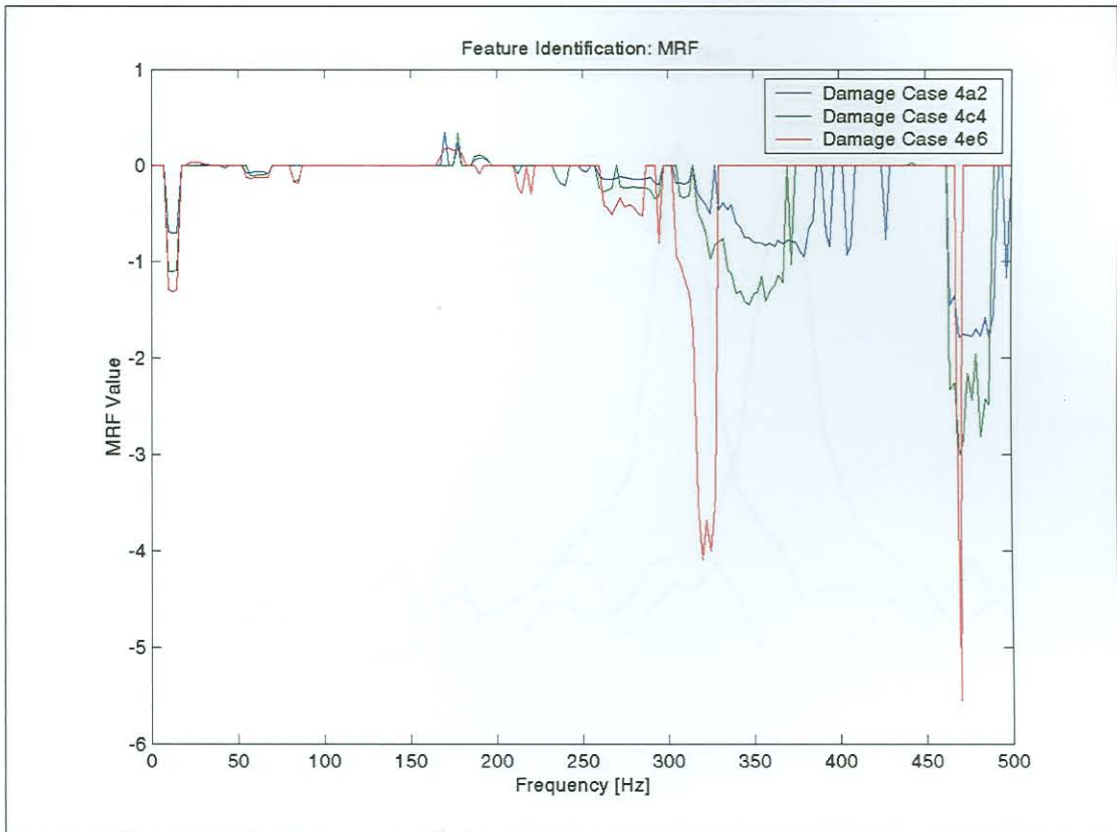
Figure 7-3: MRF Results over 500 Hz Bandwidth for SL #3

Figure 7-3 shows the MRF results for SL #3 over a 500 Hz bandwidth as calculated using Equation (7-9). From Figure 7-3, possible features include the MRF amplitude around 12.5 Hz, the minimum MRF amplitude between 460 Hz and 495 Hz as well as the frequency index of the MRF minimum between 255 Hz and 390 Hz.

Figure 7-4 shows the shift of peaks of the strain sensor PSD function between 1300 Hz and 1370 Hz, identified as feature #11 for SL #3. Figure 7-5 shows the use of PSD energy for the strain sensor data for SL #3 as in feature #8. Here, the PSD energy is obtained by calculating the area underneath the PSD graph from 1795 Hz to 1805 Hz. Definite trends are clearly seen on these figures.
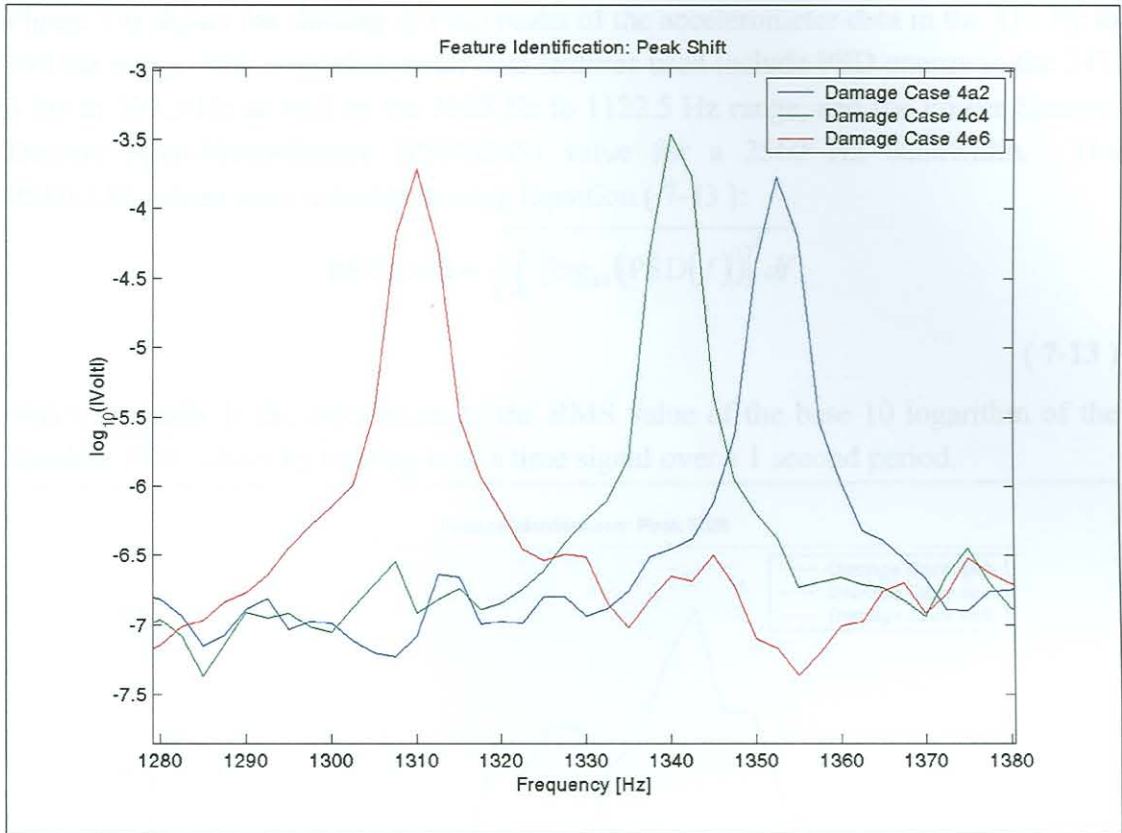
Figure 7-4: SL #3, Feature # 11
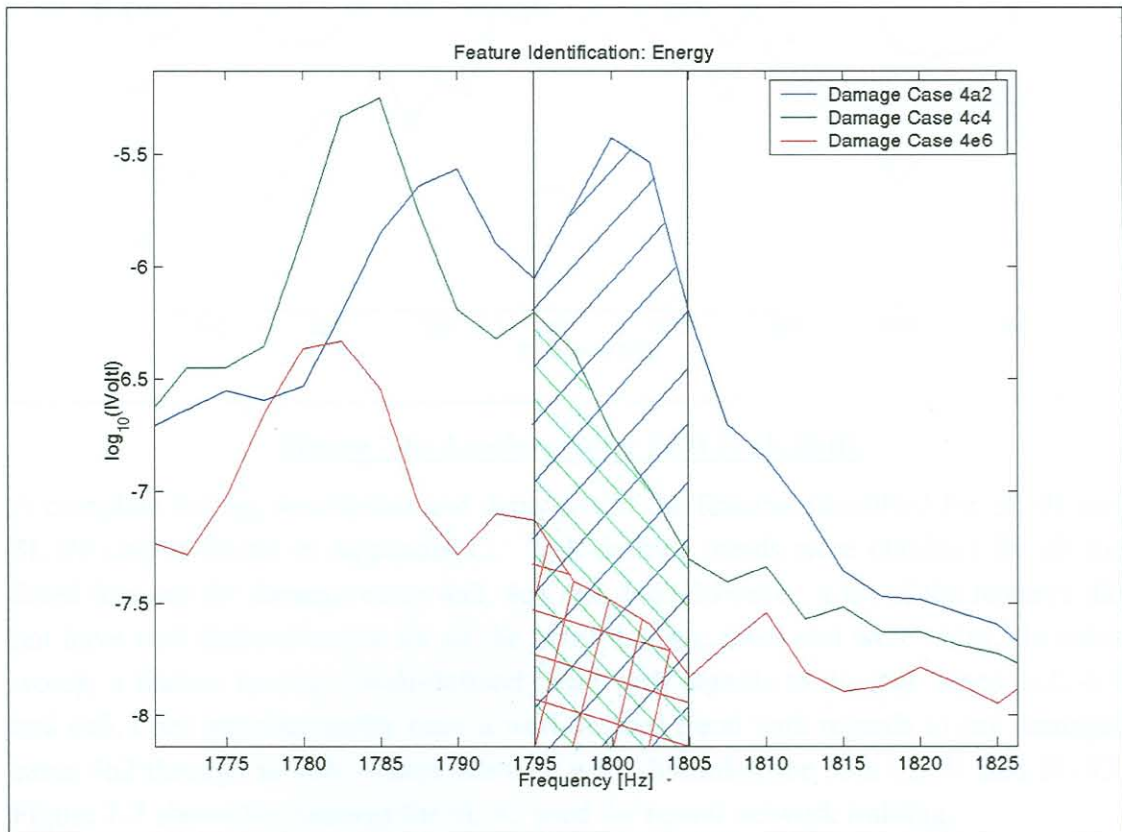
Figure 7-5: SL #3, Feature #8

Figure 7-6 shows the shifting of PSD peaks of the accelerometer data in the 310 Hz to 370 Hz range. Other accelerometer data features used include PSD energy in the 347.5 Hz to 357.5 Hz as well as the 1085 Hz to 1122.5 Hz range, and the Power Spectral Density Root-Mean-Square (PSDRMS) value for a 2560 Hz bandwidth. The PSDRMS values were calculated using Equation (7-13):

$$PSDRMS = \sqrt{\int_{f_0}^{f_1} \left[\log_{10} \left(|PSD(f)| \right) \right]^2 df}$$

(7-13)

which basically is the calculation of the RMS value of the base 10 logarithm of the absolute PSD values by treating it as a time signal over a 1 second period.
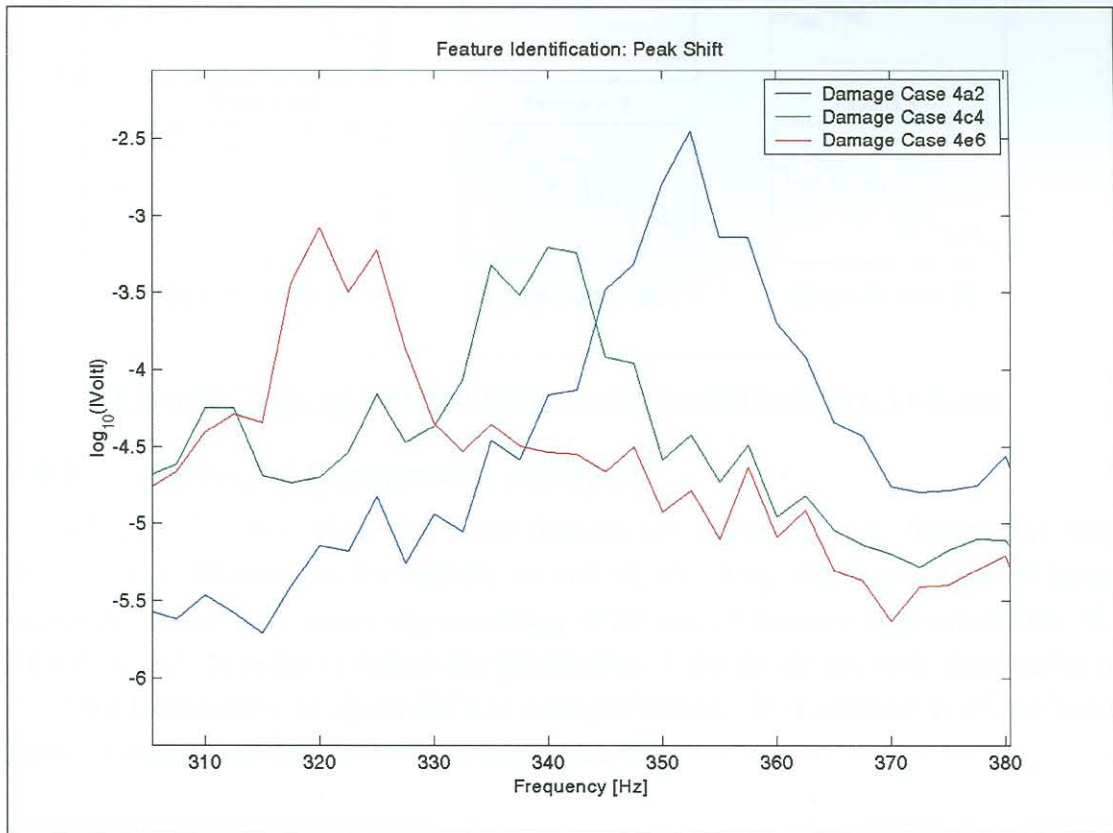
Figure 7-6: Accelerometer PSD Peak Shift

A complete listing, description and depiction of the features identified for SL #1 and SL #3 can be found in Appendix C. Well-defined trends were obtained for all the listed features for damage cases 4a2, 4c4 and 4e6. However, a lot of the features did not have well defined trends for all the other damage cases and were noisy. In other words, a feature having a well-defined trend with regards to damage cases 4a2, 4c4 and 4e6, does not necessarily have a well-defined trend with regards to say damages cases 4a2 through to 4a6. These features were discarded for both SL #1 and SL #3. Figure 7-7 shows the features for SL #3 used for neural network training.
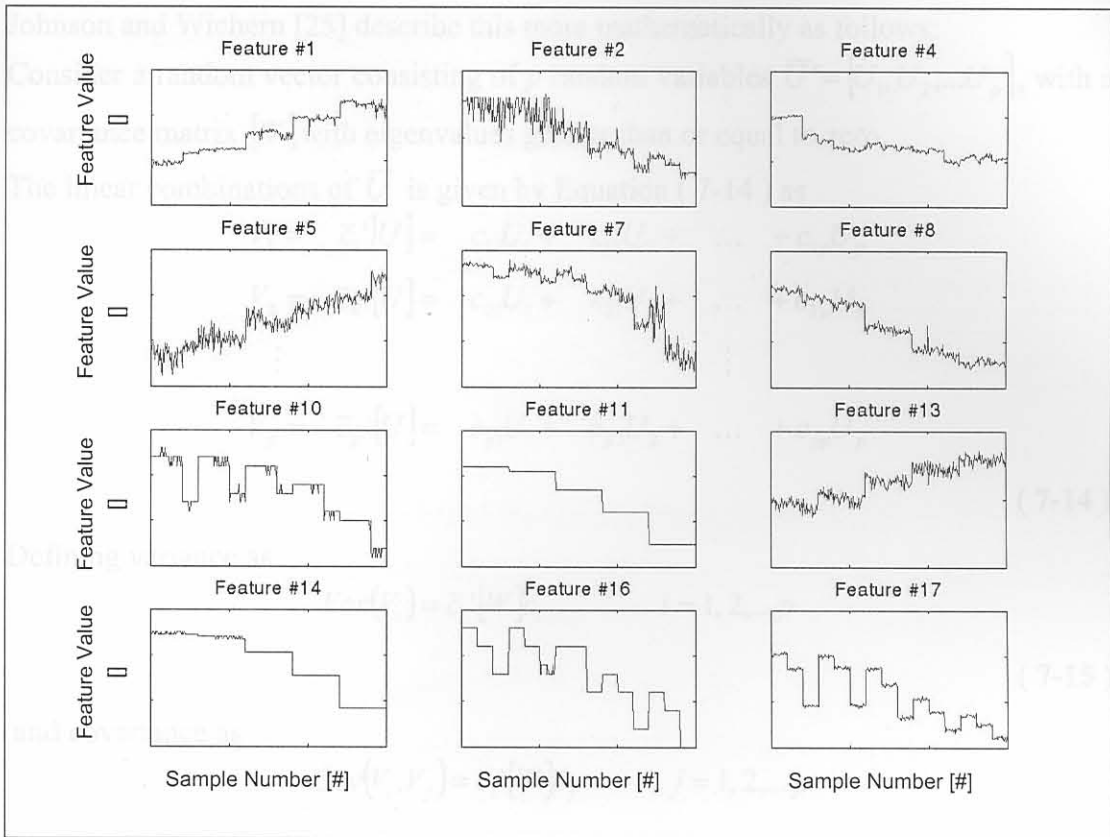
Figure 7-7: SL #3 Selected Features for Neural Network Training

7.4.2. Principal Component Analysis

From Figure 7-7, it is clear that some features are correlated (e.g. feature #11 and feature #14). This occurs for both SL #1 and SL #3. Also, the neural network input vector dimensions are rather big consisting of 20 and 19 features respectively for SL #1 and SL #3. In order to reduce the dimensions of the neural network input vectors, Principal Component Analyses (PCAs) were performed. This resulted in a final input vector dimension of 5x1 for both SL #1 and SL #3.

Principal components are particular linear combinations of a group of random variables considered and are solely dependant on the covariance matrix of the variables as described by Johnson and Wichern ([25]). According to them, PCAs often reveal unsuspected relationships and frequently serve as intermediate steps in larger investigations.

The technique has three effects namely input vector orthogonolisation, orthogonolized component sorting and component elimination ([11]). In other words, the technique first orthogonolizes the input vector so that its components are uncorrelated. It then sorts the resulting components so that those with the largest variation come first. After that, components that contribute least to the data set variation are eliminated.

Johnson and Wichern [25] describe this more mathematically as follows:

Consider a random vector consisting of p random variables $\overline{U}' = [U_1, U_2, \ldots U_p]$, with a covariance matrix $[W]$ with eigenvalues greater than or equal to zero.

The linear combinations of $\overline{U}$ is given by Equation (7-14) as

$$V_1 = \overline{c}_1'[U] = c_{11}U_1 + c_{12}U_2 + \ldots + c_{1p}U_p$$
$$V_2 = \overline{c}_2'[U] = c_{21}U_1 + c_{22}U_2 + \ldots + c_{2p}U_p$$
$$\vdots \qquad\qquad \vdots$$
$$V_p = \overline{c}_p'[U] = c_{p1}U_1 + c_{p2}U_2 + \ldots + c_{pp}U_p$$

(7-14)

Defining variance as

$$Var(V_i) = \overline{c}_i'[W]\overline{c}_i \qquad i = 1, 2, \ldots p$$

(7-15)

and covariance as

$$Cov(V_i, V_j) = \overline{c}_i'[W]\overline{c}_j \qquad i, j = 1, 2, \ldots p$$

(7-16)

the ith principal component will be the linear combination $\overline{c}_i'\overline{U}$ that maximizes $Var(\overline{c}_i'\overline{U})$ for $\overline{c}_i'\overline{c}_i = 1$ and $Cov(\overline{c}_i'\overline{U}.\overline{c}_j'\overline{U}) = 0$ for $j < i$.

7.4.3. Network Architecture

Several neural networks were trained and tested in order to determine suitable network architecture. This was done using features extracted from data measured for the adjacent blade damage scenario as explained in Chapter 6. All the networks trained were feed-forward networks using back-propagation training. The best results were obtained for four layer networks with two outputs with the first two layers using TSTFs and the remaining two layers making use of LTFs.

Subsequently, all neural networks referred to further on in this paper, have this architecture. One could argue that due to the complex nature of the damage classification to be done, complex network architecture needs to be used. Figure 7-8 presents a graphical presentation of such network architecture for a 5-neuron input layer, two 5-neuron hidden layers, 2-neuron output layer (5x5x5x2) network.
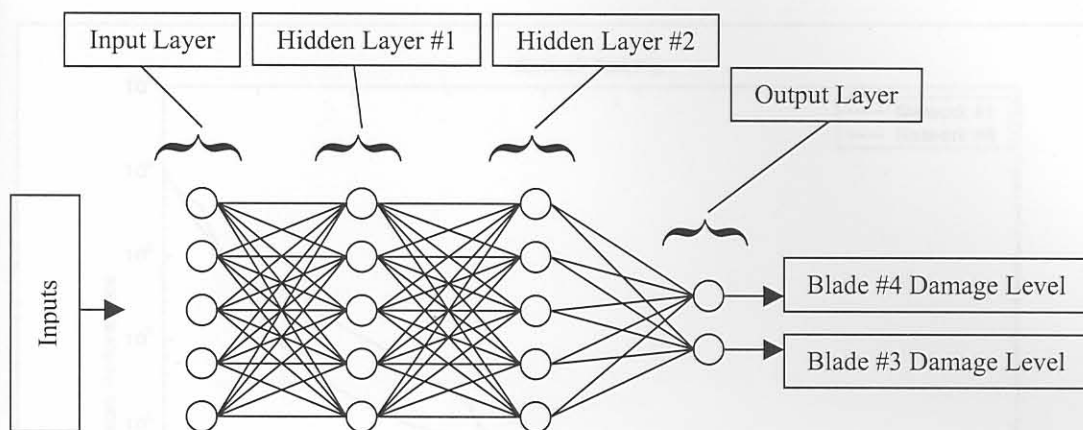
Figure 7-8: 5x5x5x2 Neural Network Architecture

For SL #1, a 20x20x20x2 network yielded the best results whereas for SL #3, a 10x10x10x2 network yielded the best results.

7.4.4.   Network Training

As already mentioned, two networks were trained. The networks trained for SL #1 and SL #3 will be referred to as Network #1 and Network #3 respectively. The networks were trained on 20 feature sets extracted from 20 of the 24 measured datasets for each of the damage cases of the 1st, 3rd and 5th columns of the damage case matrix given in Figure 6-1. Both networks were trained using the same parameters listed in Table 7-1 using the Levenberg-Marquardt training algorithm.

Table 7-1: Neural Network Training Parameters

Training Parameter	Value
Performance Goal	0.001
Learning Rate	0.01
Epochs	2000

All other training parameters used the default values assigned by the Neural Network Toolbox for Matlab. Figure 7-9 shows the logarithmic network performance during training of Networks #1 and #3.
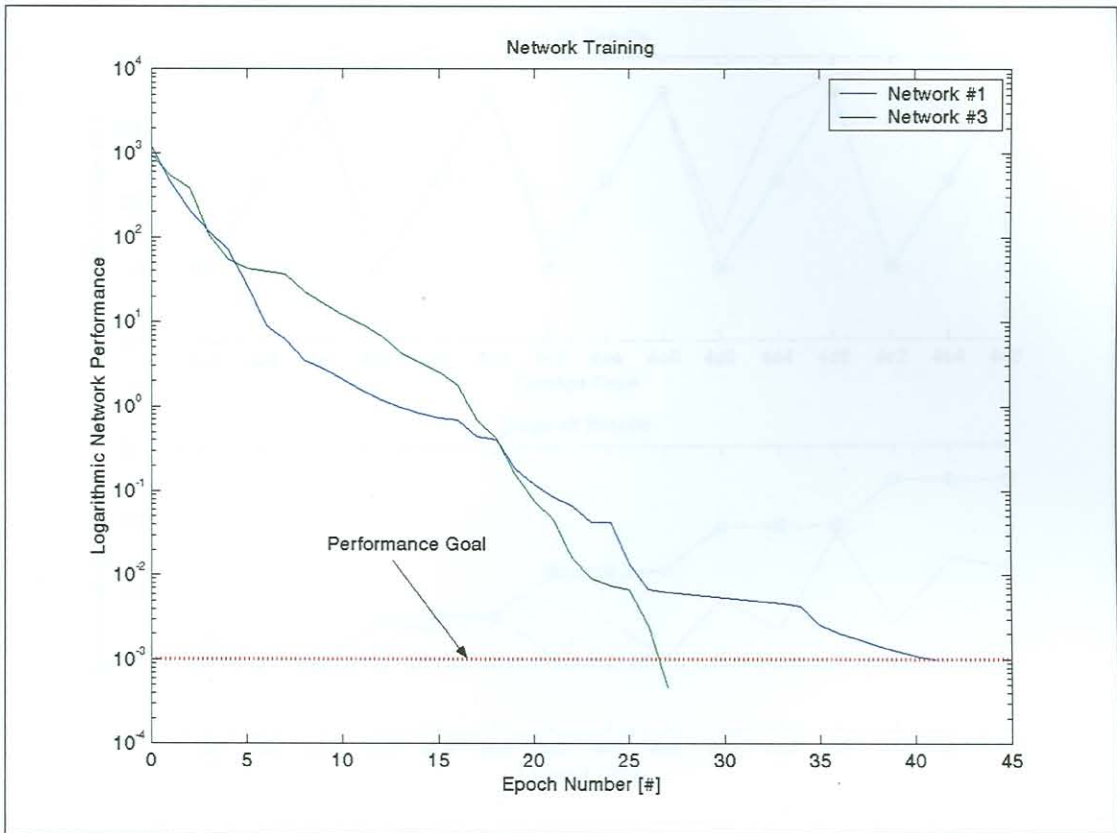
Figure 7-9: Training of Network #1 and Network #3

7.5. Results

In this section, the results of the neural networks are presented in terms of trained damage levels and untrained damage levels. The reason why the networks were tested for untrained damage levels was to test the ability of the networks to interpolate between damage levels for which they trained. Also, the damage level extrapolation capabilities of the networks were tested for damage cases 2a4 and 2a6, which represent a 3-blade damage scenario as described in Section 6.4. Also, to test the robustness of Network #1, it was tested with feature sets for SL #2. The same features were extracted as those for SL #1. The results obtained from Network #1 for SL #2 will be referred to as Network #2.

Figure 7-11 to Figure 7-13 (the key of which is given in Figure 7-10) give the mean results for Networks #1, #2 and #3. It was decided to average the network results as individual results proved to be a bit noisy.
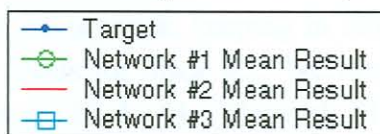
Figure 7-10: Key for Figure 7-11 to Figure 7-13

68
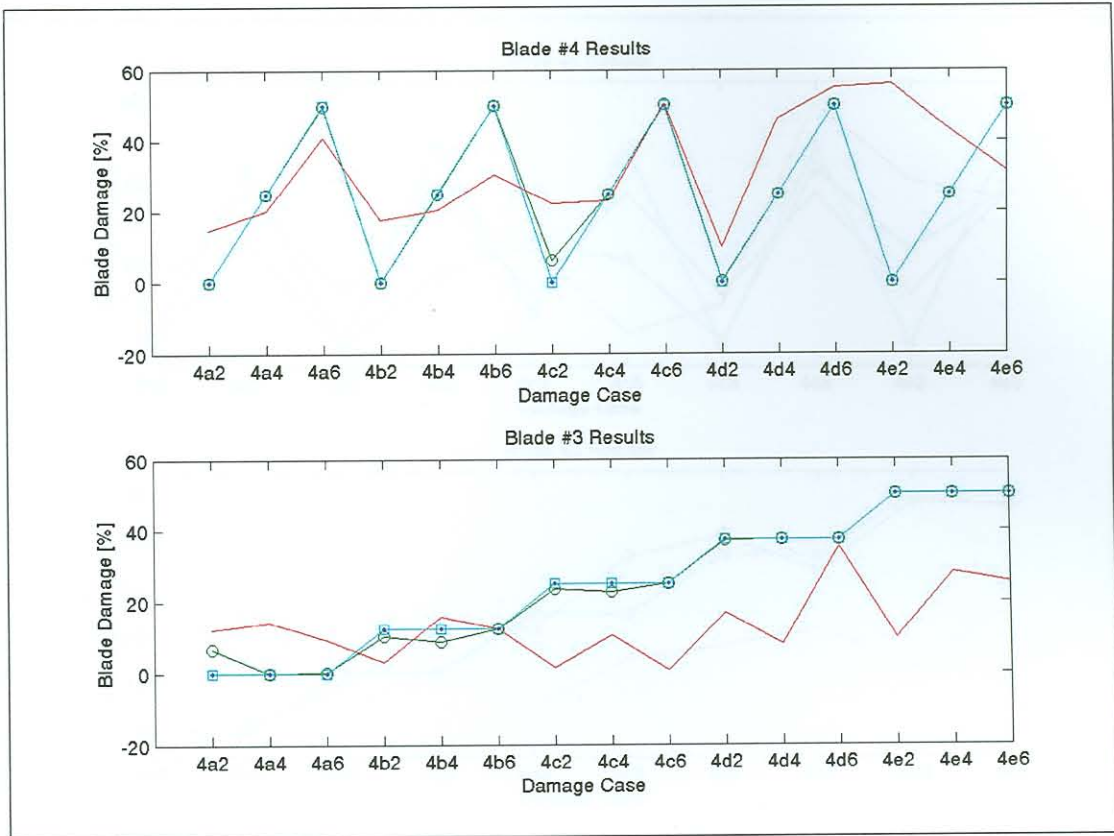
Figure 7-11: Results for Trained Damage Levels

Figure 7-11 gives the mean results for the trained damage levels of the networks. This was done as preliminary network tests. For Networks #1 and #3, the features sets used were those extracted from the remaining four of the 24 measured datasets as mentioned in section 7.4.4. For Network #2, the feature sets from all 24 measured datasets for each of the damage cases as described in section 7.4.4 were used for testing.

From Figure 7-11 it can be seen that Networks #1 and #3 perform very well. However, the results from Network #2 is not as good, especially for damage level detection of blade 3. The reason for the very poor results for damage cases 4e2, 4e4 and 4e6, is that the strain sensor on blade #2 got loose during testing of blade 4e, as mentioned in Chapter 6.

Figure 7-12 gives the mean results of the networks for damage level interpolation. From the three networks, Network #3 performs the best. Excellent damage detection is obtained for blade #3 by the network, keeping in mind that all the networks were trained for all the damage levels for blade #3. Network #3 performs rather well in terms of damage detection for blade #4. Network #1 performs less well but still acceptable for blade #3 damage detection. It does not perform very well for damage detection of blade #4. The results of Network #2 proved to be rather useless.
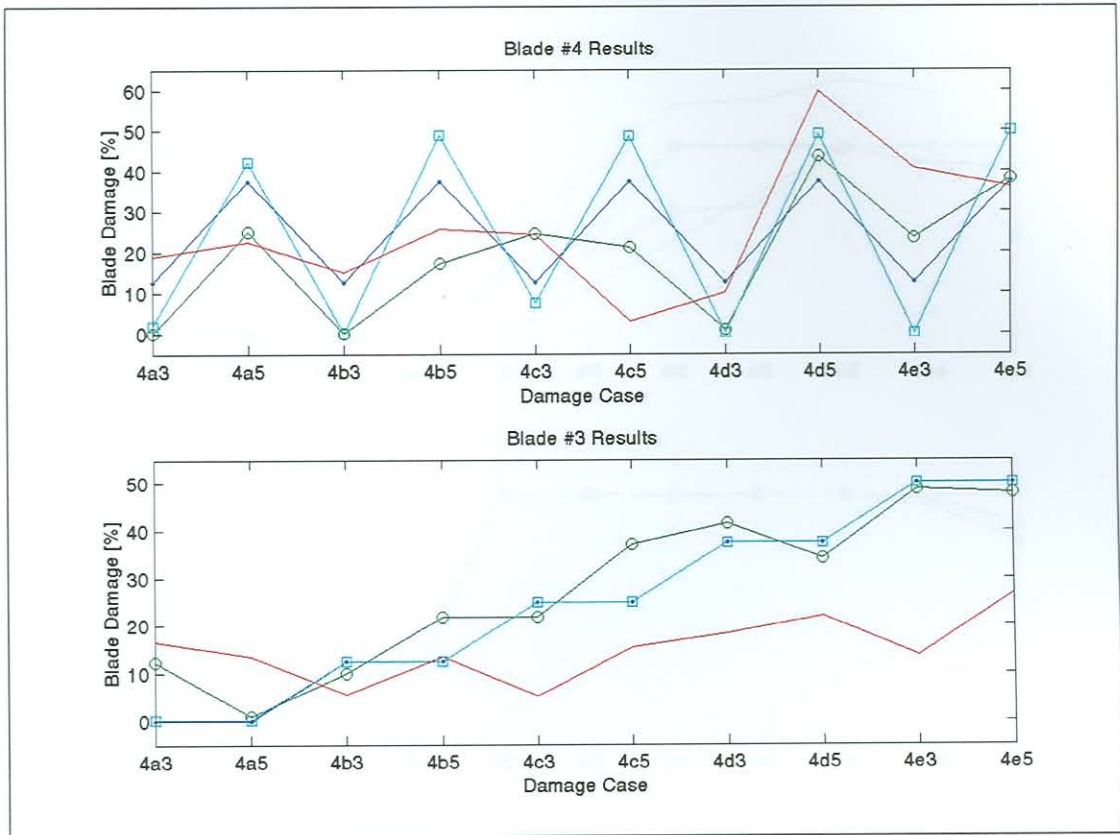
Figure 7-12: Results for Damage Level Interpolation

Figure 7-13 gives the results for extra feature sets not used in network training as well as two damage cases, namely 2a4 and 2a6, for which the networks were not trained. It can be seen for damage cases 2a4 and 2a6, that Network #1 and Network #3 interpret the additional damage as damage reduction both for blades #4 and #3 although this is more apparent for blade #3. From this, it is safe to conclude that the networks will be able to do damage classification for three blades and perhaps all four blades if trained to do so. Also, it can be concluded that if the networks find the structural health to improve, it is possibly due to the incorrect interpretation of additional damage.

Feature sets from damage cases 4b1, 4c1, 4d1 and 4e1 were used to test the robustness of the networks in terms of blade manufacturing and installation tolerances. These damage cases are all equal in terms of damage levels to the undamaged case 4a2, the feature sets of which was used to train the networks. As seen from Figure 7-13 Network #1 and Network #3 perform very well for these damage cases.
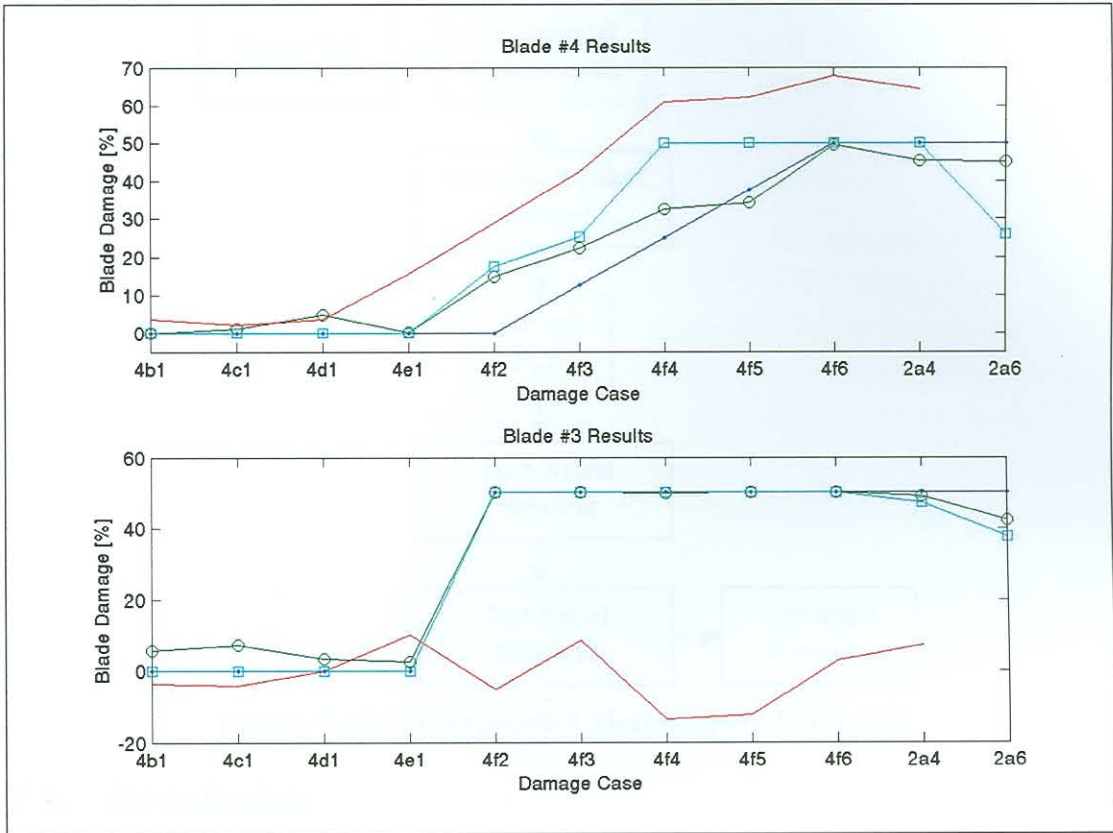
Figure 7-13: Results for Extra Datasets and Untrained Damage Cases

The measurements taken for blade #4f were basically a re-test for blade #4e as the strain gauge on blade #2 came loose during testing for blade #4e. Again, very good results are obtained from Network #1 and Network #3 for blade #3 damage detection. Less good results for Networks #1 and #3 are obtained for blade #4 damage detection. Network #2 performed poorly for the extra datasets as seen on Figure 7-13.

7.6. *Experimental Methodology Summary*

The experimentally supervised neural network damage detection methodology is summarized in Figure 7-14. The methodology consists mainly of a design, testing, network training and network implementation phase. As can be seen, this methodology is relatively simple.
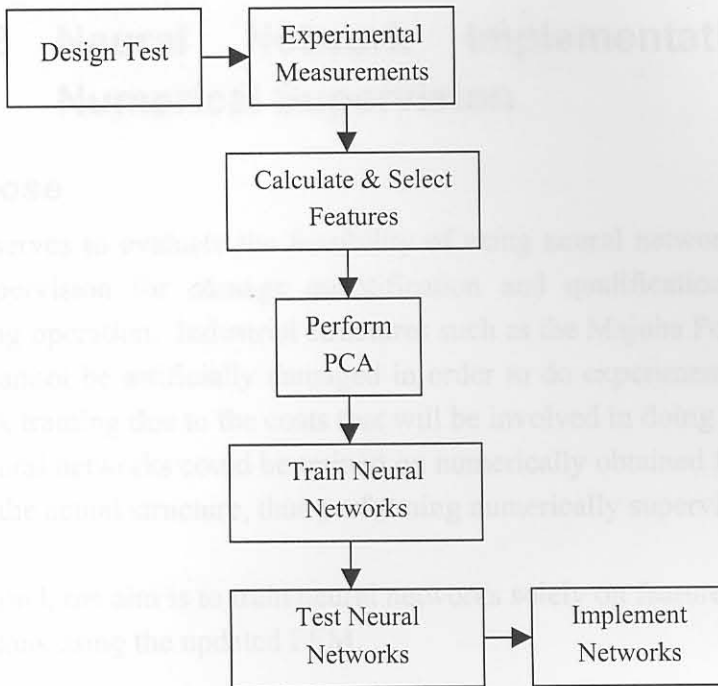
Figure 7-14: Experimental Methodology Summary

7.7. Conclusion

In this chapter, the ability of neural networks to do on-line blade damage quantification and qualification with data obtained from sensors not necessarily installed on the damaged blades, was proved for experimentally supervised training. Excellent results where obtained for all damage cases for which the networks were trained. However, the networks were found to be limited in terms of damage level interpolation and extrapolation. It was also found that a neural network trained for a specific sensor location, couldn't be used for a different sensor location.

Thus it can be concluded that in order to do accurate damage detection making use of neural networks, the networks must be trained for as many damage levels, damage scenarios and sensor locations as possible.

Chapter 8 Neural Network Implementation with Numerical Supervision

8.1. Purpose

This chapter serves to evaluate the feasibility of using neural networks trained with numerical supervision for damage quantification and qualification on an actual structure during operation. Industrial structures such as the Majuba Power Station FD and ID fans cannot be artificially damaged in order to do experimentally supervised neural network training due to the costs that will be involved in doing so. It would be ideal if the neural networks could be trained on numerically obtained features in order to be used on the actual structure, thus performing numerically supervised training.

With this in mind, the aim is to train neural networks solely on features obtained from FEM calculations using the updated FEM.

8.2. Introduction

Unlike in Chapter 7 where a lot of features were available to choose from, the only features available for network training are FRF energies and peak shifts obtained from the FEM. Although it is possible to obtain time signal estimations from the FEM, the accuracy of these estimations will be very doubtful due to the differences in excitation between the FaBCoM TeSt during operation and the FEM during testing. The reason why GMSFs cannot be used directly as features for neural network training, is the effect of modal density as described in Section 3.5.

In order to be able to use the neural networks trained on numerically obtained features for damage identification on the FaBCoM TeSt, several issues need to be taken into account:

- The FEM node or element locations, from which FRFs are to be calculated, should correspond to the FaBCoM TeSt sensor locations and orientations.
- The FEM result types should correspond to the FaBCoM TeSt measurement types. In other words, FEM FRFs should be calculated using strain or acceleration corresponding to the FaBCoM TeSt transducer measurements.
- Normalization of the experimentally obtained features to the numerical ones will probably be needed due to the differences between the two test procedures.
- The same frequency resolutions should be used for both numerical and experimental features.

8.3. FEM Testing Procedure

Figure 8-1 shows the setup for the FEM FRF calculations with the measurement locations corresponding to those of the experimental setup as well as the blade numbers.
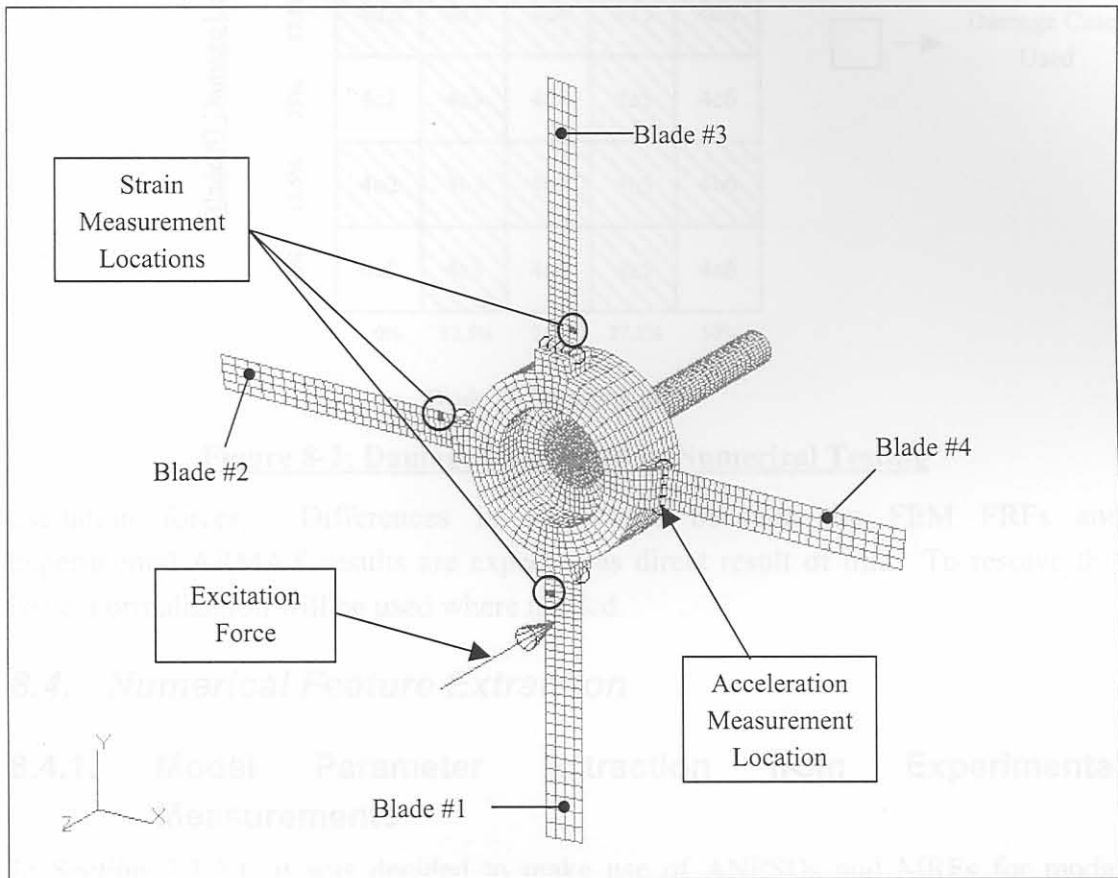
Figure 8-1: FEM Test Setup

The FEM can only be tested for blade root damage increments of 25%. This is due to the element mesh resolution of the blades as described in Section 2.3. As in Chapter 6, damage was simulated at blade #3 and blade #4. The same procedure was followed as depicted in Figure 6-3 except for the damage increments being 25% and not 12.5%. Comparing to Figure 6-1, Figure 8-2 gives the damage cases used for FEM testing. Damage was simulated in the FEM by deleting appropriate MPCs. This is similar to the nodal dissociation method used by Smit [45] for crack modelling.

The point of excitation as shown in Figure 8-1 was chosen to be the same as that used in the EMA for the reason of allowing torsional, sideways and normal excitation of the structure. A constant excitation force of 1 N was chosen over an excitation bandwidth of 2000 Hz at 2.5 Hz intervals. Thus a single white noise input force is simulated corresponding to turbulent forces experienced by operational wind turbines ([2]). In the FaBCoM TeSt however, the force inputs are more complex as they are distributed forces and comprise of turbulent force inputs as well as rotational excitation by the electric motor, blade pass frequency excitation and other operational
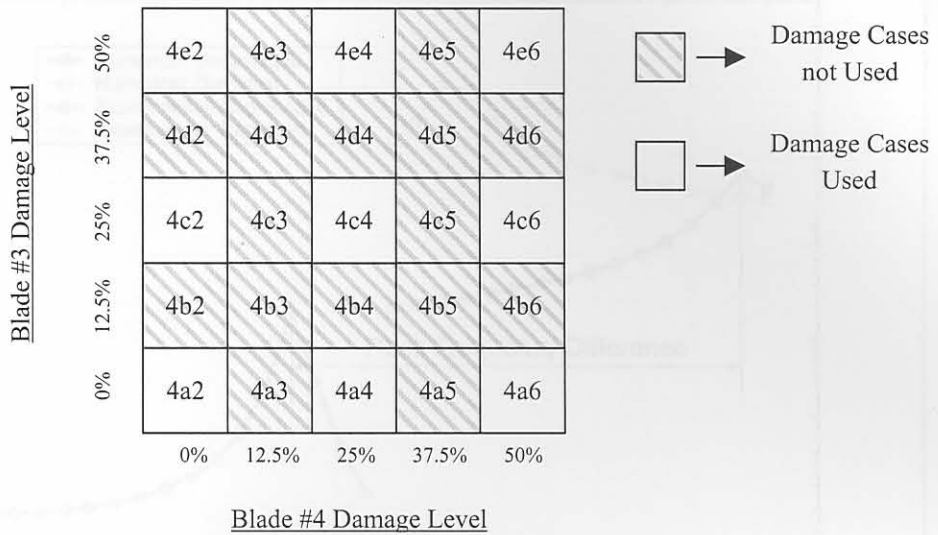
Figure 8-2: Damage Cases used in Numerical Testing

excitation forces. Differences in amplitudes between the FEM FRFs and experimental ARMAX results are expected as direct result of this. To resolve this issue, normalization will be used where needed.

8.4. Numerical Feature Extraction

8.4.1. Modal Parameter Extraction from Experimental Measurements

In Section 7.2.2.1, it was decided to make use of ANPSDs and MRFs for modal parameter extraction instead of ARMAX modelling due to computational costs. However, ANPSDs and MRFs were found to be much less accurate then ARMAX models results. Also, once an ARMAX model is estimated for a time signal, it is very easy to obtain modal frequencies for that model. Smit [45] used 48th order ARMAX models as he found this to be sufficient for datasets with sampling frequencies of 5120 Hz and a bandwidth of 2000 Hz. As the same experimental setup was used in this dissertation as in Smit's, it was decided to use the same order ARMAX models. The software used to calculate the ARMAX models was the System Identification Toolbox Version 5 for Matlab.

8.4.2. Peak Frequency Normalization

As described in Section 5.1.2, not all the natural frequencies of the FEM are equal to that of the FaBCoM TeSt. For this reason, FRF peak normalization in terms of frequencies needs to be done as shown in Figure 8-3 for EMS #4. For frequency normalization, use was made of factorisation. The frequency ranges used for FEM FRF peak identification were chosen to be from 5 Hz below the modal frequencies for 50% damage of blades #3 and #4, and to 5 Hz above the modal frequencies for the

75
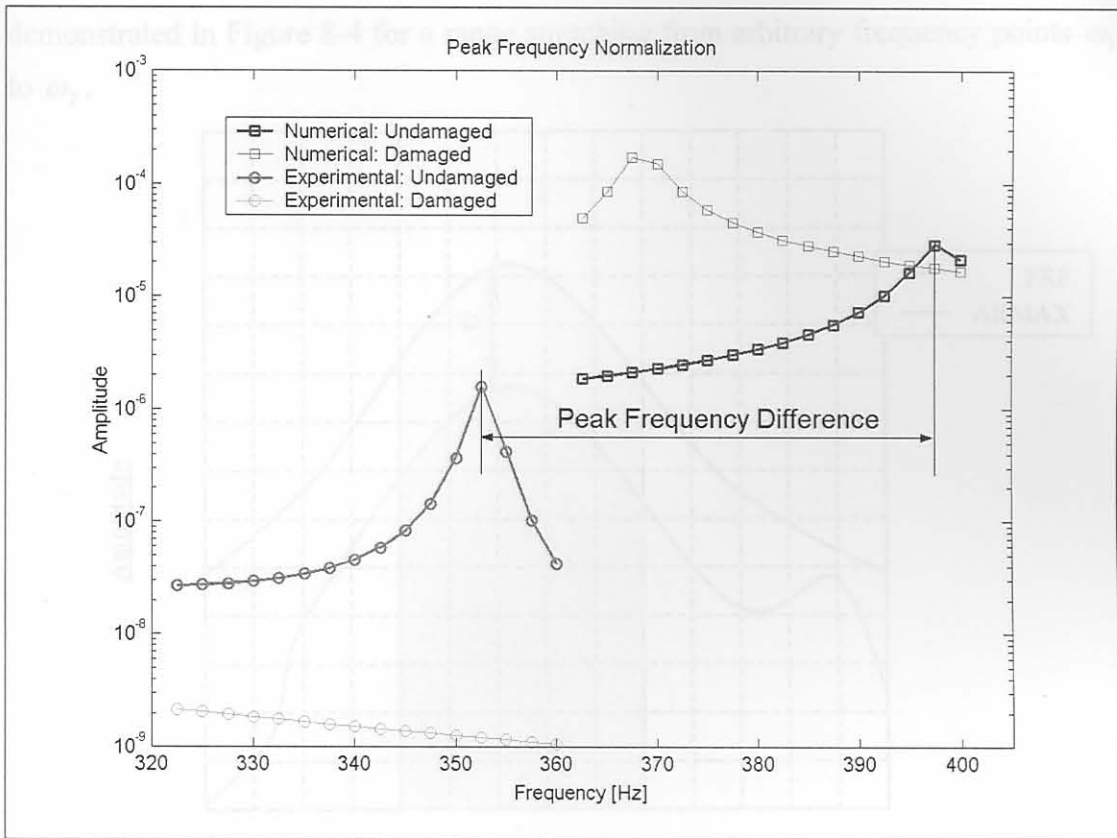
Figure 8-3: Peak Frequencies for EMS #4

undamaged case. For experimental peak identification, the top frequency limits were chosen to be 5 Hz above the experimental modal frequencies for the undamaged case. The lower ranges were determined by the ranges used in the corresponding FEM in order to obtain the same number of curve points for the respective experimental and FEM ranges. To explain this more mathematically, let the FEM FRF peak frequency range for a specific peak stretch from a lower limit ω_1 to a higher limit ω_2. If the frequency range for the corresponding experimental peak stretches from a lower limit ω_3 to ω_4, then the limit differences are equal as given by Equation (8-1):

$$\omega_2 - \omega_1 = \omega_4 - \omega_3$$

(8-1)

8.4.3. Energy Normalization

As discussed in Section 8.3, differences in amplitudes between the FEM FRFs and experimental ARMAX results are expected. This is also confirmed in Figure 8-3. Energy normalization was performed only after peak normalization was performed.

The first step of normalization of numerically obtained features to experimental features is based on the assumption that for a certain frequency range, the amplitudes of a numerical FRF will differ to that of the corresponding experimental ARMAX model FRF amplitudes by a constant over that range. This is graphically

demonstrated in Figure 8-4 for a range stretching from arbitrary frequency points ω_1 to ω_2.
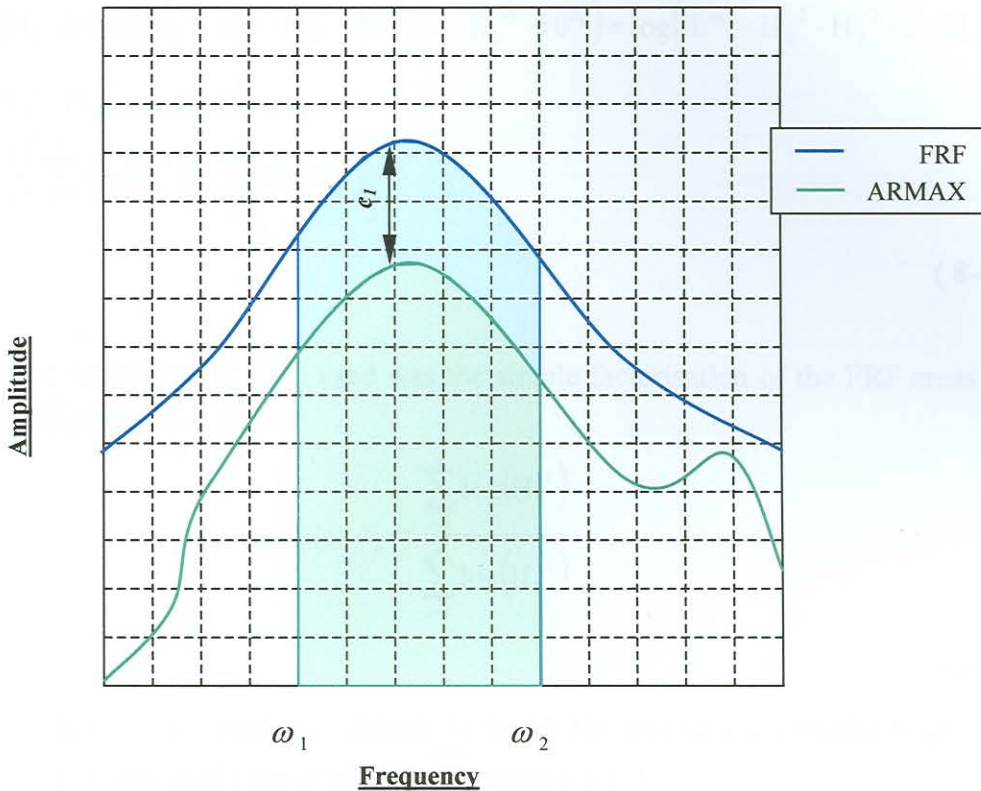
Figure 8-4: Frequency Response Function Offset Assumption

To express this mathematically, let $H_1(\omega)$ and $H_2(\omega)$ be an experimental ARMAX model FRF and a numerical FRF respectively at an arbitrary frequency within a frequency range stretching from ω_1 to ω_2, so that

$$\log(H_1) = \log(H_2) + c_1$$
$$\therefore \log(H_1) - \log(H_2) = c_1$$
$$\therefore \log\left(\frac{H_1}{H_2}\right) = c_1$$
$$\Rightarrow \frac{H_1}{H_2} = 10^{c_1}$$

(8-2)

For n discrete points over this frequency range, the area underneath the curve H_1 over the range is given by

$$\sum_{i=1}^{n} \log\left(H_1^{i}\right) = \log\left(H_1^{1}\right) + \log\left(H_1^{2}\right) + \ldots + \log\left(H_1^{n}\right) = \log\left(H_1^{1} \cdot H_1^{2} \cdot \ldots \cdot H_1^{n}\right)$$

(8-3)

Equation (8-3) can also be written for H_2.

Using Equation (8-2) and assuming c_1 remains constant over the specified range, Equation (8-4) is obtained:

$$\sum_{i=1}^{n} \log\left(H_1^i\right) = \log\left(H_2^1 \cdot 10^{c_1} \cdot H_2^2 \cdot 10^{c_1} \cdot \ldots \cdot H_2^n \cdot 10^{c_1}\right) = \log\left(10^{nc_1} \cdot H_2^1 \cdot H_2^2 \cdot \ldots \cdot H_2^n\right)$$

$$= \log\left(H_2^1 \cdot H_2^2 \cdot \ldots \cdot H_2^n\right) + nc_1$$

$$\therefore c_1 = \frac{1}{n}\left[\sum_{i=1}^{n} \log\left(H_1^i\right) - \sum_{i=1}^{n} \log\left(H_2^i\right)\right]$$

(8-4)

The second normalization step used was the simple factorisation of the FRF areas as given in Equation (8-5):

$$c_2 = \frac{\displaystyle\sum_{i=1}^{n} \log\left(H_1^i\right)}{\displaystyle\sum_{i=1}^{n} \log\left(H_2^i\right)}$$

(8-5)

The frequency ranges used was chosen to be 10 Hz around each modal frequency (ω_m) for the undamaged case as given in Equation (8-6):

$$\omega_1 = \omega_m - 5\,\text{Hz} \text{ and } \omega_2 = \omega_m + 5\,\text{Hz}$$

(8-6)

To obtain the final normalized energies, these two normalization steps are combined as given for a frequency range by Equation (8-7):

$$\text{Normalized Energy} = \frac{1}{2}\left[\left(\sum_{i=1}^{n} \log\left(H_2^i\right) + nc_1\right) + \left(c_2 \times \sum_{i=1}^{n} \log\left(H_2^i\right)\right)\right]$$

(8-7)

With the frequency resolution used (as described in Section 8.3) together with the frequency range definition given by Equation (8-6), it means that the number of discrete points in these ranges, n, will be equal to five.

8.5. Neural Network Training

Several neural networks were trained with different goals in mind namely global damage quantification, global damage qualification, sensor position identification, blade #3 damage quantification and blade #4 damage quantification. For each of these, several networks of different complexities in terms of network architecture were trained in order to make use of neural network committees as suggested by Marwala [33]. In this way, the unique characteristics of the different networks were

combined to yield the best results. The network architectures used in each network committee are listed in Table 8-1.

<p align="center">**Table 8-1: Network Committees Network Architectures**</p>

		Global Blade Damage			
	Network Number	4	5	6	7
	Dimensions	12x1	11x1	10x1	9x1
Transfer Function	Layer 1	TSTF	TSTF	TSTF	TSTF
	Layer 2	LTF	LTF	LTF	LTF
	Layer 3	-	-	-	-
	Layer 4	-	-	-	-
	Committee	Multiple Blade Damage			
	Network Number	1	15	16	17
	Dimensions	6x4	12x4	12x6x4	12x10x4
Transfer Function	Layer 1	TSTF	TSTF	TSTF	TSTF
	Layer 2	LTF	LTF	TSTF	TSTF
	Layer 3	-	-	LTF	LTF
	Layer 4	-	-	-	-
	Committee	Blade Identification			
	Network Number	2	3	8	9
	Dimensions	6x8x1	6x8x4x1	12x1	10x1
Transfer Function	Layer 1	TSTF	TSTF	TSTF	TSTF
	Layer 2	TSTF	TSTF	LTF	LTF
	Layer 3	LTF	TSTF	-	-
	Layer 4	-	LTF	-	-
	Committee	Blade #3 Damage			
	Network Number	18	19	20	21
	Dimensions	12x6x2x1	12x1	12x6x1	12x6x2x1
Transfer Function	Layer 1	TSTF	TSTF	TSTF	TSTF
	Layer 2	TSTF	LTF	TSTF	TSTF
	Layer 3	TSTF	-	LTF	TSTF
	Layer 4	LTF	-	-	LTF
	Committee	Blade #4 Damage			
	Network Number	10	12	13	14
	Dimensions	12x1	12x6x2x1	6x6x2x1	6x8x2x1
Transfer Function	Layer 1	TSTF	TSTF	TSTF	TSTF
	Layer 2	LTF	TSTF	TSTF	TSTF
	Layer 3	-	TSTF	TSTF	TSTF
	Layer 4	-	LTF	LTF	LTF

Three sets of training data were used, containing the features extracted for all of the nine damage cases from the FEM strain FRFs of blades #1, #2 and #3 respectively as well as from the rotational FEM acceleration FRFs at the root of blade #4. Each dataset consisted of the a total of six features namely the frequency shifts of EMSs #4

and #6 as well as the energies of EMS #X for both the strain signal from the particular blade for the training set and the rotational acceleration signal.

8.6. Neural Network Testing

All the network committees were tested using nine additional experimental data sets for each of testing sets #1, #2 and #3 as listed in Table 8-2. The results yielded are presented in Figure 8-5 to Figure 8-9 with the damage cases numbered sequentially according to dataset number. Each testing set number indicates which blade's strain signal features were used for that dataset. As in Chapter 7, the results yielded were averaged to obtain more representative results.

Table 8-2: Training and Testing Sample Numbering

Damage Case	Sample #		
	Testing Set #1	Testing Set #2	Testing Set #3
4a2	1	10	19
4c2	2	11	20
4e2	3	12	21
4a4	4	13	22
4c4	5	14	23
4e4	6	15	24
4a6	7	16	25
4c6	8	17	26
4e6	9	18	27

First, the use of a neural network committee for global damage quantification was explored. Rather good results are obtained as shown in Figure 8-5. This network committee is a bit conservative with regards to global blade damage detection when blade #4 is undamaged, as a higher damage level is detected than what is actually present. The results are roughly similar for all three training sets.

Networks were then trained for quantifying damage for all four blades simultaneously. Figure 8-6 shows the network committee results where it can be seen that very good results are obtained for blade #3 damage detection while less well results are obtained for blade #4.
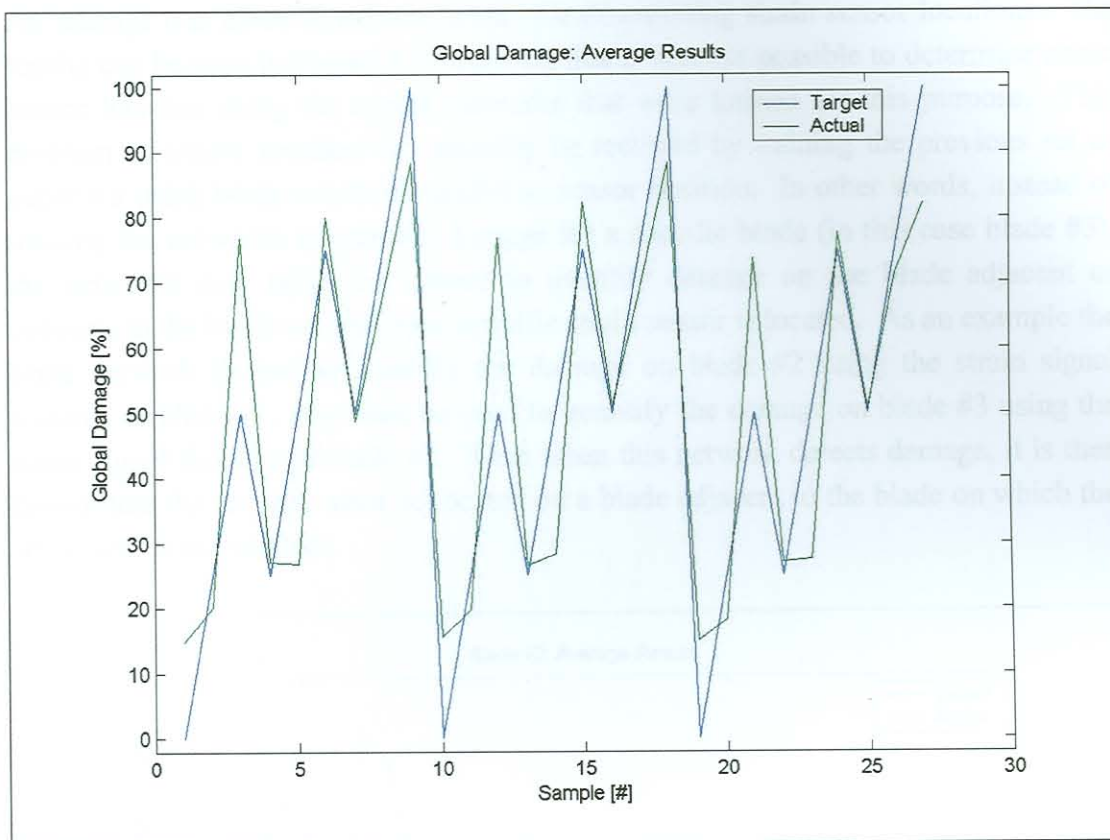
Figure 8-5: Global Blade Damage Detection Network Committee Results
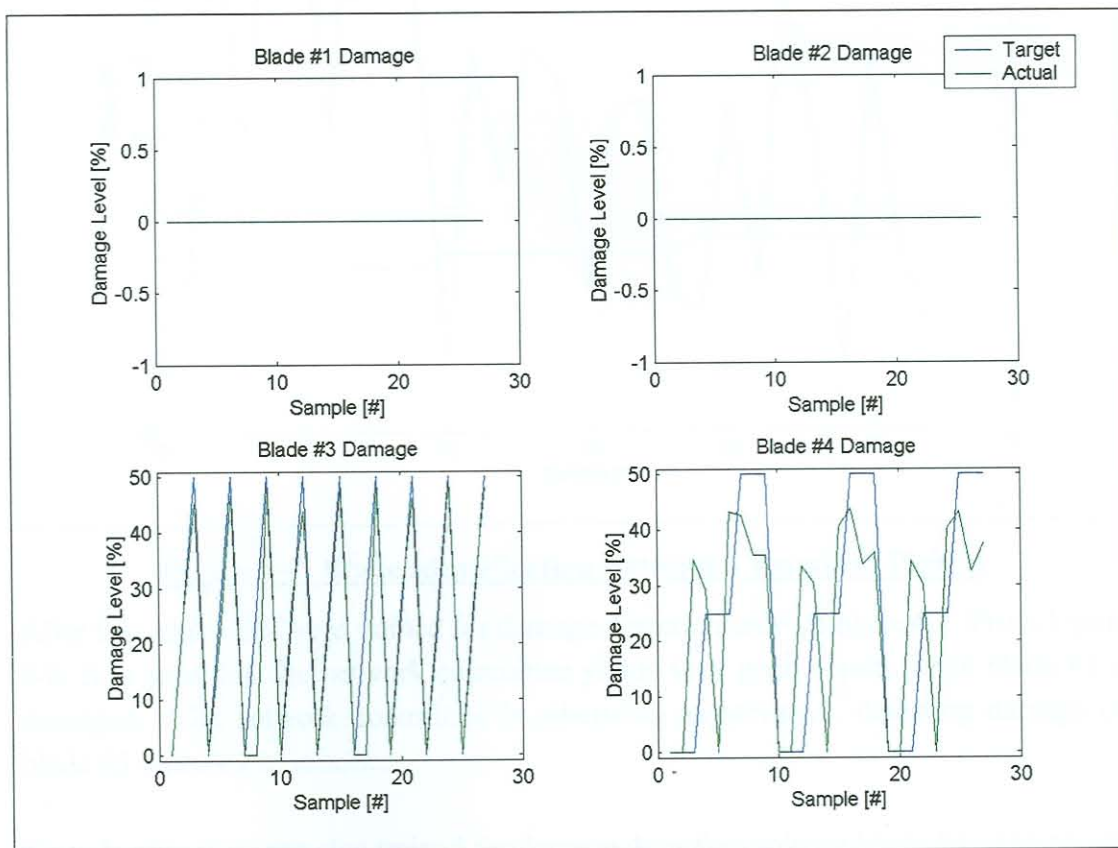
Figure 8-6: Multiple Blade Damage Detection Network Committee Results

An attempt was made to train networks for determining strain sensor locations. The results can be seen in Figure 8-7, showing that it was not possible to determine strain sensor location using the neural networks that were trained for this purpose. This problem of sensor location can possibly be rectified by training the previous set of networks using blade numbers relative to sensor position. In other words, instead of training the networks to quantify damage for a specific blade (in this case blade #3), the networks may rather be trained to quantify damage on the blade adjacent or opposite to the blade on which the specific strain sensor is located. As an example the same network trained to quantify the damage on blade #2 using the strain signal features of blade #1, may then be used to quantify the damage on blade #3 using the strain signal features of blade #2. Thus when this network detects damage, it is then known that the damage must be located on a blade adjacent to the blade on which the strain sensor is installed.
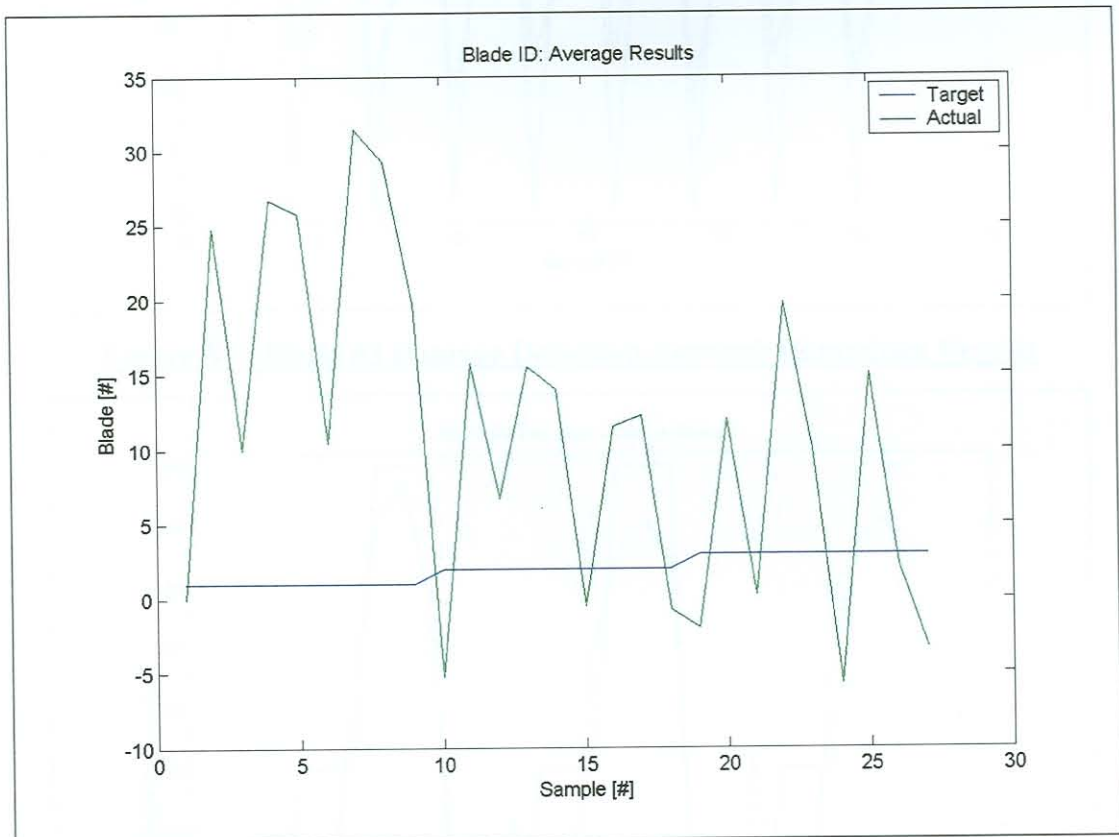
Figure 8-7: Blade Identification Network Committee Results

After this, networks were trained for damage detection only on blade #3. From Figure 8-8, it is seen that the network committee yields very good results when blade #3 is damaged. The network committee is otherwise conservative, detecting damage on blade #3 when there is none.

Neural networks were also trained for damage detection only on blade #4. The results of the network committee are shown in Figure 8-9. Relatively good results are

obtained for an undamaged blade #4 with blade #3 damage below 50%. Blade #3 damage has a large effect on the results at blade #4 damage levels of 25% and below. Overall, the results are not very accurate but are still indicative of blade #4 damage.
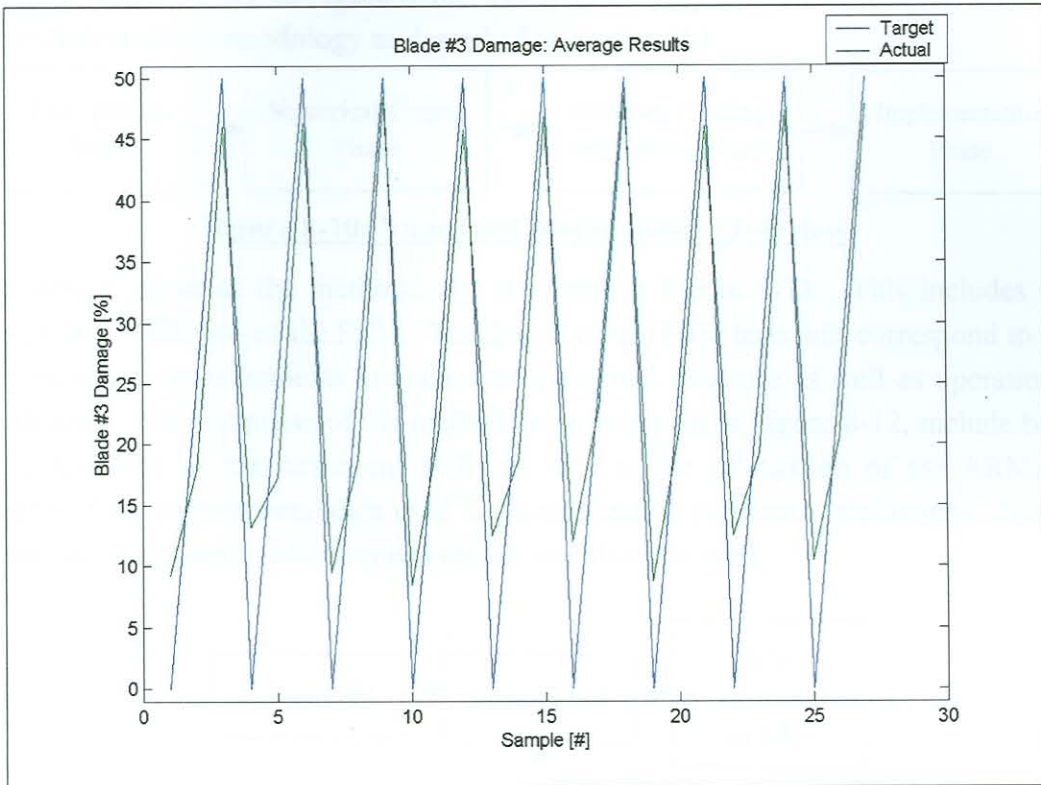
Figure 8-8: Blade #3 Damage Detection Network Committee Results
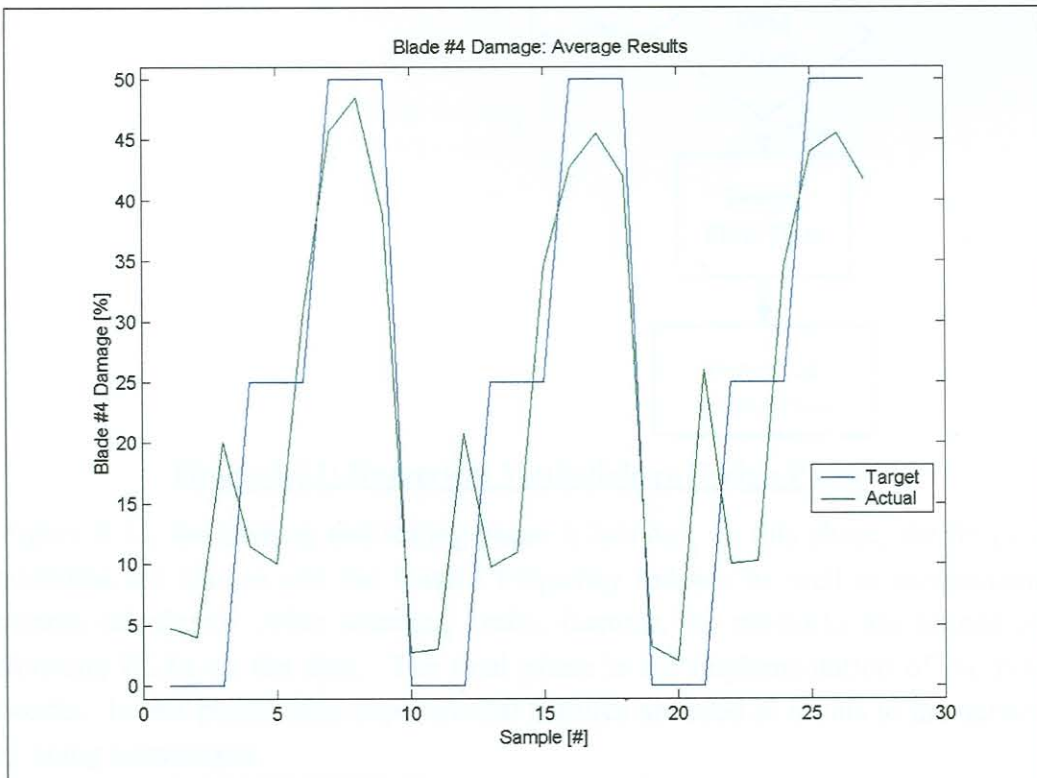
Figure 8-9: Blade #4 Damage Detection Network Committee Results

83

8.7. Numerical Methodology Summary

An overview of the numerically supervised neural network damage detection methodology is shown in Figure 8-10. The methodology phases are similar to that of the experimental methodology as described in Section 7.6.
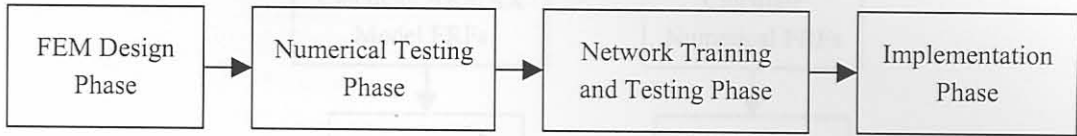
Figure 8-10: Numerical Methodology Overview

The design phase of the methodology is shown in Figure 8-11. This includes the design and validation of the FEM. The design of the FEM tests will correspond to the way in which measurements are taken on the actual structure as well as operational conditions. The test phase of the methodology as shown in Figure 8-12, include both the calculation of the numerical FRFs as well as the calculation of the ARMAX models of the experimental data used for normalization constants calculations. In this phase, the necessary modal frequencies are calculated as well.
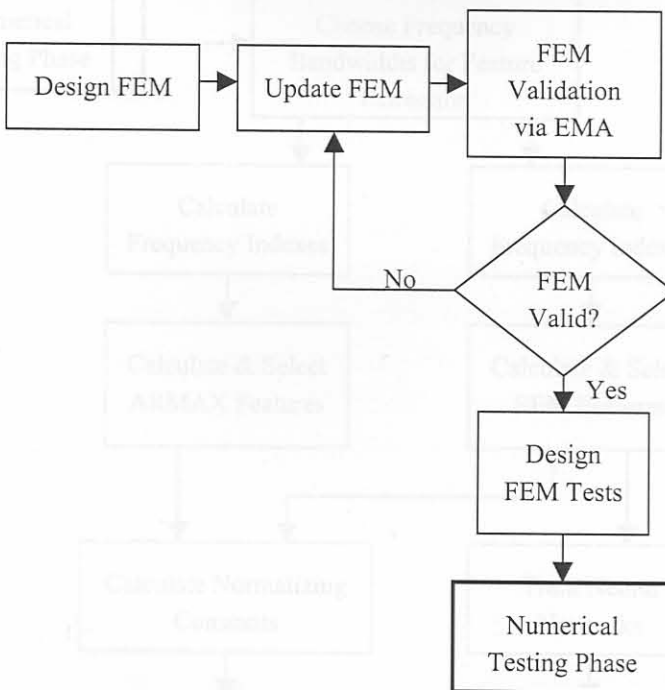
Figure 8-11: Numerical Methodology Design Phase

In Figure 8-13, the training and testing phase is laid out. In this phase, the frequency bandwidths are chosen and the feature frequency indexes as well as normalization constants calculated. After selecting usable features, the networks are trained after performing PCAs on the data. The final phase is the implementation of the neural networks. In this phase, only experimental features are used as inputs to the networks after being normalized.
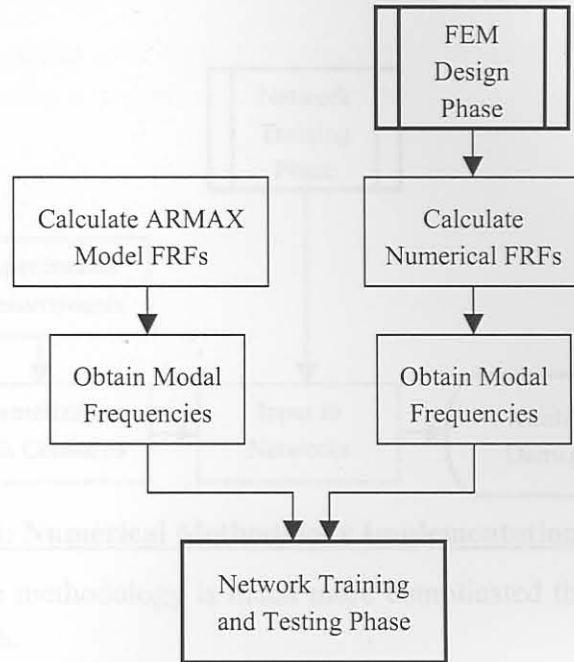
Figure 8-12: Numerical Methodology Test Phase
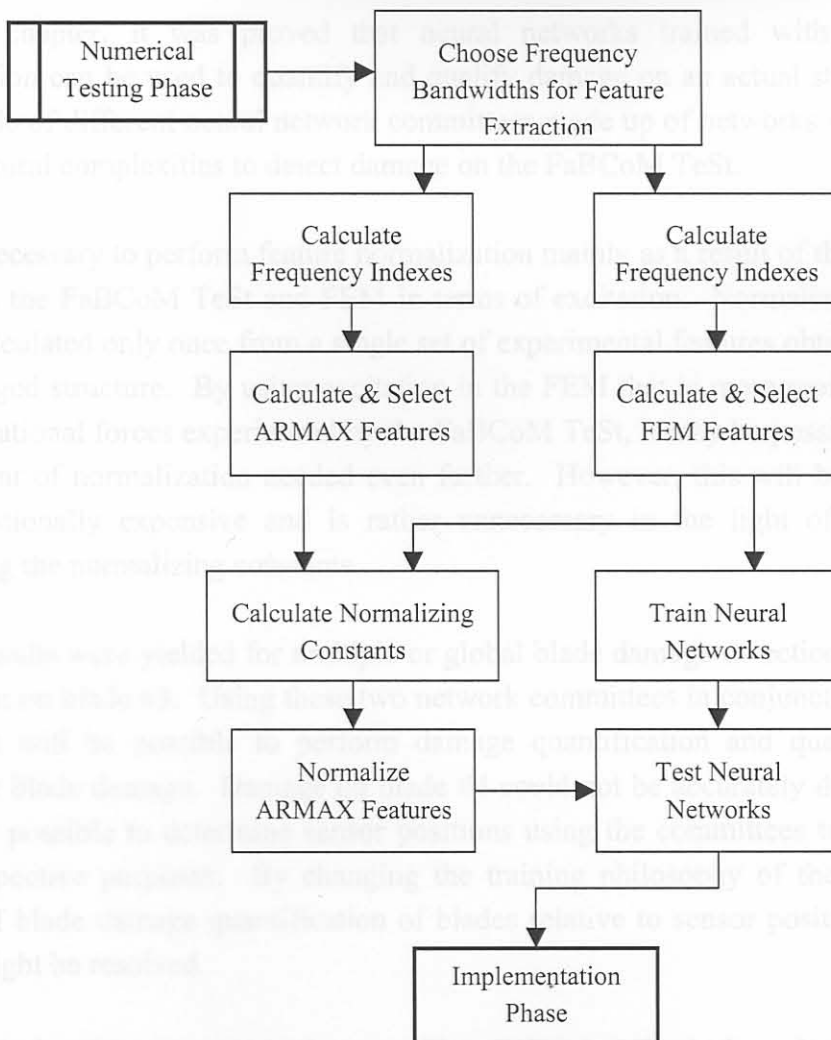
Figure 8-13: Numerical Methodology Training and Testing Phase
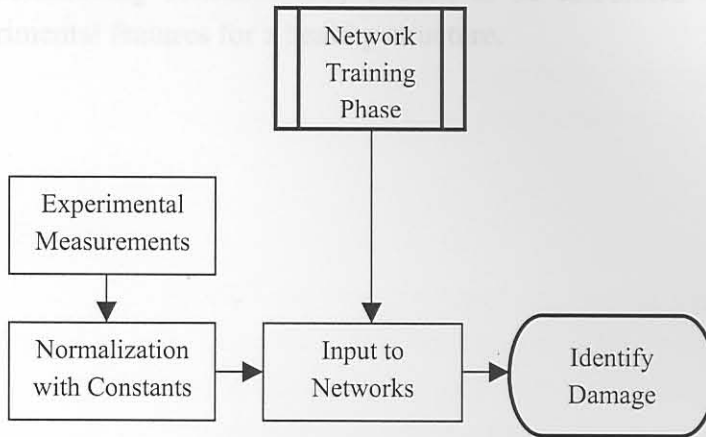
Figure 8-14: Numerical Methodology Implementation Phase

It is very clear that the methodology is much more complicated than that of the one presented in Section 7.6.

8.8. Conclusion

In this chapter, it was proved that neural networks trained with numerically supervision can be used to quantify and qualify damage on an actual structure. Use was made of different neural network committees made up of networks with different architectural complexities to detect damage on the FaBCoM TeSt.

It was necessary to perform feature normalization mainly as a result of the differences between the FaBCoM TeSt and FEM in terms of excitation. Normalizing constants were calculated only once from a single set of experimental features obtained from an undamaged structure. By using excitation in the FEM that is more representative of the operational forces experienced by the FaBCoM TeSt, it may be possible to reduce the extent of normalization needed even further. However, this will be much more computationally expensive and is rather unnecessary in the light of the ease of obtaining the normalizing constants.

Good results were yielded for multiple or global blade damage detection and damage detection on blade #3. Using these two network committees in conjunction with each other, it will be possible to perform damage quantification and qualification for multiple blade damage. Damage on blade #4 could not be accurately detected and it was not possible to determine sensor positions using the committees trained for the two respective purposes. By changing the training philosophy of the networks in terms of blade damage quantification of blades relative to sensor position, the latter issue might be resolved.

Although the aim was to train the networks solely on numerical results, use was still made of a set of experimental features for calculation of normalization constants.

However, these normalizing constants only needed to be calculated once using a single set of experimental features for a healthy structure.

Chapter 9   Conclusions

This chapter deals with the final conclusions with regards to key aspects of this dissertation including FEM utilization, telemetry identification and developed methodologies.

9.1. FEM Utilization

An extensive FEM of the FaBCoM TeSt was developed for several purposes. As a start, the FEM was used to determine the possibility of using GMSFs to quantify and qualify fan blade damage. Several damage cases and scenarios were used for this study and positive results were obtained. During this study, it was found that some GMSFs were sensitive to added blade mass. This directly influenced the way in which the EMA of the FaBCoM TeSt was conducted. The aim of the EMA was to identify the GMSFs of the FaBCoM TeSt to be used for monitoring during the tests. The EMA was also used to determine whether it would be possible to use torsional vibration measurements for blade damage detection, which proved to be the case.

The FEM was extensively updated before commencing work on the numerical neural network supervision approach. This was done in terms of material properties as well as structural damping assumptions. Making use of EMA results, the first shaft torsional mode frequency of the FEM was tuned to that of the FaBCoM TeSt. A MAC matrix of the FEM was calculated and showed the FEM to be a valid representation of the FaBCoM TeSt.

During testing of the FEM, use was made of a single excitation force with white noise characteristics. Due to the differences between this type of excitation and the more complex distributed excitation forces exerted on the FaBCoM TeSt during operation, it was necessary to normalize features for neural network training.

9.2. Telemetry Identification

Following a thorough investigation into the utilization of different techniques and technologies, it was decided to make use of a readily available slip ring assembly. Available wireless technologies were found to be limited in terms of masses, power supplies and measuring frequency ranges at the time of the investigation. However, several other researchers have already started to address these shortcomings. For industrial application, this technology will be preferred due the low maintenance required as opposed to slip rings.

9.3. Developed Methodologies

In this dissertation two methodologies for on-line fan blade damage detection was presented.

The first methodology entails the training of neural networks using experimental supervision. Using this methodology, neural networks were trained for different sensor locations using one piezoelectric strain sensor signal and one rotational acceleration signal per network. These networks were shown to be able to quantify blade damage on a four-bladed experimental structure for multiple blade damage using only two measurement signals. This methodology will be desirable to use where access to an experimental structure is readily available, or where damage measurements on an operational structure will not involve large cost implications.

The second methodology entails the training of neural networks using numerical supervision. Neural networks were trained for different sensor locations using features obtained from one strain sensor FRF and one rotational acceleration FRF per network. These FRFs were calculated from an updated FEM of the experimental structure. For each FRF, only frequency shifts of two natural frequencies as well as the area underneath the peak of another natural frequency were used as features. Experimental feature normalization constants were calculated only once from a single set of experimental features obtained from a healthy structure. Network committees were used and were found to be able to detect multiple blade damage. This methodology will be more desirable to use than the first methodology where it will be less costly to construct, update and test a FEM than to test an experimental or operational structure by means of damage simulation.

References

1. *Balmès E.,* Experimental and Analytical Structural Dynamics Toolbox Version 3 User's Guide, Scientific Software Group, 1997

2. *Barney P., Carne T.,* Modal Parameter Extraction Using Natural Excitation Response Data, Proceedings of the 17th IMAC, Florida, 1999

3. *Benham P.P., Crawford R.J., Armstrong C.G.,* Mechanics of Engineering Materials, 2nd Edition, Addison Wesley Longman Limited, ISBN 0-582-25164-8, 1998

4. *Boek M.J., Cybulski J.L., Szczepanik A.S.,* Embedding Neural Networks in On-line Monitoring Applications, ANZIIS 1993, pp. 172-176

5. *Brooks, T.,* Using Smart Accelerometers and Wireless Interfaces for Condition Monitoring, Machine, Plant and Systems Monitor, Coxmoor Publishing Company, May/ June 1999

6. *Bucher I.,* Rotating Machinery, Modal Testing and Signal Processing, Some New Results, Proceedings of the 9th DINAME, March 2001, pp. 573-587

7. *Bult K., Burstein A., Chang D., Dong M., Fielding M., Kruglick E., Ho J., Lin F., Lin T.H., Kaiser W.J., Marcy H., Mukai R., Nelson P., Newburg F.L., Pister K.S.J., Pottie G., Sanchez H., Stafsudd O.M., Tan K.B., Ward C.M., Xue S., Yao J.,* Wireless Integrated Microsensors, Proceedings of the Conference on Sensors and Systems (Sensors Expo). Anaheim, CA, USA, April 16-18, 1996, pp. 33-38

8. *Carne T.G., Nord A.R.,* Modal Testing of a Rotating Wind Turbine, Sandia National Laboratories Report SAND82-0631, 1983

9. *Castellini P., Revel G.M.,* Defect Detection and Characterization by Laser Vibrometry and Neural Networks, Proceedings of the 18th IMAC, San Antonio, Texas, Vol. 2, February 2000, pp. 1783-1789

10. *Corbelli A., Mastroddi F., Gennaretti M.,* Damage Detection for Helicopter Rotor Blades in Operative Conditions, Proceedings of ISMA 25, September 2000, pp. 179-186

11. *Demuth H., Beale M.,* Neural Network Toolbox (Version 4) For Use with Matlab, March 2001

12. *Doebling S.W., Farrar C.R., Prime M.B., Shevitz D.W.,* Damage Identification and Health Monitoring of Structural and Mechanical Systems from Changes in Their Vibration Characteristics: A Literature Review, Los Alamos National Laboratory, LA-13070-MS, May 1996

13. *Ewins D.J.,* Modal Analysis for Rotating Machinery, Silva, J.M.M., Maia, N.M.M., Nato Science Series, Series E: Applied Sciences – Vol. 363, Kluwer Academic Publishers, 1998

14. *Ewins D.J.,* Modal Testing: Theory and Practice, Taunton: Research Studies Press, 1988

15. *Farrar C.R., Doebling S.W., James G.H., Simmermacher T,* Structural Health Monitoring Activities at National Laboratories, Proceedings of the International Workshop on Structural Health Monitoring, Stanford, CA, September 1997, pp. 241-254

16. *Farrar C.R., Sohn H.,* Pattern Recognition for Structural Health Monitoring, LA-UR-00-5565: Workshop on Mitigation of Earthquake Disaster by Advanced Technologies, Las Vegas, NV, USA, November 30 – December 1, 2000

17. *Felber A.J., Ventura C.E.,* Frequency Domain Analysis of the Ambient Vibration Data of the Queensborough Bridge Main Span, Proceedings of the 14th IMAC, 1996, pp. 459-465

18. *Fredö C.R., Andrén P., Falk T.,* Mechanical Damping Simulation in MSC.Nastran, Nordic MSC User's Conference, Gothenburg, 1999

19. *Garnett-Bennett W.,* Draught Plant Systems Engineer, Majuba Power Station, South Africa, Private Communication, 2002

20. *Ghosh M., Rajamani A.,* Vibration Analysis of a Rotating Cooling Fan, Proceedings of the 3rd IMAC, Florida, 1985, pp. 459-464

21. *Ghoshal, A., Sundaresan, M.J., Shulz, M.J., Pai, P.F.,* Structural Health Monitoring Techniques for Wind Turbine Blades, Journal of Wind Engineering and Industrial Aerodynamics 85, 2000, pp. 309-324

22. *Haase W.C., Drumm M.J.,* Sensing Blade Vibration in Gas Turbine Engines, ExSell inc., January 2000

23. *Horowitz P., Hill W.,* The Art of Electronics, 2nd Edition, Cambridge University Press, ISBN 0-521-49846-5, 1995

24. *Hu N., Wang X., Fukunaga H., Yao Z.H., Zhang H.X., Wu Z.S.,* Damage Assessment of Structures using Modal Test Data, International Journal of Solids and Structures 38, 2001

25. *Johnson R.A., Wichern D.W.,* Applied Multivariate Statistical Analysis, 5th Edition, Pearson Education International, 2002

26. *Kim J., Ryu Y., Cho H., Stubbs N.,* Damage Identification in Beam Structures: Frequency-Based Method vs Mode-Shape-Based Method, Engineering Structures 25, 2003, pp. 57-67

27. *Lew J.,* Damage Detection Using Neural Networks and Transfer Function Correlation, Proceedings of the 18th IMAC, San Antonio, Texas, Vol. 2, February 2000, pp. 1783-1789

28. *Li W.J., Mei T.,* Sun W., A Micropolysilicon High-Angular-Rate Sensor with Off-Chip Wireless Transmission, Sensors and Actuators A 89, 2001, pp. 56-63

29. *Lobitz D.W.,* A Nastran-Based Computer Program for Structural Dynamic Analysis of Horizontal Axis Wind Turbines, Proceeding of the Horizontal Axis Wind Turbine Technology Workshop, Department of Energy and NASA-Lewis, Cleveland, May 1984

30. *Lomenzo R.A., Barker A.J., Wicks A.L.,* Laser Vibrometry System for Rotating Bladed Disks, Proceedings of the 17th IMAC, 1999, pp. 277-282

31. *Mannan M.A., McHargue P., Richardson M.H.,* Continuous Monitoring of Modal Parameters to Quantify Structural Damage, IMAC 12, February 1993

32. *Marscher W.D.,* Modal Testing of Rotating Machinery While it is Operating, Proceedings of the 17th IMAC, 1999, pp. 263-269

33. *Marwala T.,* Damage Identification Using Committee of Neural Networks, Journal of Engineering Mechanics, January 2000, pp. 43-50

34. *Maynard K.P., Trethewey M.,* Application of Torsional Vibration Measurement to Blade and Shaft Crack Detection in Operating Machinery, Maintenance and Reliability Conference, Gatlin burg, Tennessee, May 6-9, 2001

35. *Maynard K.P., Trethewey M.,* On the Feasibility of Blade Crack Detection through Torsional Vibration Measurements, Proceedings of the 53rd Meeting of the Society for Machinery Failure Prevention Technology, April 19-22, 1999, pp. 451-459

36. *Miettinen J., Salmenperä P., Järvinen V., Hirvonen M.,* Wireless Operation Monitoring System for Polymer Covered Cylinders in Rolling Contact, Proceedings of ETCE2002: ASME Engineering Technology Conference on Energy, February 4-6, 2002

37. *MSC.Software Corporation,* MSC.Patran FEA User's Guide Version 2000 (r2)

38. *Norton M.P.,* Fundamentals of Noise and Vibration Analysis for Engineers, New York: Cambridge University Press, 1989

39. *Olofsson P., Östling K.,* Bluetooth for Sensors, Master's Dissertation MEE-99-10, Blekinge Institute of Technology, 1999

40. *Quek S., Wang Q., Zhang L., Ang K.,* Sensitivity Analysis of Crack Detection in Beams by Wavelet Technique, International Journal of Mechanical Sciences 43, 2001, pp. 2899-2910

41. *Rao S.S.,* Mechanical Vibrations, 3rd Edition, Addison-Wesley Publishing Company, ISBN 0-201-59286-4, 1995

42. *Reschovsky J.,* Digital Rotor Telemetry, Sensors Magazine, Vol. 17, No. 9, September 2000

43. *Scheffer C.,* Development of a Wear Monitoring System for Turning Tools using Artificial Intelligence, Ph.D. Thesis (in print), University of Pretoria, 2002

44. *Shu H.T., Cutts D.G.,* Methods of Processing Strain Response Signals from Rotating Bladed Assemblies to Extract Modal Parameters, Proceedings of the 5th IMAC, London, 1987, pp. 700-706

45. *Smit W.G.,* Fan Blade Damage Detection Using On-line Vibration Monitoring, Master's Dissertation, University of Pretoria, 2001

46. *Staphorst L.,* Lecturer in Electronic Engineering, University of Pretoria, Private Communication, 2002

47. *Staszewski W.,* Monitoring ON-line Integrated Technologies for Operational Reliability – MONITOR, Air and Space Europe, Vol. 2, No. 4, 2000

48. *Stevens P.W., Smith E.C.,* Active Interrogation of Helicopter Rotor Faults using Trailing-Edge Flaps, Proceedings of the 19th IMAC, 2001, pp. 214-220

49. *Strydom J.P.D.,* Mechanical Engineer, Anglo Technical Division, South Africa, Private Communication, February 2003

50. *Südmersen U., Reimche W., Stegemann D., Liu Y.,* Condition Monitoring of Industrial Fans and Pumps by Advanced Vibrations Analysis, Turbokompressoren im ibdustrielen Einsatz, VDI/GET-Fachtagung, Hannover, 6/7 Oktober 1998

51. *Teughels A., Maeck J., De Roeck G.,* Damage Assessment by FE Model Updating using Damage Functions, Computers and Structures 80, 2002, pp. 1869-1879

52. *Waszczyszyn Z., Ziemianski L.,* Neural Networks in Mechanics of Structures and Materials – New Results and Prospects of Applications, Computers and Structures 79, 2001, pp. 2261-2276

53. *Wilkie W.K., Mirick P.H., Langston C.W.,* Rotating Shake Test and Modal Analysis of a Model Helicopter Rotor Blade, NASA Technical Memorandum 4760, ARL Technical Report 1389, June 1997

54. *Williams J.S., Wilson B.K., Hanner D.T.,* Measurement of the Rotational Vibrations of RWD Output Shafts and Characterisation of the Resulting Effect on Passenger Perceived Noise, Proceedings of the 1997 Noise and Vibration Conference, Traverse City, Michigan, 1997

55. *Wismer N.J.,* Application Note: Gearbox Analysis using Cepstrum Analysis and Comb Liftering, Brüel & Kjær, Denmark, Version BO0440-11

Appendix A FaBCoM TeSt Experimental Modal Analysis Results
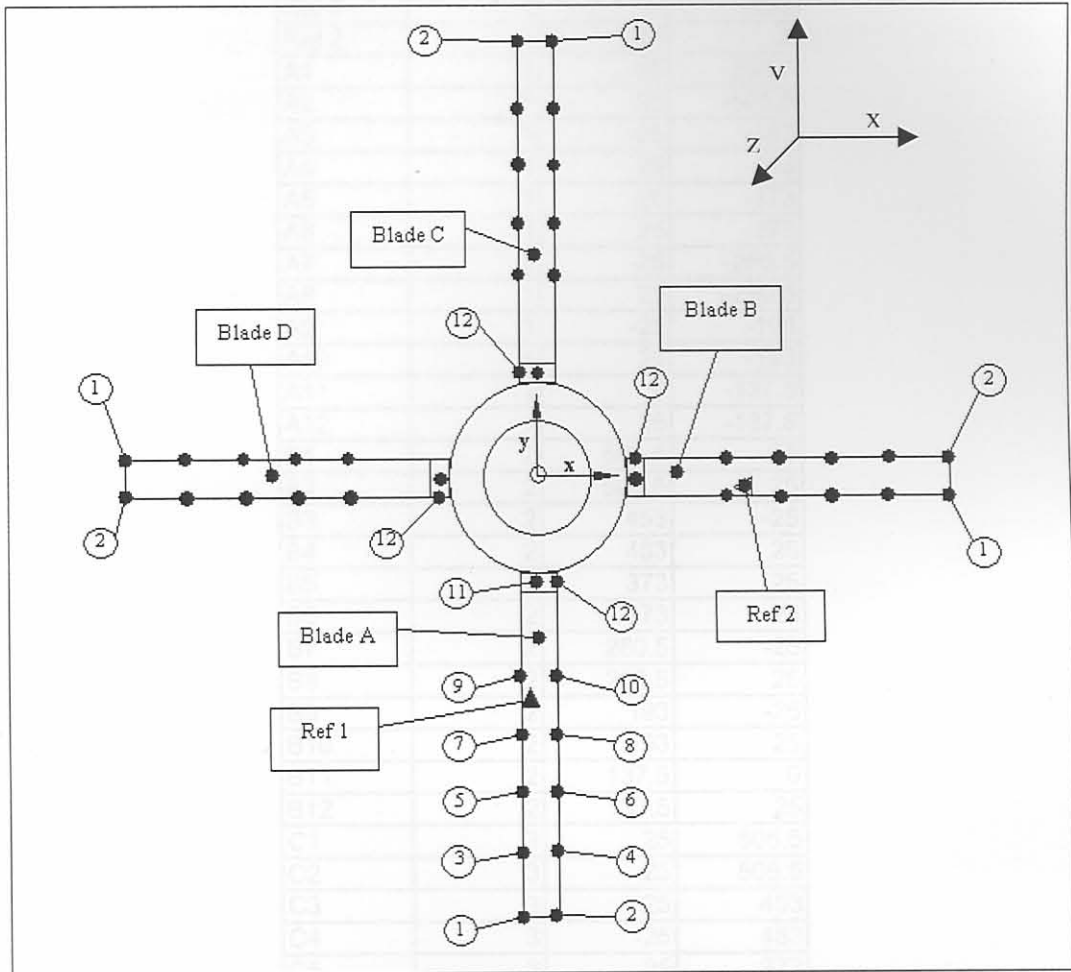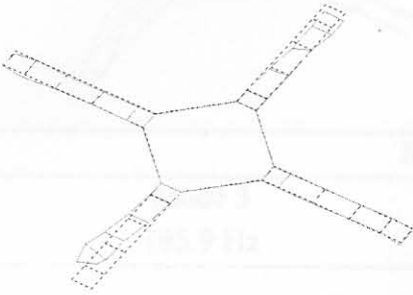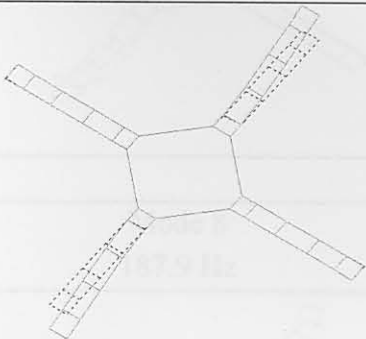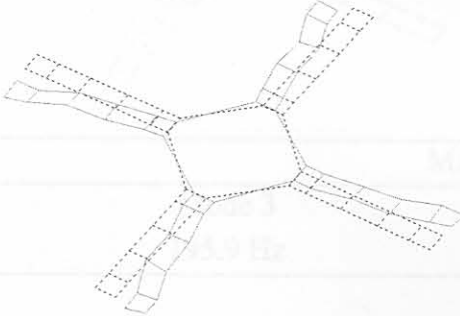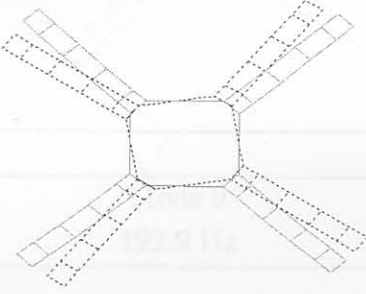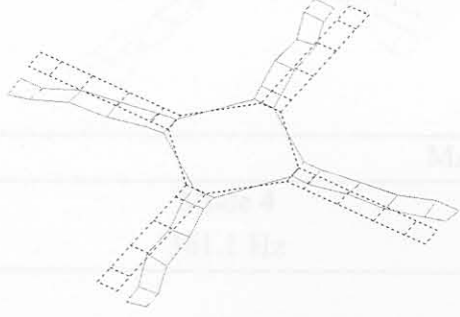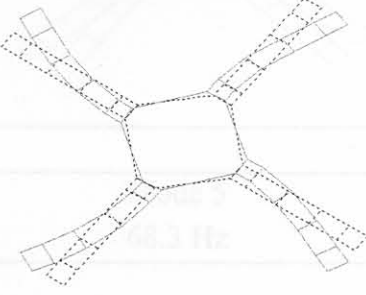
Figure A-1: Experimental Modal Analysis Measurement Point Locations
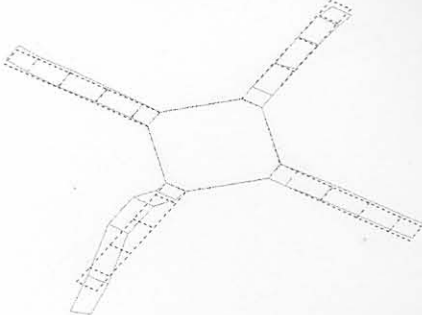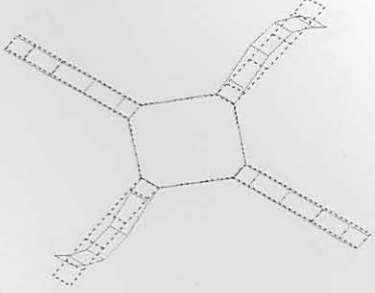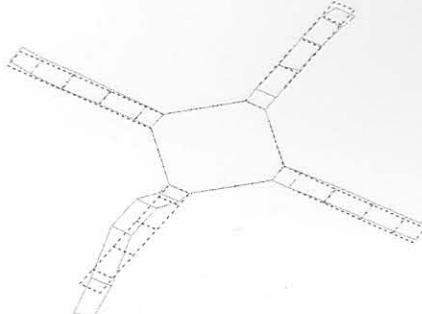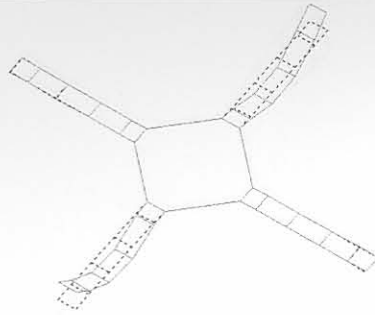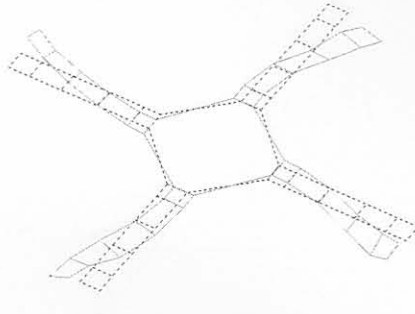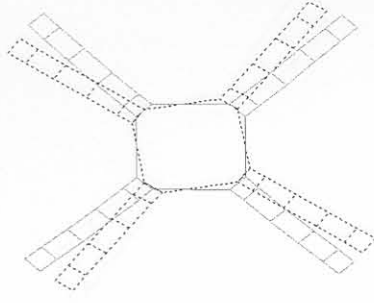
Table A-1: Experimental Modal Analyses Measurement Point Locations
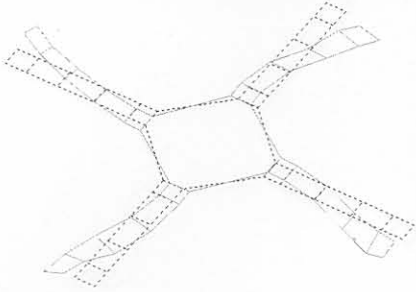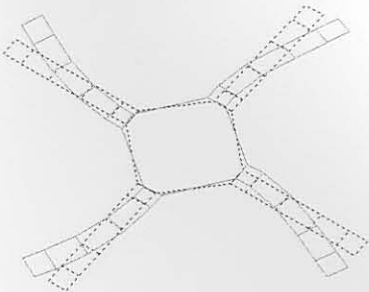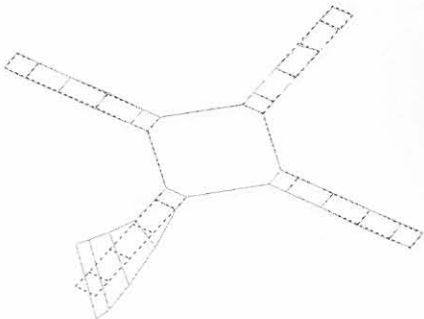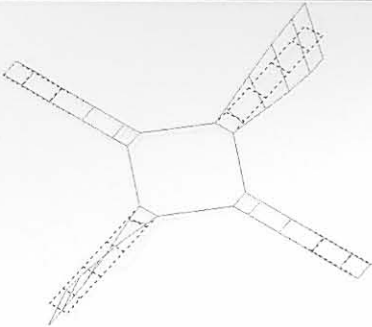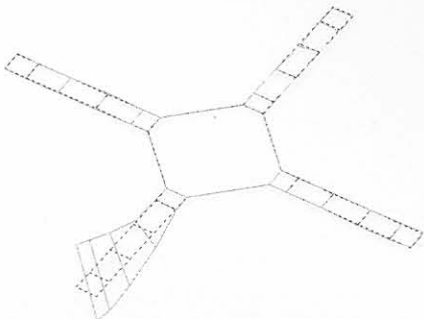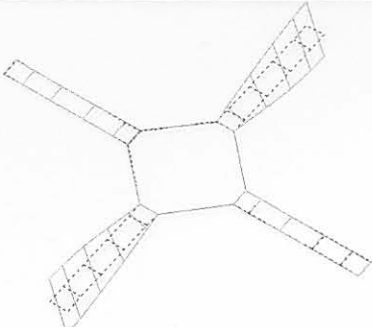
Point #	Blade #	X [mm]	Y [mm]
Ref 1	1	-8	-223
Ref 2	2	223	-8
A1	1	-25	-505.5
A2	1	25	-505.5
A3	1	-25	-453
A4	1	25	-453
A5	1	-25	-373
A6	1	25	-373
A7	1	-25	-280.5
A8	1	25	-280.5
A9	1	-25	-193
A10	1	25	-193
A11	1	0	-137.5
A12	1	25	-137.5
B1	2	505.5	-25
B2	2	505.5	25
B3	2	453	-25
B4	2	453	25
B5	2	373	-25
B6	2	373	25
B7	2	280.5	-25
B8	2	280.5	25
B9	2	193	-25
B10	2	193	25
B11	2	137.5	0
B12	2	137.5	25
C1	3	25	505.5
C2	3	-25	505.5
C3	3	25	453
C4	3	-25	453
C5	3	25	373
C6	3	-25	373
C7	3	25	280.5
C8	3	-25	280.5
C9	3	25	193
C10	3	-25	193
C11	3	0	137.5
C12	3	-25	137.5
D1	4	-505.5	25
D2	4	-505.5	-25
D3	4	-453	25
D4	4	-453	-25
D5	4	-373	25
D6	4	-373	-25
D7	4	-280.5	25
D8	4	-280.5	-25
D9	4	-193	25
D10	4	-193	-25
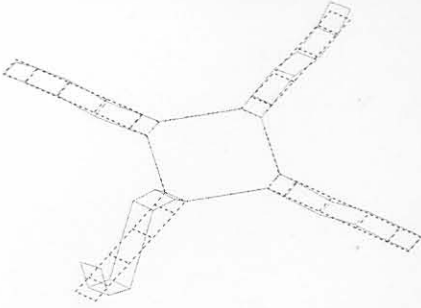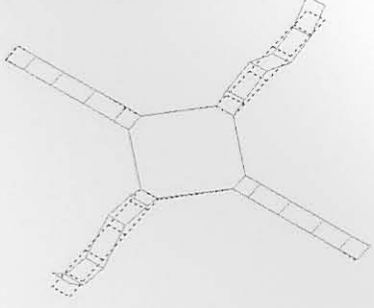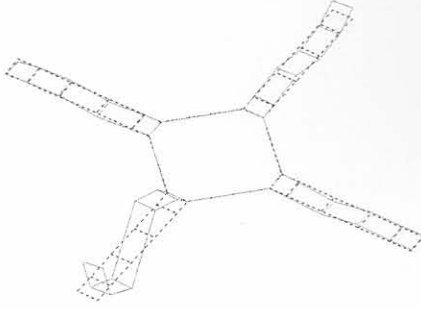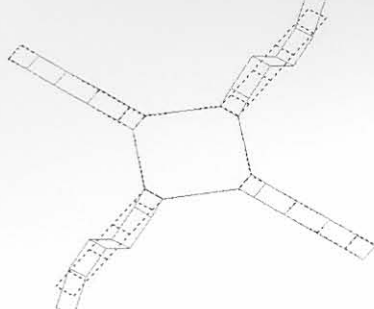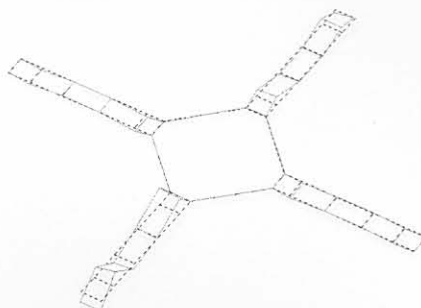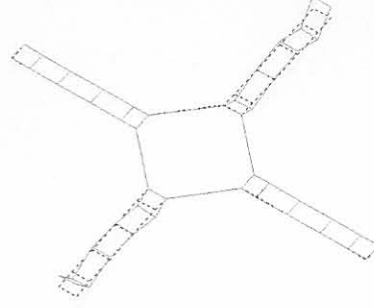
Table A-2 graphically compares experimental and numerical mode shapes with significant MAC. The MAC values between the mode shapes are given along with their mode shape numbers and frequencies.
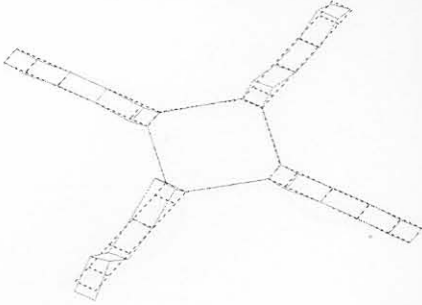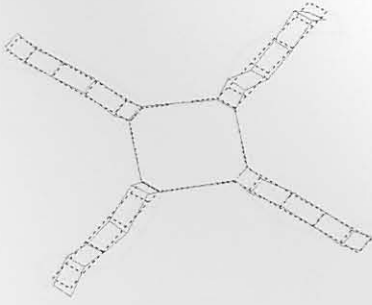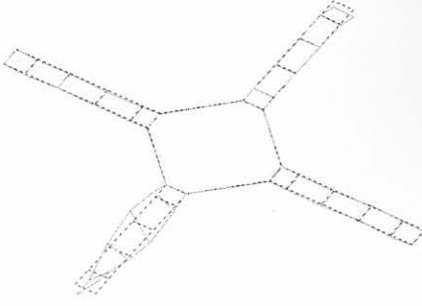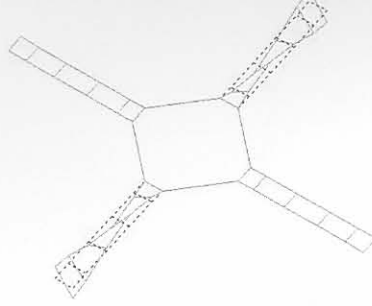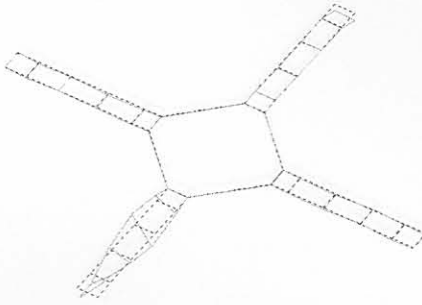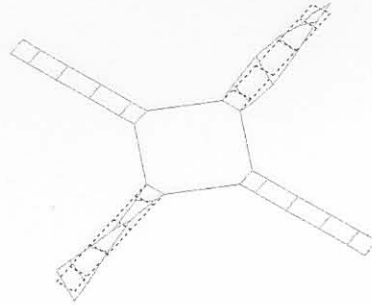
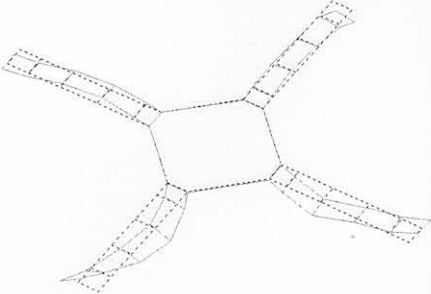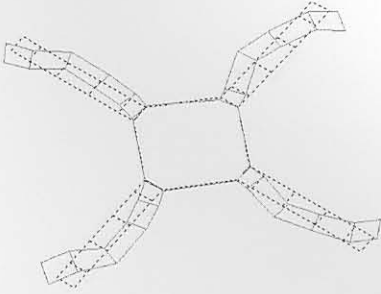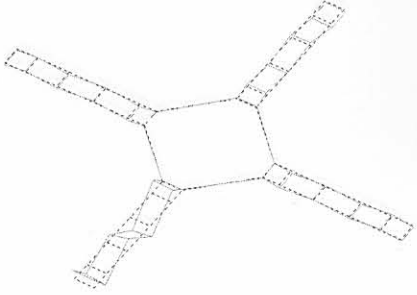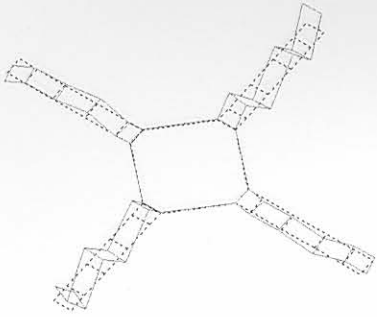**Table A-2: Graphical Experimental and Numerical Mode Shape Comparison**
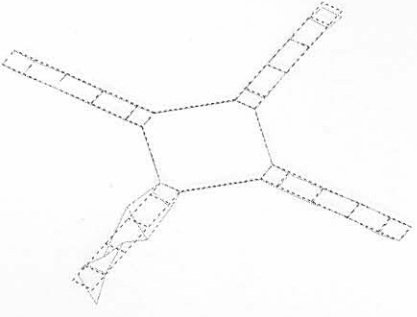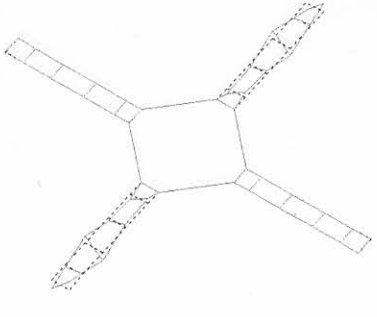
Experimental	Numerical
MAC = 0.78	
Mode 1 30.7 Hz	Mode 3 30.9 Hz
MAC = 0.93	
Mode 2 57.2 Hz	Mode 5 68.3 Hz
MAC = 0.58	
Mode 2 57.2 Hz	Mode 19 417 Hz

96
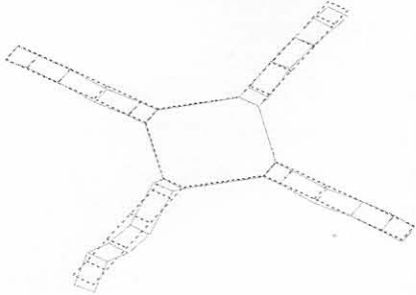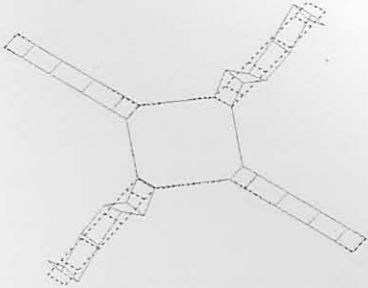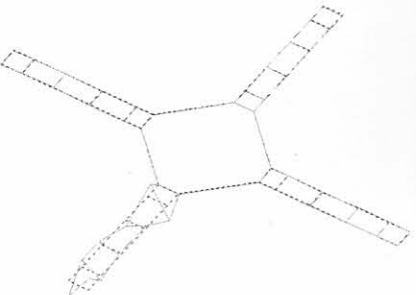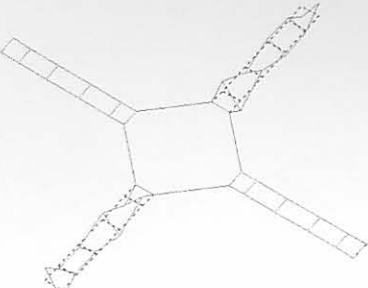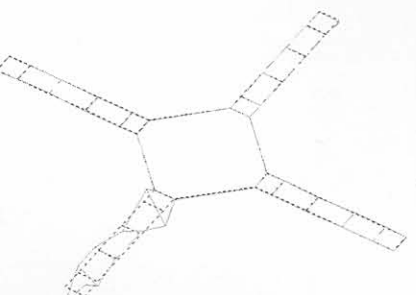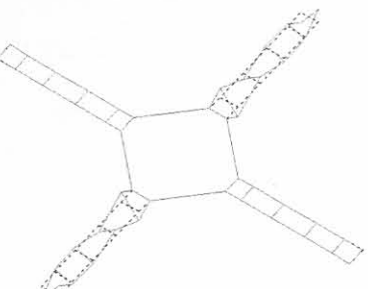
Experimental	Numerical
MAC = 0.37	
Mode 3	Mode 8
195.9 Hz	187.9 Hz
MAC = 0.62	
Mode 3	Mode 9
195.9 Hz	192.9 Hz
MAC = 0.52	
Mode 4	Mode 5
361.1 Hz	68.3 Hz
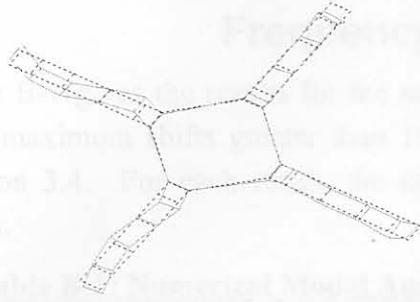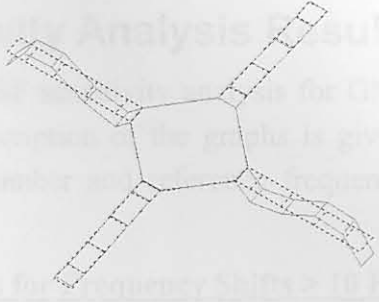
Experimental	Numerical
MAC = 0.80	
Mode 4 361.1 Hz	Mode 19 417 Hz
MAC = 0.47	
Mode 5 422 Hz	Mode 17 404.8 Hz
MAC = 0.44	
Mode 5 422 Hz	Mode 18 405 Hz
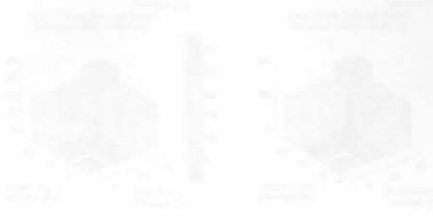
Experimental	Numerical
MAC = 0.70	
Mode 6 542 Hz	Mode 22 538 Hz
MAC = 0. 31	
Mode 6 542 Hz	Mode 23 541.3 Hz
MAC = 0.60	
Mode 7 1058.9 Hz	Mode 26 1049.3 Hz

Experimental	Numerical
MAC = 0.50	
Mode 7	Mode 51
1058.9 Hz	2630.6 Hz
MAC = 0.33	
Mode 8	Mode 30
1278.1 Hz	1220 Hz
MAC = 0.43	
Mode 8	Mode 31
1278.1 Hz	1220 Hz

Experimental	Numerical
MAC = 0.48	
Mode 9 1390.3 Hz	Mode 33 1623.2 Hz
MAC = 0.41	
Mode 10 1648.9 Hz	Mode 38 1715.8 Hz
MAC = 0.35	
Mode 12 2490.9 Hz	Mode 46 2061.4 Hz

Experimental	Numerical
MAC = 0.34	
Mode 13 2820.1 Hz	Mode 50 2585.2 Hz
MAC = 0.44	
Mode 14 3282.1 Hz	Mode 54 2943.6 Hz
MAC = 0.38	
Mode 14 3282.1 Hz	Mode 55 2943.9 Hz

Experimental	Numerical
MAC = 0.37	
Mode 16	Mode 59
3733.1 Hz	3487.8 Hz

Appendix B Numerical Global Mode Shape Frequency Sensitivity Analysis Results

Table B-1 gives the results for the numerical GMSF sensitivity analysis for GMSFs with maximum shifts greater than 10 Hz. A description of the graphs is given in Section 3.4. For each result, the mode shape number and reference frequency is given.

Table B-1: Numerical Modal Analysis Results for Frequency Shifts > 10 Hz

Mode 10 (241.2 Hz)	Mode 11 (242.24 Hz)
Mode 12 (288.13 Hz)	Mode 13 (310.49 Hz)
Mode 15 (399.08 Hz)	Mode 16 (399.53 Hz)

104

Mode 17 (405.97 Hz)

Mode 19 (420.95 Hz)

Mode 20 (523.1 Hz)

Mode 22 (542.42 Hz)

Mode 24 (1019.3 Hz)

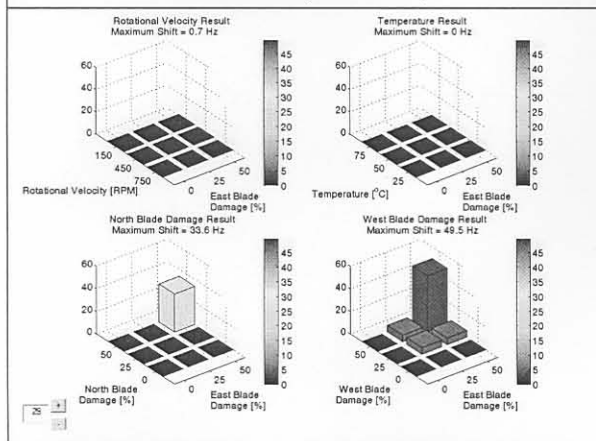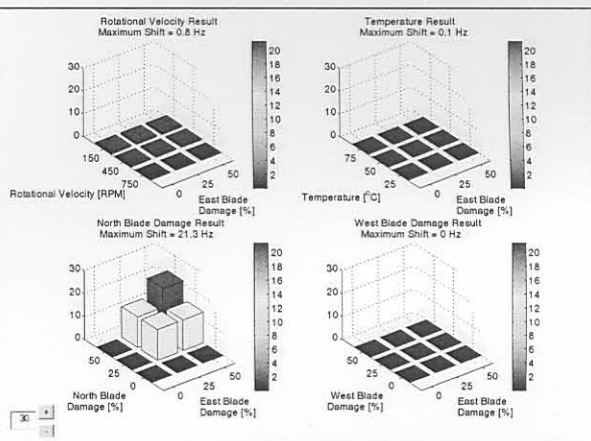Mode 25 (1021.1 Hz)
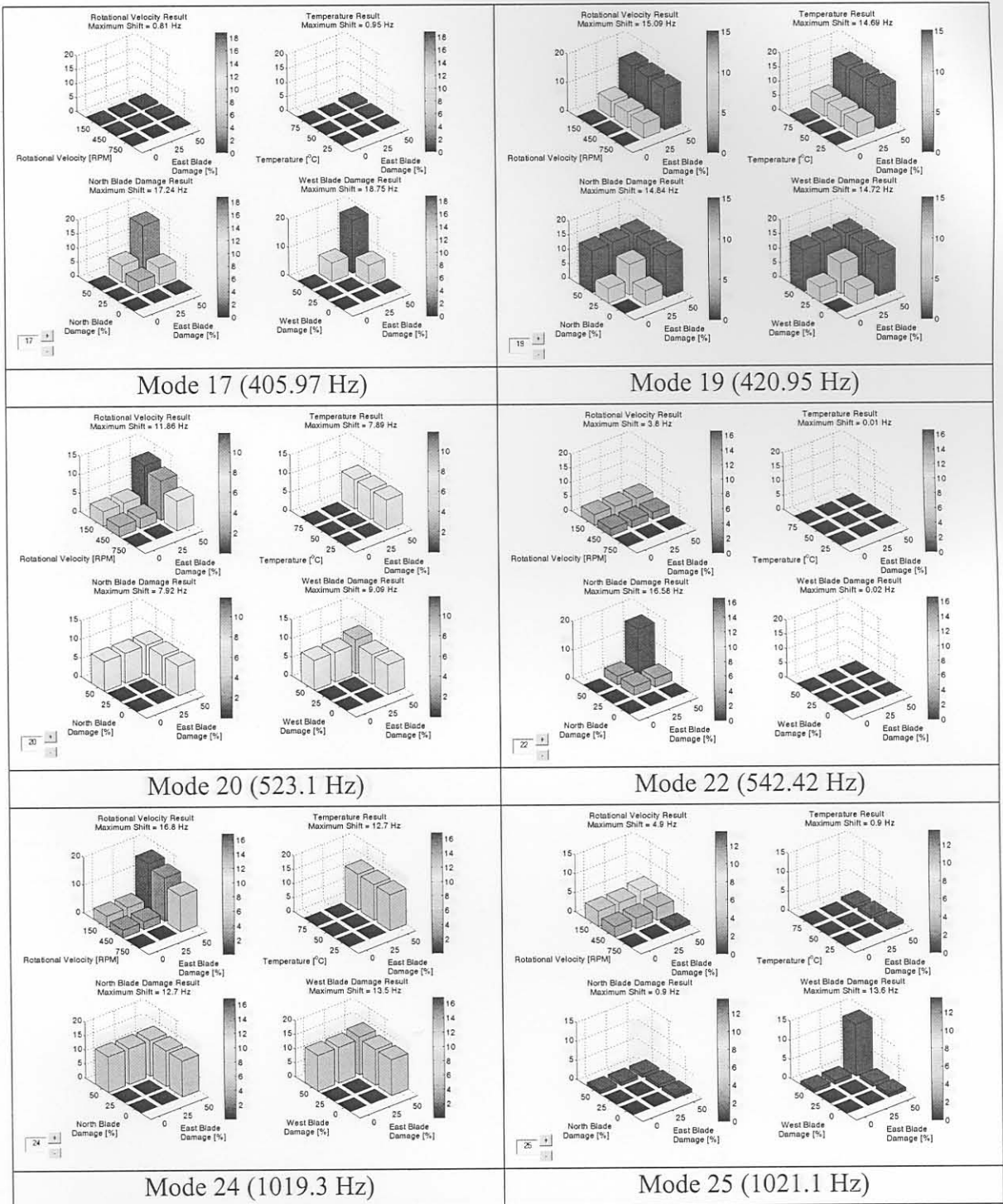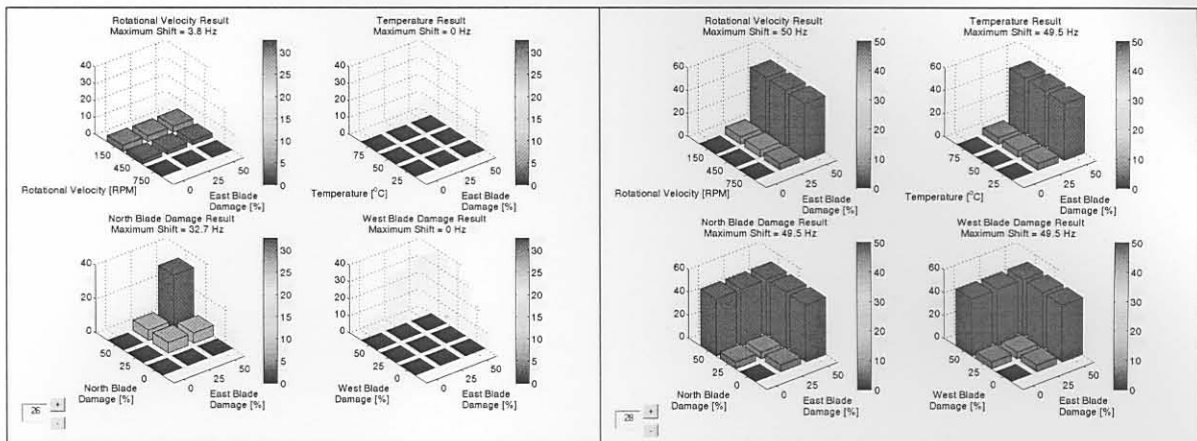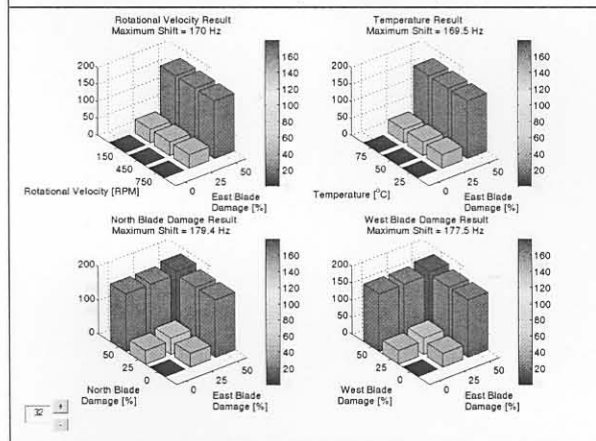
Mode 26 (1054 Hz)
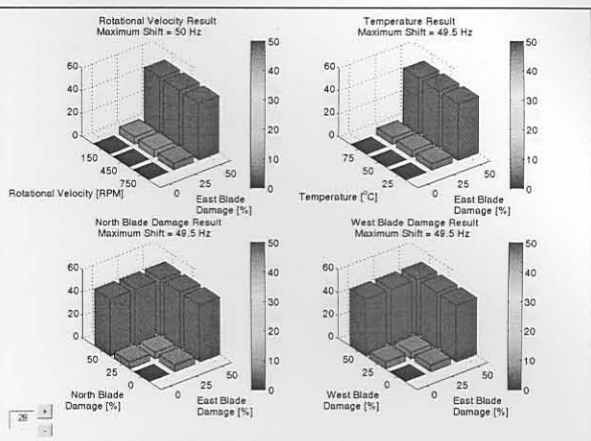
Mode 28 (1201.7 Hz)

Mode 29 (1201.7 Hz)

Mode 30 (1223 Hz)

Mode 32 (1633.1 Hz)

Mode 33 (1638.9 Hz)

Mode 34 (1648.3 Hz)

Mode 35 (1676.3 Hz)

Mode 36 (1677.5 Hz)

Mode 37 (1707.2 Hz)

Mode 38 (1725 Hz)

Mode 39 (1747.8 Hz)

Mode 40 (1792.3 Hz)

Mode 41 (1810 Hz)

Mode 42 (1970.7 Hz)

Mode 43 (2030.7 Hz)

Appendix C Neural Network Feature Selection

Feature #1   Feature #2   Feature #3   Feature #4   Feature #5

Feature #6   Feature #7   Feature #8   Feature #9   Feature #10

Feature #11   Feature #12   Feature #13   Feature #14   Feature #15

Feature #16   Feature #17   Feature #18   Feature #19   Feature #20
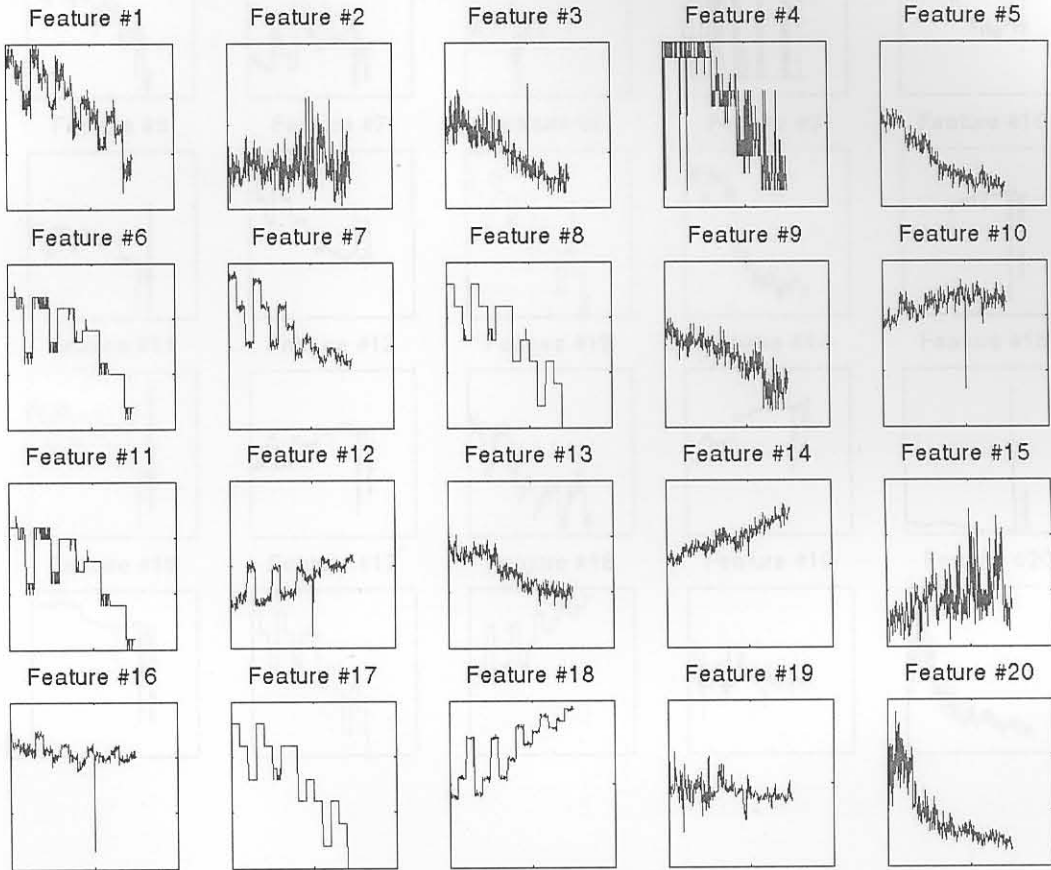
Figure C-1: Sensor Location #1 Feature Selection

Feature #1	Feature #2	Feature #3	Feature #4	Feature #5
Feature #6	Feature #7	Feature #8	Feature #9	Feature #10
Feature #11	Feature #12	Feature #13	Feature #14	Feature #15
Feature #16	Feature #17	Feature #18	Feature #19	Feature #20
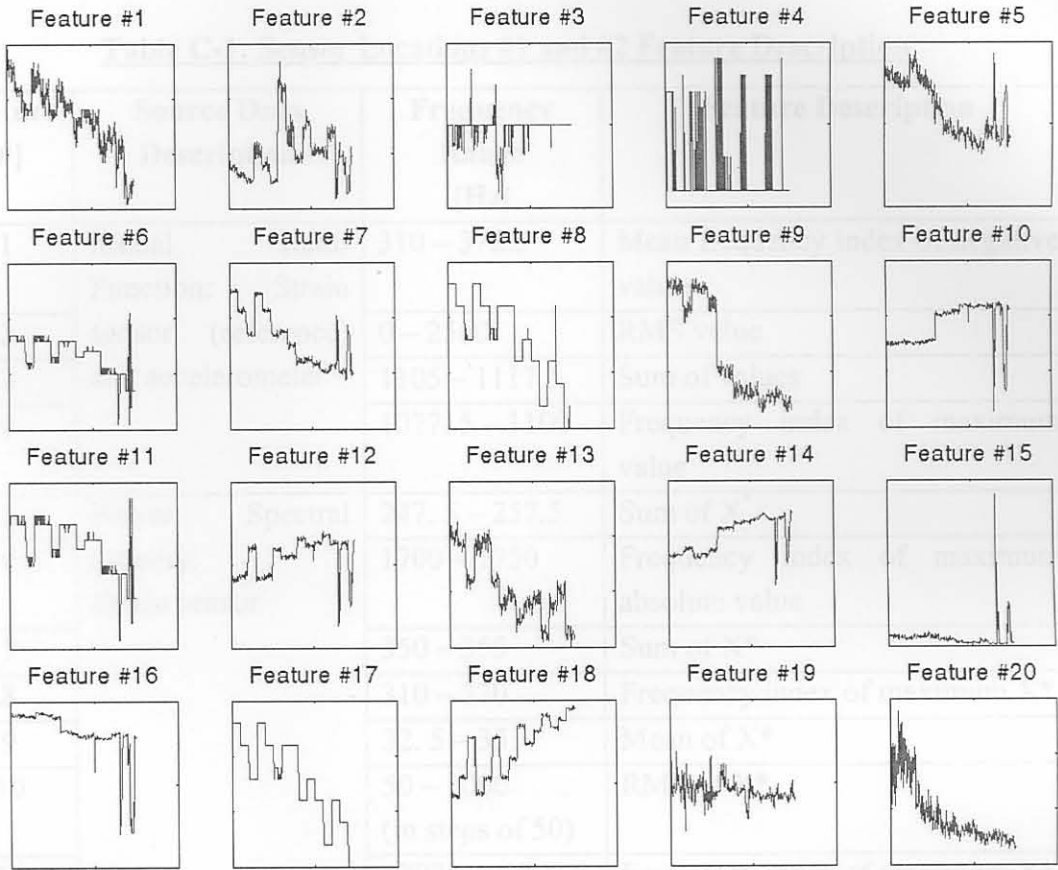
Figure C-2: Sensor Location #2 Features

Table C-1: Sensor Locations #1 and #2 Feature Description

Feature [#]	Source Data Description	Frequency Range [Hz]	Feature Description
1	Modal Ratio Function: Strain sensor (reference) and accelerometer	310 – 372.5	Mean frequency index of negative values
2		0 – 2560	RMS value
3		1105 – 1117.5	Sum of values
4		1077. 5 – 1100	Frequency index of maximum value
5	Power Spectral Density: Strain sensor	247. 5 – 257.5	Sum of X*
6		1700 – 1750	Frequency index of maximum absolute value
7		350 – 355	Sum of X*
8		310 – 370	Frequency index of maximum X*
9		32. 5 – 35	Mean of X*
10		50 – 1000 (in steps of 50)	RMS of X*
11		1702.5 – 1747.5	Frequency index of maximum X*
12		1737. 5 – 1745	Base 10 logarithm of absolute of sum of X*
13		560 – 562.5	Sum of X*
14		1072.5 – 1122.5	Base 10 logarithm of absolute of sum of X*
15		1772. 5 – 1810	RMS of absolute values
16		0 – 2560	Covariance of X*
17	Power Spectral Density: Accelerometer	310 – 370	Frequency index of maximum X*
18		347.5 – 357.5	Base 10 logarithm of absolute of sum of X*
19		0 – 2560	PSDRMS
20		1085 – 1122.5	Sum of absolute values

* X is the base 10 logarithm of the absolute values: $X = \log_{10}(|x|)$

Feature #1	Feature #2	Feature #3	Feature #4	Feature #5

Feature #6	Feature #7	Feature #8	Feature #9	Feature #10

Feature #11	Feature #12	Feature #13	Feature #14	Feature #15

Feature #16	Feature #17	Feature #18	Feature #19

Figure C-3: Sensor Location #3 Feature Selection

Table C-3: Sensor Location #3 Feature Description

Feature [#]	Source Data Description	Frequency Range [Hz]	Feature Description
1	Modal Ratio Function: Strain sensor (reference) and accelerometer	1092.5 – 1102.5	Sum of values
2		302.5 – 385	Frequency index of minimum value
3		2047.5 – 2560	RMS value
4		7.5 – 17.5	Sum of values
5		1470 – 1697.5	RMS value
6		0 – 2560	RMS value
7		302.5 – 332.5	Sum of values
8	Power Spectral Density: Strain sensor	1795 – 1805	Sum of X*
9		1740 – 1820	Frequency index of maximum absolute value
10		1700 – 1745	Frequency index of maximum absolute value
11		1300 – 1370	Frequency index of maximum X*
12		422.5 – 460	Maximum absolute value
13		2172.5 – 2322.5	Natural logarithm of maximum absolute value
14		2172.5 – 2322.5	Frequency index of maximum absolute value
15		0 – 2560	RMS of absolute value
16	Power Spectral Density: Accelerometer	310 – 370	Frequency index of maximum X*
17		347.5 – 357.5	Sum of X*
18		0 – 2560	RMS of X*
19		1085 – 1122.5	Sum of absolute values

* X is the base 10 logarithm of the absolute values: $X = \log_{10}(|x|)$

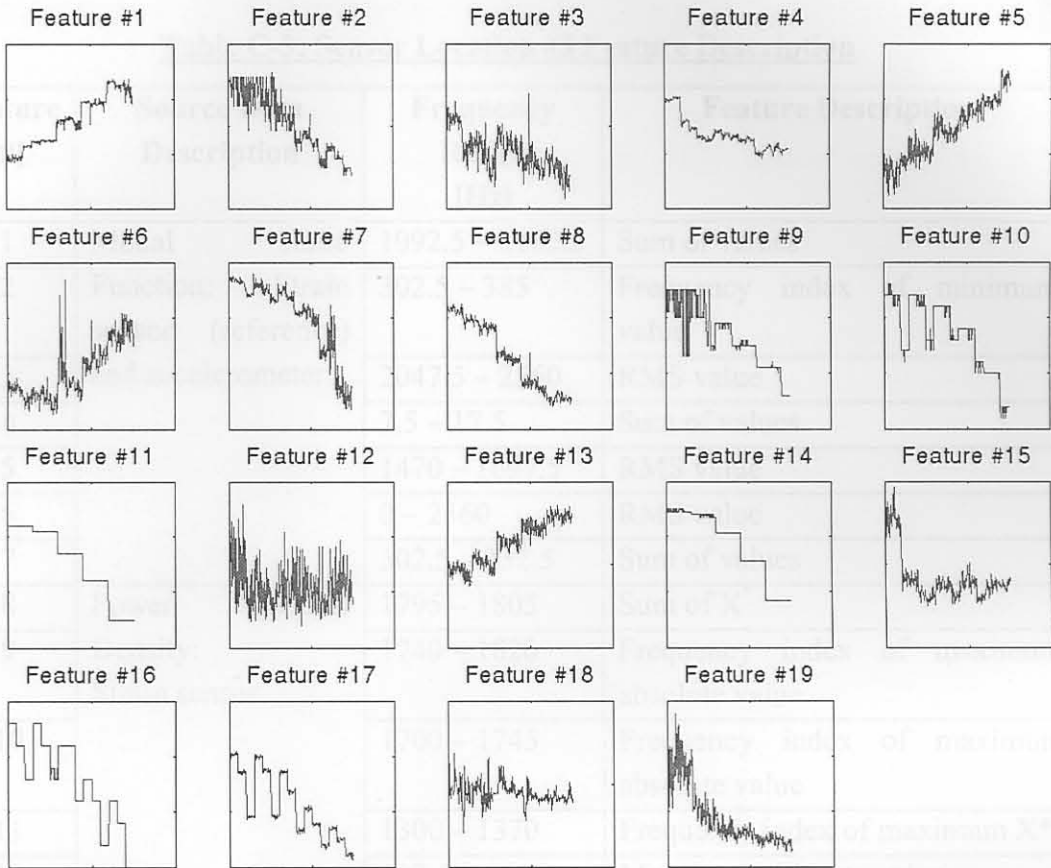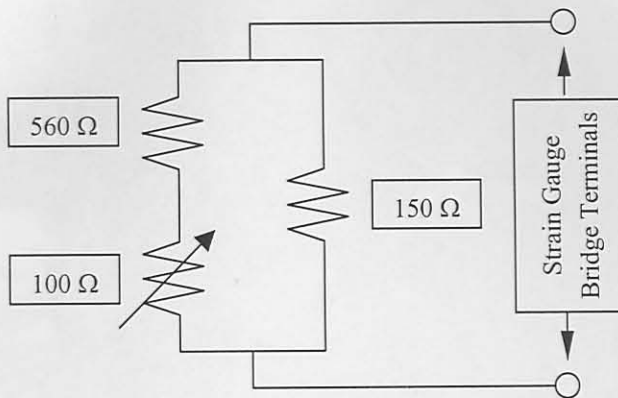**Figure D-2: Half Bridge Completion Circuit**

A single 9V PP3 battery performs bridge excitation.

In the second phase of the circuit, the strain gauges signals are amplified with an operational amplifier circuit with a gain of 1000. Power is supplied to the operational amplifier circuit by means of two 9V PP3 batteries. No filtering is performed in the circuit.

The system was tested and validated for static signals.

D.2. System Dynamic Testing

The developed system was tested using a 120 Ω strain gauge rosette installed on the reverse side of on of the FaBCoM TeSt blades as shown in figure D-3. A piezoelectric strain sensor was installed at the same position, but on the front side of the same blade. This was done in order to compare the measurement qualities obtained from the developed system and the piezoelectric system.

Figure D-3: Strain Gauge Rosette Orientation

Several measurements were taken for different conditions to verify the robustness of the developed system in terms of:

- Strain gauge rosette shielding
- Fan rotational velocity
- Motor speed controller noise contribution
- Strain signal amplification before and after the slip ring assembly

Measurements were taken in the form of PSDs from 10 averages with a Siglab signal analyser for a 2 kHz bandwidth with a frequency resolution of 0.625 Hz.

Figure D-4 shows the PSDs for the two systems for rosette shielding, 0 rpm with the motor speed controller switched on and strain signal amplification before sending it through the slip ring assembly. From Figure D-4 it is clear that the developed system has a much higher overall noise floor than the piezoelectric system.

Appendix D Developed Strain Gauge System Testing

The suitability of a developed strain gauge system for on-line blade vibration measurements was tested using conventional strain gauge rosettes. The results are compared with those from a piezoelectric strain gauge system consisting of a piezoelectric strain sensor and signal conditioner.

D.1. Half Bridge Strain Gauge Amplifier

As there were no strain gauge amplifiers with a minimum measurement bandwidth capability of 2000 Hz available for use, it was decided to develop such an amplifier as shown in Figure D-1.
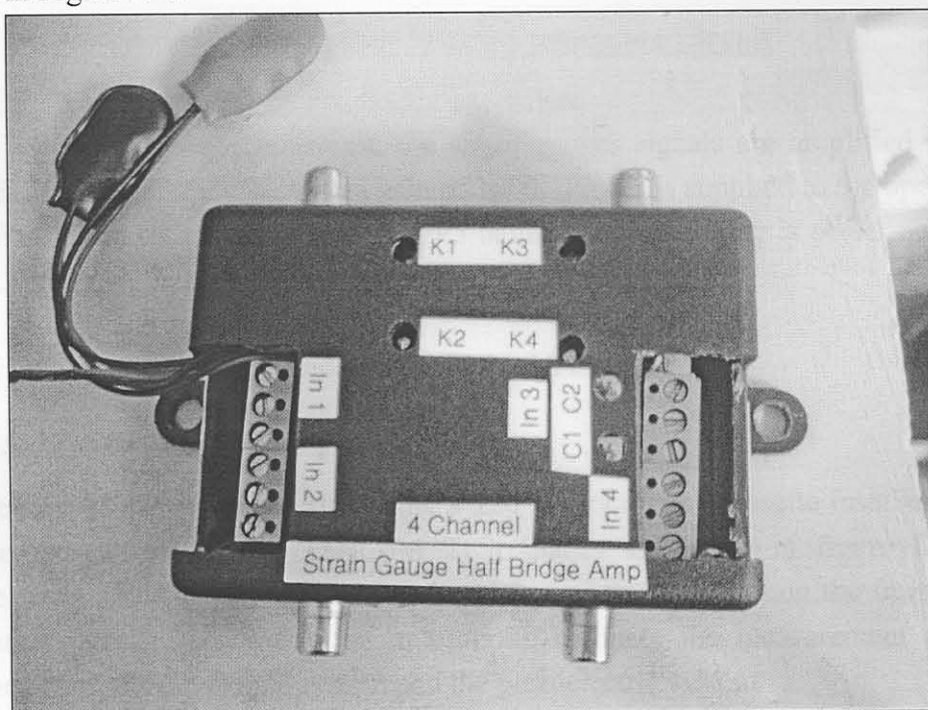

Figure D-1: Four Channel Half Bridge Strain Gauge Amplifier

In the first phase of the circuit, half bridge completion is performed for 120 Ω strain gauges using a dummy resistance circuit as designed by Scheffer [43] as shown in Figure D-2:
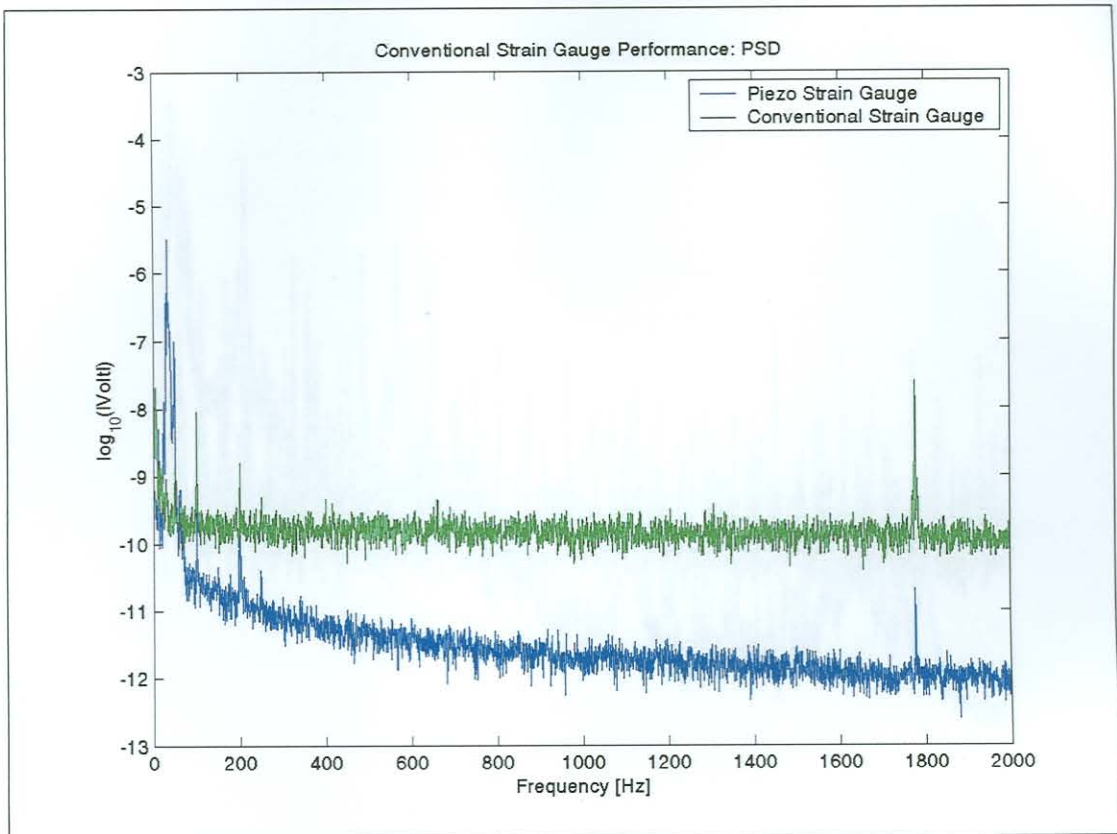
114

Figure D-4: Strain Gauge PSD Comparison: Ambient Electrical Noise

Figure D-5 shows the two PSDs for the same conditions as for figure D-4, except for a rotational velocity of 750 rpm. As seen in Figure D-5, the piezoelectric strain sensor system gave good results. However, it is also evident that the developed system has an extremely poor signal to noise ratio and that it does not correlate at all with the measurements from the piezoelectric strain sensor system.
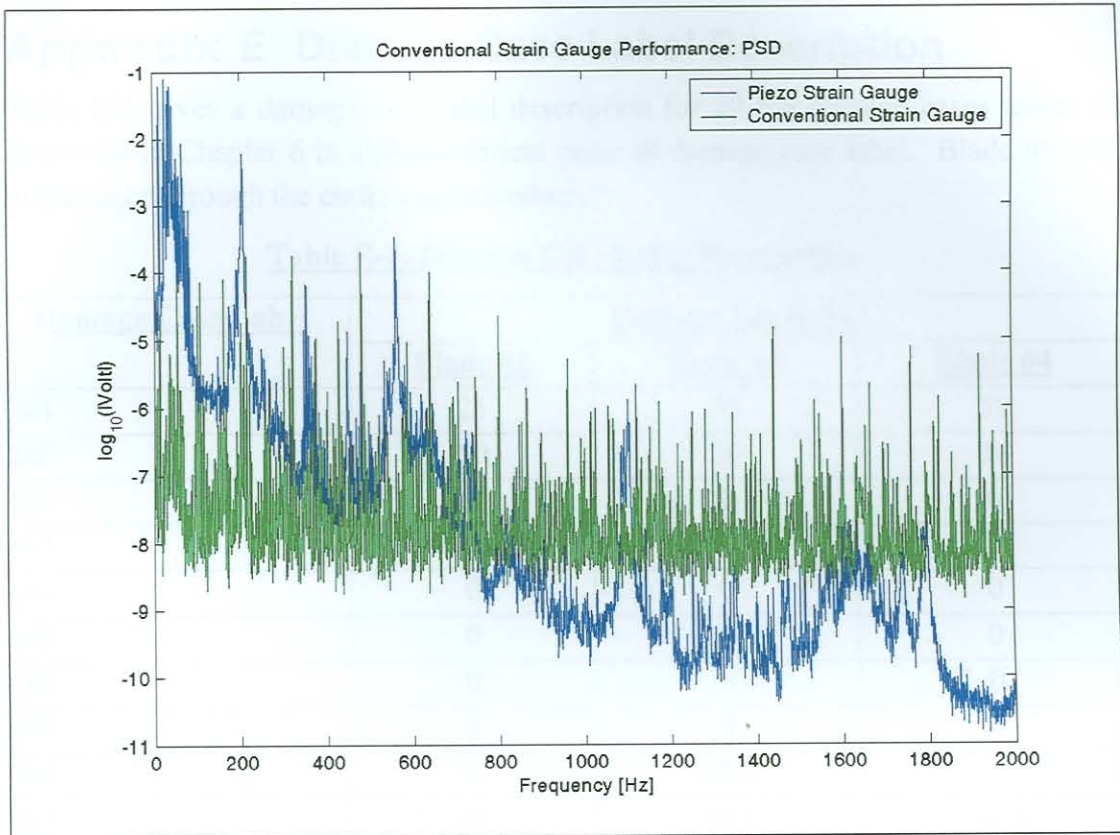
Figure D-5: Strain Gauge PSD Comparison: 750 rpm

D.3. Conclusion

From the tests performed, it is clear that the developed system is not suitable for the application of this dissertation. Possible causes for the poor performance of the system include the lack of signal filtering prior to amplification, the use of an operational amplifier in stead of a differential amplifier as advised by Horowitz and Hill [23] and the lack of system circuitry shielding.

Consequently, it was decided to make use of the piezoelectric strain sensor system.

Appendix E Damage Case Label Description

Table E-1 gives a damage case label description for all the damage cases tested as discussed in Chapter 6 in alphanumerical order of damage case label. Blade #1 was undamaged through the entire test procedure.

Table E-1: Damage Case Label Description

Damage Case Label	Damage Level [%]		
	Blade #2	Blade #3	Blade #4
2a4	25	50	50
2a6	50	50	50
4a2	0	0	0
4a3	0	0	0
4a4	0	0	0
4a5	0	0	0
4a6	0	0	0
4b1	0	0	0
4b2	0	12.5	0
4b3	0	12.5	12.5
4b4	0	12.5	25
4b5	0	12.5	37.5
4b6	0	12.5	50
4c1	0	0	0
4c2	0	25	0
4c3	0	25	12.5
4c4	0	25	25
4c5	0	25	37.5
4c6	0	25	50
4d1	0	0	0
4d2	0	37.5	0
4d3	0	37.5	12.5
4d4	0	37.5	25
4d5	0	37.5	37.5
4d6	0	37.5	50
4e1	0	0	0
4e2	0	50	0
4e3	0	50	12.5
4e4	0	50	25
4e5	0	50	37.5
4e6	0	50	50
4f2	0	50	0

Damage Case Label	Damage Level [%]		
	Blade #2	Blade #3	Blade #4
4f3	0	50	12.5
4f4	0	50	25
4f5	0	50	37.5
4f6	0	50	50